Diffusion Tensor Imaging with Free Water Elimination

By

Andrew Robert Hoy

A dissertation submitted in partial fulfillment of
the requirements for the degree of

Doctor of Philosophy
(Medical Physics)

At the
University of Wisconsin-Madison
2015

Date of final oral examination: 3/5/15

The dissertation is approved by the following members of the Final Oral Committee:

Andrew L. Alexander, Professor, Medical Physics
Oliver Wieben, Associate Professor, Medical Physics
M. Elizabeth Meyerand, Professor, Medical Physics
Barbara B. Bendlin, Assistant Professor, Medicine
Aaron Field, Professor, Radiology

For Christina, Ben, and Corinne

You are worth so much more than any idea, experiment or document that I will ever produce.

Abstract

Diffusion imaging has become a mainstay amongst neuroimaging methods. However, there is a paradox common to diffusion methods. While the measured signal is generated from displacements on the order of tens of micrometers, voxel sizes are typically 2-3 mm per side. Due to limitations in the achievable signal to noise ratio, relatively large voxels will likely remain standard in the field.

In turn, the resolution limits ensure that voxels at the interfaces between tissue and cerebrospinal fluid (CSF) will inevitably contain a mixture of both materials. This work sets out to deal with the situation of partial volumed voxels by modelling and removing the signal due to CSF.

This was accomplished by rigorously establishing an optimal protocol and robust fitting scheme, validating the method through *in vivo* tractography, applying the free water elimination technique to a group of individuals at risk for Alzheimer's disease and, finally, comparing results to those of the standard diffusion tensor imaging method.

Acknowledgements

I am thankful to have had Dr. Andy Alexander as my advisor. Andy always provided a level head, gave direction when needed, and gave me the latitude I needed to make this work my own.

I would like to thank Dr. Cheng Guan Koay without whom I would still be toiling over tensor estimation and optimization methods. Guan has demonstrated a pure love of science and learning as well as a detail oriented nature that I will forever benefit from having witnessed.

Dr. Steve Kecskemeti has imparted MRI knowledge to me on a daily basis during my entire time in Madison. I am forever indebted to Steve for the helpful discussions on how to conduct and analyze experiments.

The Waisman Center and Andy's lab group has put me in contact with many scientists who have been excellent technical resources and kind friends. These folks included Greg Kirk, Dr. Nagesh Adluru, David Thompson, Dr. Brittany Travers, Dr. Sam Hurley, Dr. Doug Dean III, and Dr. Pasha Hossienbor.

I am thankful to the United States Navy for this opportunity. I have CAPT (ret) Ray Fong, my mentor in the Navy, to thank for encouraging me to apply for this opportunity. Ray has taught me much about the Navy, work, and how to treat people. Thank you Mr. Fong. I hope I can repay your faith.

I would like to thank my parents, Bob and Anne Hoy. If I have accomplished anything it is because you prepared me to do so through your love, encouragement, and wisdom. I thank you for teaching me to be a godly man.

I am most grateful to my family. Christina, my wife of ten years, and our children Benjamin and Corinne have been my support and motivation. They have endured my many and varied hours at work with grace and love. Christina especially has been my source of constant support and the model for steadfast endurance and efficiency. I would be adrift without you.

Contents

List of Figures

List of Tables

Chapter 1

Introduction

1.1 Outline

Chapter 2 addresses much of the background, which will be revisited throughout the course of this dissertation, including an introduction to diffusion and diffusion tensor imaging. The theory behind diffusion imaging and the application of deterministic tractography is discussed. These tools will later be utilized as a means to test the validity of the free water elimination method.

This chapter also puts in place the motivation for such a technique. The practical limitations of resolution and the consequences for diffusion imaging are introduced. Lastly, Alzheimer's disease is discussed from a clinical and social perspective. This disease is demonstrated to be a poignant application for such a method as the one developed here.

Chapter 3 is the first rigorous discussion of the free water elimination diffusion imaging method. The theory as well as implementation details, are presented in this chapter. The search for an optimal acquisition is addressed through the use of Monte Carlo simulation techniques. These same techniques are used to characterize the estimation performance.

Additionally, an example case in human brain is presented in this chapter. An *in vivo* model comparison between diffusion tensor imaging and free water elimination is conducted using Bayesian Information Criteria. Likewise, the reduction in partial volume effects is shown in the human volunteer.

Chapter 4 provides a more thorough proof of CSF partial volume effect reduction through the use of deterministic tractography. Here three different white matter tracts (corpus callosum, fornix, and cingulum), of which, two (corpus callosum and fornix) are prone to CSF PVE and one (cingulum) is a ‘control’ are reconstructed for different DTI imaging techniques. The techniques compared are ‘classic’ DTI, fluid attenuation inversion recovery (FLAIR) DTI, and FWE DTI. It is known that FLAIR directly resolves CSF PVE and, thus, results in longer tract reconstructions. In this manner, reconstructed volume is used as the criteria for comparing methods.

While FLAIR is unquestionably effective at CSF PVE resolution, it has some undesirable characteristics which can be avoided through use of the

FWE model. This chapter demonstrates that the FWE method is capable of resolving PVE as well or better than FLAIR while providing greater SNR, anatomical coverage, and time efficiency.

Also, this chapter further investigates the meaning of the isotropic compartment in tissue that is distal from a CSF interface. Evidence is provided that lends credence to the hence unsupported hypothesis that the signal arises from the extracellular space.

Chapter 5 investigates the question of how white matter microstructure relates to CSF biomarkers for Alzheimer's disease. This is tested using tractography and voxel-based analysis of both FWE and DTI metrics as proxy for the microstructural environment.

The same set of tracts and general techniques employed in chapter 4 is used here for tractography. The reconstructed tracts are then used to define structure specific ROIs to evaluate the diffusion metrics in a series of generalized linear models (GLM). Once multiple comparisons were accounted for, there were no statistically significant results.

The voxel-based analysis was performed by using permutation testing across a white matter mask. For the original data, as well as each permutation, a GLM was fit and the resulting t-value recorded. This allowed for direct control of the family-wise error rate. For both DTI and FWE, several of the biomarkers were correlated with diffusion measures.

The FWE *f*-value was generally more sensitive to diffusion differences associated with CSF biomarker levels than DTI mean diffusivity. This was manifest in larger clusters of significant voxels across the brain. For both methods, the largest cluster was located in the left temporal lobe, a result that is in line with known pathology in Alzheimer's disease. The findings in this study suggest that the *f*-value may be sensitive to the loss of axons.

Chapter 6 summarizes the contributions of this work and outlines potential applications and developments in the future.

Chapter 2

Portions of this chapter have been published in *Brain Mapping: An Encyclopedic Reference* as the chapter entitled *Diffusion Imaging Methods (Elsevier) 2015.*

Background

2.1 Diffusion Tensor Imaging

Diffusion MRI is a noninvasive imaging technique that uses the microscopic movement of water molecules to probe tissue environments. While voxel sizes are typically 2-3 mm per side, the signal originates from water movements and microstructural features that are on the order of micrometers.

Diffusion is the random motion of particles due to stochastic thermal fluctuations (also known as Brownian motion). The Einstein equation [1] describes diffusion in one dimension

$$D = \frac{\langle \Delta r^2 \rangle}{2\Delta t}$$

where $\langle \Delta r^2 \rangle$ is the mean squared displacement (in mm^2), D is the coefficient of diffusion (in mm^2/s) and Δt is the diffusion time (in s). The coefficient of diffusion is a scalar quantity that depends on molecular size, viscosity of the medium, and temperature. In an unstructured medium, molecular displacements are characterized by a three-dimensional Gaussian probability distribution.

$$P(\Delta r, \Delta t) = \frac{1}{\sqrt{(4\pi D\Delta t)^3}} exp\left(\frac{-\Delta r^2}{4D\Delta t}\right)$$

Here we will define free water as water that is unhindered by boundaries. Free water has a coefficient of diffusion of 3 x 10^{-3} mm^2/s at 37° C. For a typical diffusion time of 50 ms, free water will be displaced approximately 17 μm on average.

In structured biological tissue, water does not freely diffuse. Rather, diffusion is modulated by barriers and obstacles in the environment. Some molecules are restricted inside cells or other closed spaces, while others are hindered by objects that alter their paths to be more tortuous. Additionally, barriers such as cell membranes slow the transport of water from one compartment to another. As a result, the measured diffusion is an apparent diffusion coefficient (ADC) that reflects the structure of the microscopic tissue environment.

The result of these tissue microstructural barriers is often an inequality in molecular hindrance with respect to direction. In fibrous tissue such as white matter, water diffusion is relatively uninhibited in the direction parallel to the fiber, while it is greatly restricted perpendicular to the fiber. Thus, in early diffusion MRI experiments, the parallel and perpendicular ADC was used to show anisotropy in diffusion in the brain [2,3].

Diffusion imaging is typically carried out with a pulsed gradient spin echo sequence utilizing a single shot echo planar imaging (EPI) readout. In this sequence, relatively large diffusion weighting gradients are placed on either side of the 180° refocusing pulse, Figure 2.3. The first gradient pulse induces a linear phase dispersion in space across the sample, and the second pulse re-phases the magnetization. In the absence of motion, the phases from both pulses completely cancel. However, the associated magnetization will accumulate phase that is proportional to the net displacement as water moves. In the case of coherent flow, this phase is proportional to the flow velocity and is the basis for phase contrast angiography. Conversely, diffusion causes incoherent random movements that will lead to a dispersion in the displacements and corresponding phases. This spread in the signal phase from diffusion causes destructive interference and attenuation of the image signal.

The measured signal is a function of the molecular diffusion, gradient amplitude, duration, and spacing. This attenuation due to diffusion was characterized by Stejskal and Tanner [4]:

$$A = exp\left[-\gamma^2 G^2 D \delta^2 \left(\Delta - \frac{\delta}{3}\right)\right] = exp[-bD]$$

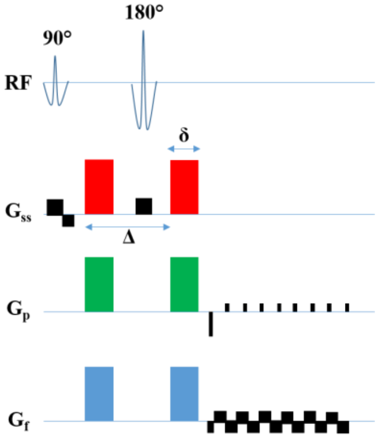

Figure 2.1: Diffusion Weighted Pulse Sequences. Diffusion weighting can be applied in any arbitrary direction through modulation of the slice select (red), phase encoding (green), and frequency encoding (blue) diffusion gradients.

where ɣ is the gyromagnetic ratio, G is the gradient amplitude, δ is the gradient duration, and Δ is the temporal separation between diffusion-encoding gradients. The collection of these terms is referred to as the b-value and determines the degree of diffusion weighting with $b = (\gamma G \delta)^2 \left(\Delta - \frac{\delta}{3}\right)$. It is important to note that the diffusion value above corresponds to diffusion only in the direction of the applied gradients. In order to calculate the full diffusion tensor, a minimum of six non-collinear gradient directions and a non-diffusion weighted acquisition are required. However, as more independent directions are acquired, the uncertainty in DTI metrics decreases [5].

There are two important signal dependencies that arise from the diffusion signal equation *in vivo*. Signal is dependent on the b-value used for the imaging sequence, Figure 2.2. As larger b-values are used, there is greater attenuation and more contrast between tissues with differing ADCs.

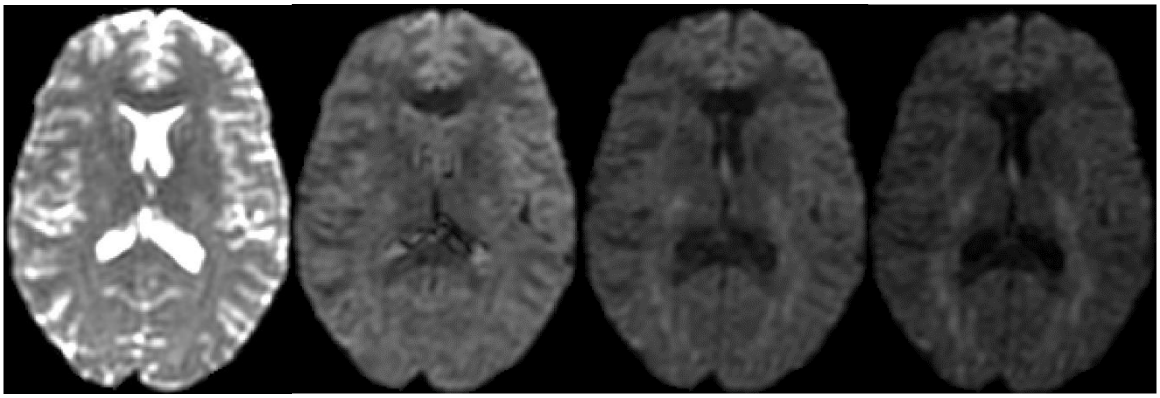

Figure 2.2: Signal dependence on b-value. All images have the same left-right gradient direction applied. From left to right, the b-values are 0, 500, 1000, and 1500 s/mm^2.

Second, there is a signal dependence on diffusion gradient direction in structured tissue, Figure 2.3. This directional dependence is a reflection of the diffusion anisotropy in tissue. As diffusion distances increase, signal attenuation also increases. Thus, for a single tissue that allows relatively unobstructed diffusion in one direction, but has greatly restricted diffusion in another direction, the measured signal is highly dependent on the diffusion direction.

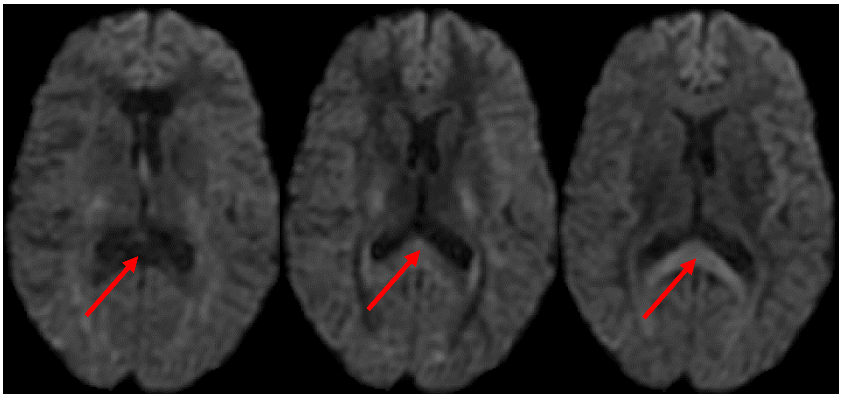

Figure 2.3: Signal dependence on gradient direction. All images have the same b-value of 1000 s/mm^2. From left to right, the gradient directions are left-right, anterior-posterior, and inferior-superior, respectively. The red arrow points out a major WM tract called the corpus callosum. In this slice, the corpus callosum is oriented primarily left-right and slightly anterior-posterior, thus, there is greater diffusion (hence more attenuation) in the left most image than there is in the right most image.

Basser et. al [6,7] proposed the diffusion tensor to better describe the anisotropic diffusion that is seen in the parenchyma of the brain. In this model the scalar coefficient of diffusion is replaced by a 3x3 matrix that is related to the covariance of the diffusion displacement in three dimensions. This matrix is symmetric (the off diagonals are equal) and positive definite, as a negative apparent diffusivity is physically meaningless. Due to symmetry, there are six unknown apparent diffusivities within the diffusion tensor.

$$D = \begin{bmatrix} D_{xx} & D_{xy} & D_{xz} \\ D_{xy} & D_{yy} & D_{yz} \\ D_{xz} & D_{yz} & D_{zz} \end{bmatrix}$$

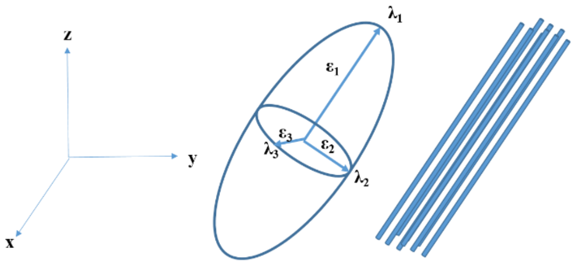

Figure 2.4: Visualization of the diffusion tensor. The tensor is visualized as an ellipsoid assumed to be aligned parallel to fibrous tissue such as white matter independent of the scanner reference frame.

The diffusion tensor may be diagonalized to yield eigenvalues (λ_1, λ_2, λ_3 with $\lambda_1>\lambda_2>\lambda_3$) and their corresponding eigenvectors (ε_1, ε_2, ε_3). This gives the magnitude of ADC (eigenvalues) along specific diffusion directions (eigenvectors). In this way, the tensor can be visualized as an ellipsoid with the principal axis direction given by the eigenvectors and length by the eigenvalues, Figure 2.4. The formalism also allows for the definition of several rotationally invariant scalar metrics, such as fractional anisotropy (FA), mean diffusivity (MD), radial diffusivity (D_R), and axial diffusivity (D_A).

$$MD = \frac{\lambda_1 + \lambda_2 + \lambda_3}{3}$$

$$FA = \sqrt{\frac{3}{2}}\sqrt{\frac{(\lambda_1 - MD)^2 + (\lambda_2 - MD)^2 + (\lambda_3 - MD)^2}{\lambda_1^2 + \lambda_2^2 + \lambda_3^2}}$$

$$D_R = \frac{\lambda_2 + \lambda_3}{2}$$

$$D_A = \lambda_1$$

These metrics are commonly ascribed certain physical interpretations. FA is thought to be indicative of general structural integrity in white matter. Meanwhile, axial diffusivity is thought to correlate with axonal integrity, and radial diffusivity is linked with degree of myelination. Figure 2.5 contains example axial slices of these metrics.

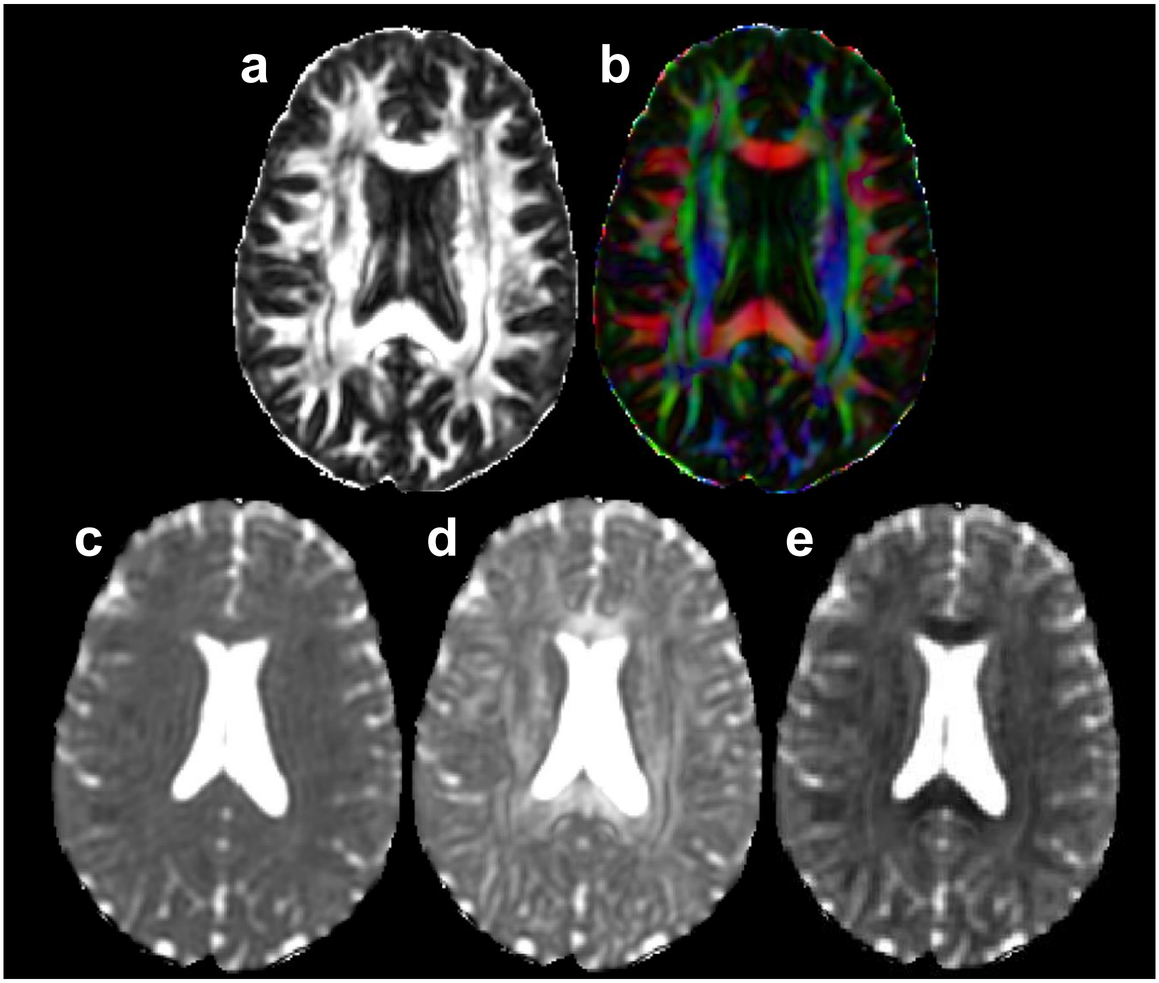

Figure 2.5: Diffusion metrics shown on an axial slice. These include different displays of FA (a and b) and ADC metrics (c, d, and e). FA can be displayed as in greyscale (a) with intensity determined by the magnitude of anisotropy or as a color coded image (b) with the primary eigenvalue determining the displayed color and the brightness determined by FA. ADCs can be displayed as the MD (c), D_a (d), or D_r (e). Here each image is displayed with the same scale.

Various tissue types in the brain display characteristic properties which can be identified in Figure 2.5. White matter (WM) is composed largely of coherent axon bundles. This composition leads to the high FA as seen in (a) and (b) and an axial diffusivity (d) which is generally much greater than the radial diffusivity (e). In comparison, cerebrospinal fluid

(CSF) and grey matter (GM) display nearly isotropic diffusivity characterized by low FA (a, b) and little difference between axial (d) and radial (e) diffusivities. However, these tissues vary greatly in their MD (c). Where CSF has an MD of $\approx 3 \times 10^{-3}$ mm^2/s, GM and WM have a very similar MD of $\approx 0.75 \times 10^{-3}$ mm^2/s.

2.2 Beyond the Diffusion Tensor

DTI is inextricably linked to the assumption of a Gaussian diffusion profile, however, this assumption does not hold in all cases. Restricted diffusion does not display Gaussian behavior as compartment size limits diffusion distance. Likewise, the presence of multiple fiber populations in a single voxel cannot be resolved with DTI. As diffusion weighting increases ($b > 2000$ s/mm^2), the departure from Gaussian behavior becomes more evident. Consequently, different formalisms have been introduced to more fully describe the observed diffusion signal.

With all diffusion models, it is important to consider the effects of the acquisition. As b-value increases so does signal attenuation, yielding a smaller SNR. The need to maintain some minimum SNR may necessitate that larger voxels be used. Additionally, while more diffusion directions increase the angular information, they also necessitate a greater scan time.

Choosing a diffusion acquisition and model requires an analysis of the costs and benefits associated with each.

2.2.1 High Angular Resolution Diffusion Imaging

High angular resolution diffusion imaging (HARDI) is a method which treats each voxel as an ensemble of some finite number of diffusion tensors [8]. In this way, the Gaussian assumption is maintained for any one of the compartments, but any single voxel may contain multiple compartments. This model makes it possible to visualize white matter pathways which cross one another while passing through a single voxel.

Generally, HARDI can refer to a class of diffusion methods which contain more information than the tensor model. This includes parametric and non-parametric models. These methods share a common acquisition with a single b-value (≈ 2000-4000 s/mm^2) and many (typically 60-100) diffusion directions distributed uniformly over a sphere. The exact b-value and number of directions are highly dependent on the chosen model.

2.2.2 Diffusion Kurtosis Imaging

Jensen and colleagues developed diffusion kurtosis imaging (DKI) [9,10], which utilizes the DTI framework while also quantifying the departure from Gaussian behavior. This deviation is measured as the kurtosis tensor. The link between DTI and DKI can be readily seen in the signal equation utilized for DKI:

$$ln\left(\frac{S_b}{S_0}\right) = -bD + \frac{1}{6}b^2DK$$

where K is the kurtosis tensor. Thus, DKI utilizes an additional second order term (in b) to measure deviation from Gaussian behavior. This definition allows for use of the typical DTI metrics with additional rotationally invariant apparent kurtosis metrics as well. A truly Gaussian diffusion profile results in a kurtosis value of zero.

Kurtosis provides information that is complimentary to DTI. Indeed, white and grey matter, which have a similar mean diffusivity, have a markedly different mean kurtosis. While kurtosis is sensitive to tissue microstructure [11], it cannot easily be tied out to a specific biophysical property. DTI estimates 6 parameters, while DKI fits 15 independent parameters. DKI also requires the use of two different b-values with a larger b-value of approximately 2000 s/mm^2.

2.2.3 Q-Space Imaging – DSI, HYDI

Q-space imaging seeks to fully quantify the diffusion displacement distribution (diffusion propagator) without any assumption about distribution or tissue structure. This is accomplished by exploiting the Fourier relation between the measured signal decay and the diffusion propagator:

$$\boldsymbol{E}_{\Delta}(\boldsymbol{q}) = \int \overline{\boldsymbol{P}}_{\boldsymbol{s}}(\boldsymbol{R}, \Delta)\boldsymbol{exp}(\boldsymbol{i2\pi q} \cdot \boldsymbol{R})\boldsymbol{dR}$$

where $\boldsymbol{E}_{\Delta}(\boldsymbol{q})$ is the measured signal as a function of q for a specific diffusion time (Δ), $\overline{\boldsymbol{P}}_{\boldsymbol{s}}(\boldsymbol{R}, \Delta)$ is the diffusion propagator, and R is the net displacement. Here q is related to the b-value, where $q = 1/2\pi\,\sqrt{(b/\Delta)}$. Q-space is the 3D space consisting of the coordinates (q_x,q_y,q_z) based on the q-value and the orientation (x,y,z) of the diffusion gradients used. Callaghan provides an excellent coverage of the foundation and formalism of q-space imaging [12].

Diffusion spectrum imaging (DSI) samples from q-space on a 3D Cartesian grid prior to using a fast Fourier transform to solve for the diffusion propagator [13]. This scheme commonly acquires as many as 500 images. To reduce the necessary number of images, Wu and Alexander proposed a hybrid diffusion imaging (HYDI) acquisition scheme that acquires samples on concentric spherical shells in q-space [14]. In addition to acquiring less samples, this scheme allows reconstructions with DSI, DTI and various other reconstruction schemes.

Once the diffusion propagator is known, several quantitative measures can be calculated including the mean displacement distance, the zero displacement probability (P_0), and the kurtosis. However, there are several experimental conditions which are necessary to accurately measure these quantities. First, known as the narrow pulse approximation, the diffusion gradient pulse width must be short so that the mean diffusion distance during the gradient on time is small relative to the compartment size, l. Second, Δ must be sufficiently long to ensure the water molecules can probe the compartment, i.e. $\Delta > l^2/2D$. Lastly, the signal must be measured until it is nearly completely decayed.

Hardware limitations ensure that the requisite assumptions, particularly the narrow pulse approximation, are not met. Consequently, the derived q-space metrics are approximate rather than exact values. The need to acquire many images leads to a longer acquisition time than most other diffusion methods. Additionally, the SNR penalty that is inherent with high b-value/q-value imaging limits the possible image resolution. Despite these limitations, q-space imaging provides comprehensive characterization of the diffusion displacement without the need for distribution assumptions or *a priori* knowledge of microstructural environment.

2.2.4 Model-Based Diffusion Imaging – CHARMED, NODDI, DBSI

In contrast to q-space techniques, there exists a category of model based techniques that makes *a priori* assumptions about the correspondence between microstructure and diffusion signal. In general, these models assign physical meanings, i.e. intra- and extra-axonal space, cellularity, CSF contamination, or neurite density, to certain diffusion patterns or characteristics. Three such techniques will be briefly introduced.

Assaf et al. [15] introduced the composite hindered and restricted model of diffusion (CHARMED). This model consists of one extra-axonal compartment and multiple intra-axonal compartments. The extra-axonal compartment is modelled as a diffusion tensor, which is characteristic of hindered diffusion. Each intra-axonal compartment is characterized by restricted diffusion within a cylinder.

Neurite orientation dispersion and density imaging (NODDI) assigns signal to intra-cellular, extra-cellular, and CSF compartments [16]. The intra-cellular compartment is modeled as a distribution of highly restricted sticks. A collection of cylindrically symmetric tensors models the extracellular compartment. Meanwhile, the CSF compartment is treated as having a fixed isotropic diffusivity.

Diffusion basis spectrum imaging (DBSI) fits a linear combination of a variable number of isotropic and anisotropic compartments at each voxel

[17]. The anisotropic tensors are considered representative of myelinated and unmyelinated axons, while the isotropic tensors are hypothesized to be indicative of cells, sub-cellular structures, and edematous water.

These models are extremely attractive as they provide meaningful biological explanations for the observed diffusion phenomena. Typically these techniques require a higher b-value, thus, less SNR and a longer acquisition time than DTI, but less time and greater SNR than q-space techniques. Improvements in gradient strength and the success of parallel imaging has made these techniques feasible in a clinical setting.

2.2.5 Diffusion Time for Probing Restricted Diffusion

It is believed that the axonal space is characterized by restricted diffusion. The restriction effects are strongly dependent on diffusion time and the size and shape of the restricting structure. Consider the simplified case of water residing in cylindrical axon with diameter d. When the diffusion time is very short, the majority of water molecules are uninhibited by the wall and, thus, they may diffuse freely. As the diffusion time increases, a greater percentage of the molecules will come in contact with the walls and the displacement distribution will deviate from Gaussian behavior. Higher b-values correspond to longer diffusion times, aligning well with the observation that non-Gaussian behavior is emphasized in high b-value imaging.

2.2.6 Method Selection

Diffusion MR imaging is a flourishing field which has grown in complexity and applications since its introduction nearly three decades ago. While DTI has become an accepted clinical procedure and other models have displayed utility in neuroscience research, there is no consensus 'best' model and acquisition. Understanding the relative strengths and weaknesses associated with each techniques is critical when evaluating studies and deciding on protocols.

2.3 Deterministic Tractography with DTI

Relative organization of WM fibers can be visualized by modulating FA values by a color determined by the orientation of the major eigenvector [18], Figure 2.5b. This system decomposes the major eigenvector into anatomical coordinates of left-right, anterior-posterior, and inferior-superior, corresponding to red, green, and blue, respectively. As was previously stated, the primary eigenvector is assumed to be tangential to the underlying WM fibers.

The two-dimensional color mapping can be extended to three-dimensions through tractography algorithms. Generally, tractography algorithms can be classified as either deterministic or probabilistic. Deterministic methods will be addressed here. These algorithms seek to recreate WM pathways by using the directional information in adjacent voxels to form coherent long-range patterns. The goal is to recreate the smooth continuous fiber pathways using the discrete voxels of DTI. From a given starting location, a direction of propagation is chosen and a step is taken. At this point, a new direction is determined and the process is repeated until a stopping criteria is met. Stopping criteria are typically anisotropy and curvature thresholds, (e.g. a tract will terminate when it meets a region with FA less than 0.2 or a curvature greater than 45 degrees over a length of 5 mm). Algorithms differ in the determination of the propagation direction and the step length. Figure 2.6 displays the transition from color map to tractography, as well as the stopping criteria.

The Fiber assignment by continuous tracking (FACT) algorithm uses the primary eigenvector as the propagation direction. Steps are defined from one voxel edge to another edge [19]. Other algorithms also use the same propagation direction with variable step lengths [20,21]. In areas with low FA, the ambiguity of the underlying fiber direction increases, thus, the primary eigenvector may not accurately reflect anatomy.

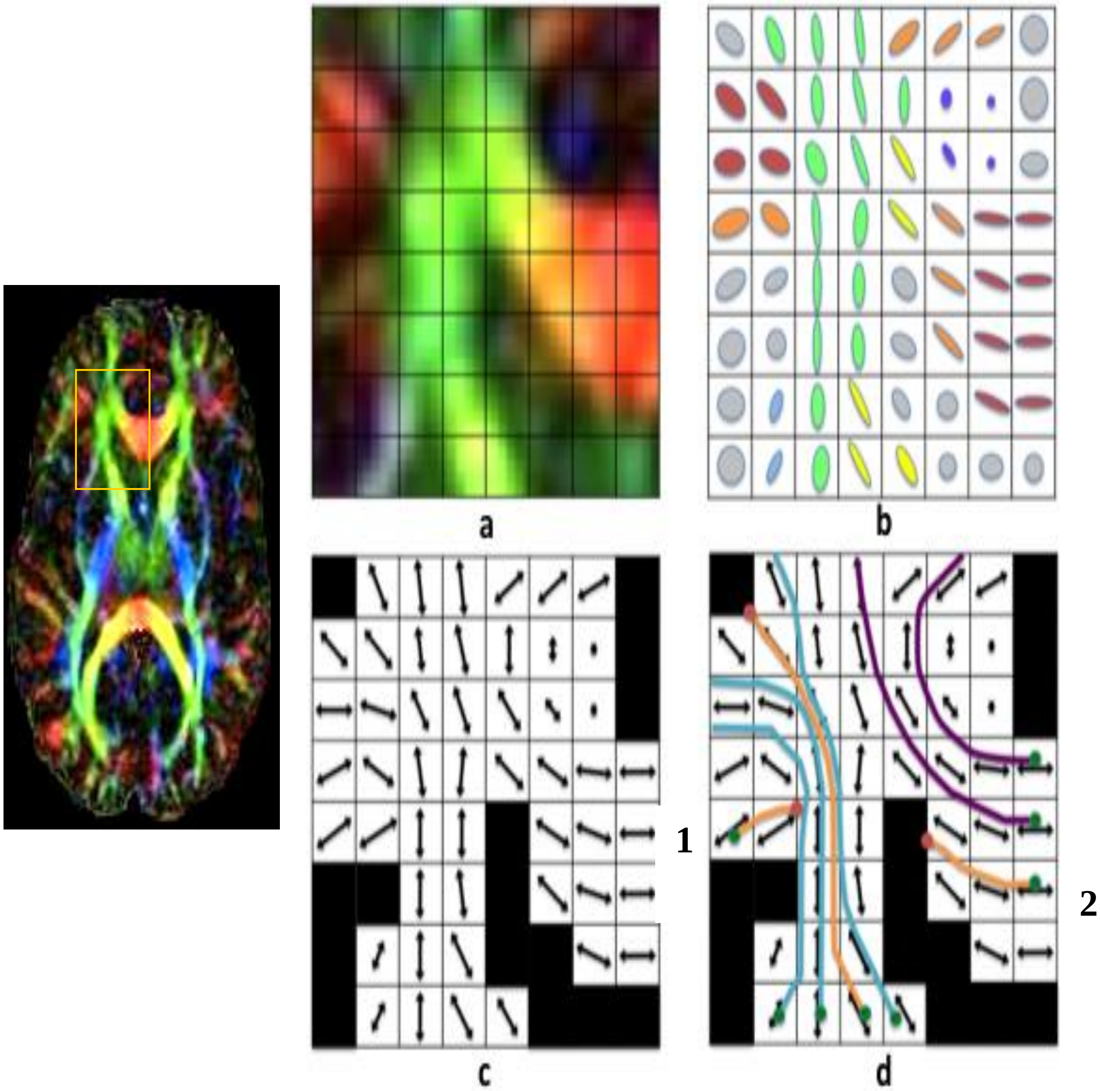

Figure 2.6: Representations of orientation information in DTI. A box centered on a region containing the genu of the corpus callosum and anterior limb of the internal capsule is expanded. A cartoon example of directional information is shown. Displayed here is the color map as described before (a), as well as ellipsoid glyphs (b) and vector map (c). Using the eigenvector information, the fiber trajectories may be estimated using tractography (d). The stopping criteria are illustrated in panel d. The tract marked 1 terminates when too great of a curvature is encountered, while tract 2 terminates upon entering an area of low anisotropy denoted by the black voxels. Adapted from [144].

Multiple inclusion and exclusion ROIs can be utilized to isolate specific tracts. Inclusion ROIs require that only tracts that pass through that region are visualized. Meanwhile, any tracts that pass through exclusion regions are not visualized. By careful placement, tracts can be visualized with a high degree of specificity. In practice most anatomical tracts require some combination of inclusion and exclusion ROIs. Figure 2.7 shows an example of defining tracts with multiple ROIs.

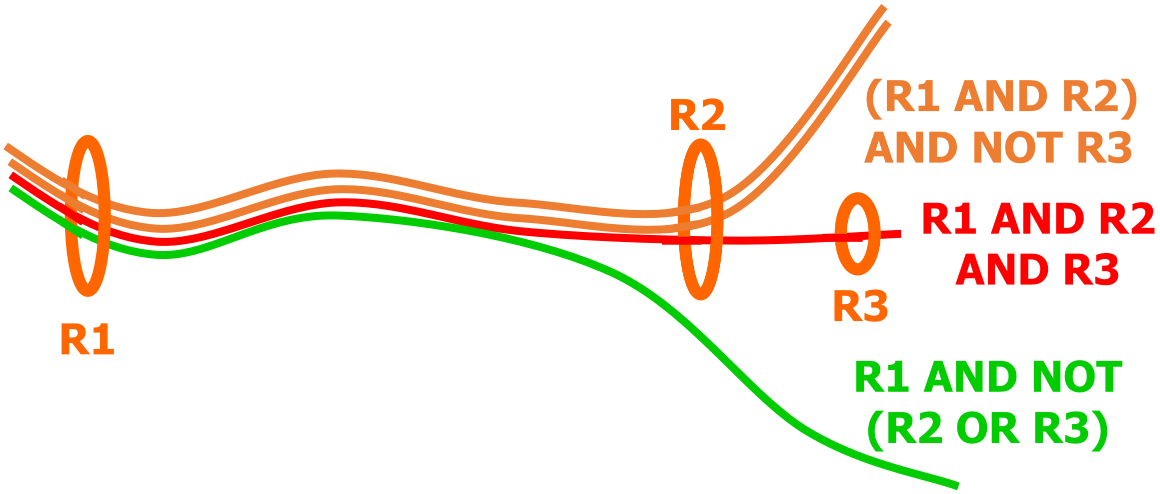

Figure 2.7: Different ROI operations. By defining which ROIs to include or exclude, three separate tracts are illustrated. Here "not" is used to denote an exclusion ROI. Adapted from [144].

A major application of tractography is the segmentation of specific pathways across multiple subjects. This allows diffusion measures such as FA and MD to be computed and compared for the same anatomical/functional region across subjects. An alternative to this approach is to draw ROIs on two dimensional slices. This is much more likely to result in the inclusion of voxels from adjacent areas and the exclusion of some desired anatomy.

2.4 Echo Planar Imaging

The diffusion weighting gradients induce a random spatially varying phase across the image. For this reason, acquiring an image across multiple excitations, as in conventional spin-echo and fast spin-echo imaging, can be problematic. Phase errors between excitations would accumulate and lead to signal voids and distortion throughout the image.

Clinical diffusion imaging is feasible thanks to echo planar imaging (EPI). There are alternative methods to EPI such as line scan [22], single-shot fast spin echo [23], spiral [24], radial [25], and PROPELLER [26] acquisitions. Although these have been used in research, each carries with it shortcomings which prevent widespread utilization. EPI remains the most advantageous combination of short acquisition time, high temporal signal to noise ratio, and relative insensitivity to motion.

Single shot EPI is capable of filling all of k-space after a single excitation. This is accomplished by producing a series of gradient echoes using bipolar readout gradients. All the while, T_2^* relaxation is occurring. Each of the alternating gradient lobes is separately phase encoded so that each leads to the acquisition of a single line of k-space. Figure 2.8 shows an example of the k-space trajectory followed by an EPI readout.

EPI sequences have important advantages but, they also provide constraints for the imaging process. While EPI is very rapid, the spatial resolution is limited. Also, off-resonance effects from static magnetic field inhomogeneities will lead to significant image distortions. Parallel imaging methods are commonly applied to reduce the amount of EPI distortion.

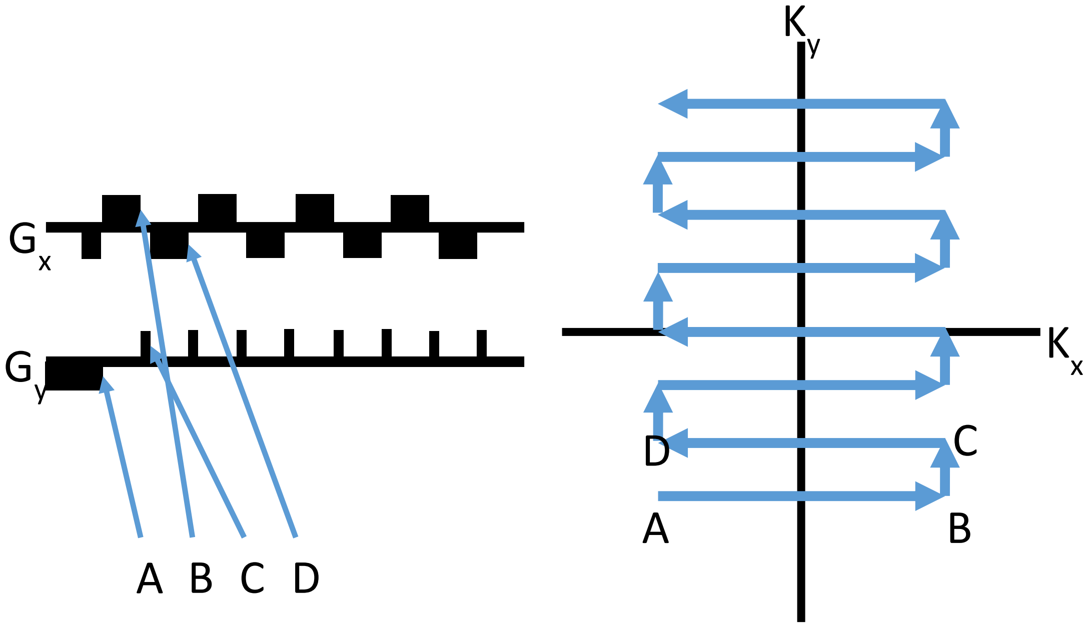

Figure 2.8: The k-space trajectory of EPI. Gx and Gy, respectively, denote the frequency and phase encoding gradients. The corresponding axes in k-space are given as Kx and Ky. The letters A, B, C, and D show the correspondence between the gradient pulses and the k-space traversal.

Another issue with diffusion-weighted EPI sequences is the residual eddy currents from the strong DW gradients. Commercial DW pulse sequences often include an option for bipolar diffusion gradients with a dual-refocused spin echo sequence [27]; however, that option significantly increases the echo time, which reduces the measurement signal to noise ratio (SNR). Eddy current induced distortions may be corrected using retrospective image registration tools that can also correct for head motion.

2.5 Partial Volume Effects

An effective means of reducing the artifacts and blurring associated with EPI imaging is to reduce the extent of k-space that is acquired. Thus, by reducing the image resolution, some detriments may be avoided and, most importantly, SNR is maximized. Diffusion images are inherently low SNR due to the EPI acquisition and the diffusion induced attenuation. As a result, diffusion studies are typically carried out with 2.5 – 3.5 mm isotropic resolution.

At typical DTI resolution, it is common to encounter partial volume effects (PVE). PVE occurs when a single voxel contains multiple different tissue types. In this case, the measured signal is a weighted average of the constituent components and does not accurately describe either tissue type.

In diffusion imaging, the properties of CSF are markedly different from the brain parenchyma. Additionally, the diffusion properties of CSF are not known to provide useful insight to any pathology and, thus, are of no research interest. However, much of the tissue adjacent to CSF is of research interest. As can be seen in Figure 2.9, fine structures adjacent to CSF are obfuscated due to the poor resolution.

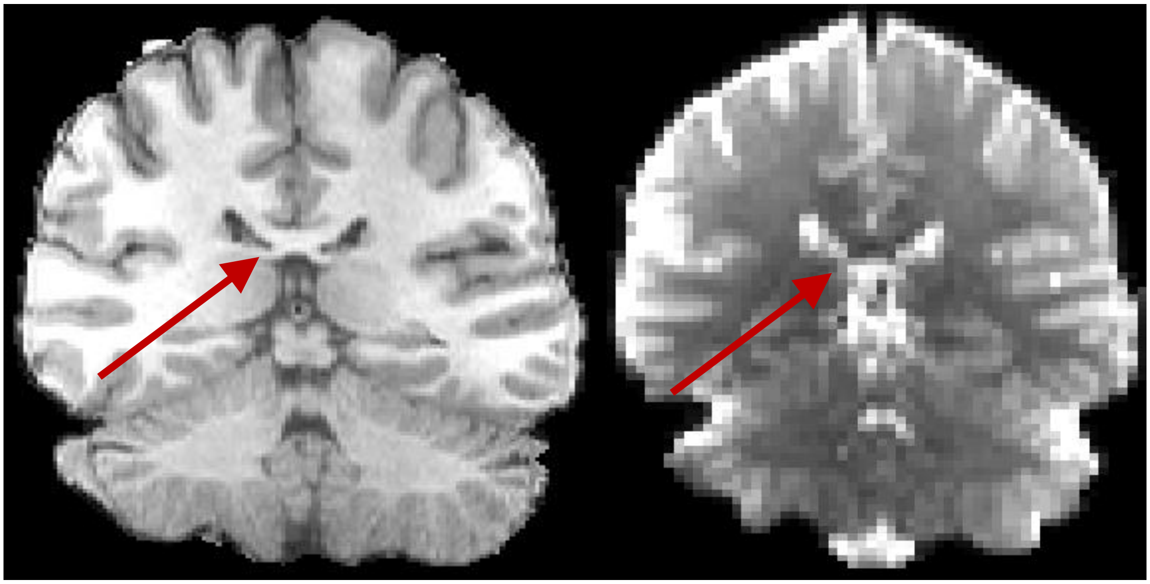

Figure 2.9: Partial volume effects in diffusion imaging. A T1 weighted image with 1 mm isotropic resolution, left, and a b = 0 diffusion weighted image with 2.5 mm isotropic resolution. In both images, the red arrow points to the fornix as it travels between two CSF filled regions. Although visible on the higher resolution image, this structure of interest in Alzheimer's disease is obscured due to PVE in the diffusion weighted image.

2.6 Fluid Attenuation Inversion Recovery (FLAIR)

By coupling the DTI sequence with a fluid attenuation inversion recovery preparation, deleterious PVE can be directly eliminated. The FLAIR preparation directly reduces the signal from CSF to nearly zero. In this way, voxels that contain some mixture of CSF and tissue will have their signal originating almost entirely from the tissue component.

Inversion recovery employs a 180 degree pulse and then some inversion time (TI) where magnetization is allowed to freely recover before the pulse sequence is further played out. FLAIR is simply inversion recovery with a TI such that the signal from CSF is nulled when the following pulses are applied. Following the inversion pulse, longitudinal magnetization is described below:

$$M_z(t) = M_0(1 - 2e^{-\frac{t}{T_1}})$$

where M_0 is the equilibrium magnetization and T_1 is the spin-lattice relaxation constant. Figure 2.10 shows the signal time course after an inversion for T_1 values representative of CSF, GM, and WM [28,29].

A consequence of nulling CSF signal is a reduction in the available signal from GM and WM by approximately 44% and 25% with a typical TI of 2200 ms. As the noise will remain unchanged, the SNR is degraded by the same factor.

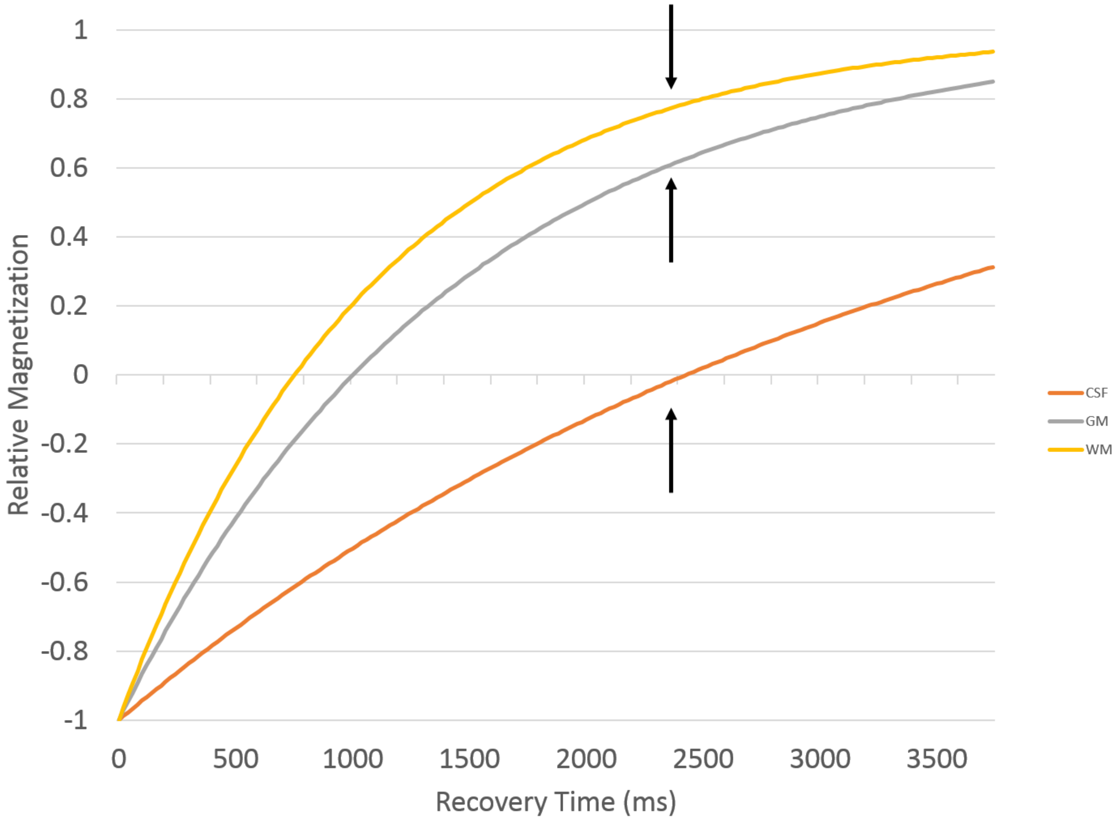

Figure 2.10: Evolution of the longitudinal magnetization after an inversion pulse. The arrow marks the recovery time when the CSF signal is nulled. At this point the typical diffusion sequence would begin. The available signal from white and grey matter is reduced by the incomplete recovery from the inversion pulse.

In addition to the loss in signal, a larger recovery time before the same slice can be excited again is required for sufficient regrowth of the longitudinal signal. When combined with the additional time for the TI, the scan has a significantly longer repetition time (TR) than a typical DTI sequence.

The last negative consequence of the FLAIR sequence is a reduced number of slices which can be acquired per TR. Though slices are interleaved, the TI required for FLAIR limits the total number of slices collected.

In this way, FLAIR effectively alleviates PVE, but it does so at the cost of SNR, time efficiency, and scan coverage. Therefore, for the same time interval, fewer diffusion directions and less anatomy can be acquired with a lower SNR. This work aims to use modeling to remove PVE without the negative effects imposed by the FLAIR preparation.

2.7 Alzheimer's Disease

Alzheimer's Disease (AD) is the most common form of irreversible dementia, occurring in 10% of those over 65 and approximately 50% of those over 85 [30]. The median lifespan following diagnosis is 4.2 years for men and 5.8 years for women, both well below the average lifespan for the Americans of the same age [31]. This neurodegenerative disorder has several behavioral and neuropathological hallmarks. Behavioral changes include inability to form new memories as well as visual and language deficits [32]. Common neuropathologies include atrophy of grey and white matter, myelin loss, deposition of β-amyloid plaques, and neurofibullary tangles.

There are numerous risk factors that may predispose an individual to developing AD. Family history of AD and possession of the apolipoprotein

E (ApoE) ε4 allele are known to be the two greatest risk factors. The gene for ApoE ε4 increases risk for development of AD by 5 to 15 times, depending on whether an individual possesses one or two copies [33]. Likewise, parental history of AD confers additional risk [34].

The involvement of WM in AD has been documented in postmortem human brains as well as *in vivo*. In mice it has been seen that WM effects are visible prior to beta amyloid deposition [35]. However, it is unknown whether this degradation is a primary event in the development of AD or if axonal regression is secondary to neuronal death (Wallerian degeneration). In either case, DTI's sensitivity to microenvironment allows for detecting group changes, even in preclinical AD.

In order to detect and characterize the onset of AD, it is necessary to study patients before the manifestation of clinical neurological deficits. With early imaging comes the added challenge of subtle effects. This study aims to image individuals who have no manifestation of symptoms, but do have some risk factor for the development of AD.

The FWE model has been used to assess microstructural changes in individuals with mild cognitive impairment [36]. Additionally, DTI metrics have been used in at risk individuals [37]. However, the FWE model has not yet been utilized in asymptomatic individuals. What has been noted is that FWE corrections change the magnitude and spatial patterns of group differences. The prior study utilized a voxel-based approach over a white matter mask.

The macroscopic and microscopic atrophy that is characteristic of AD makes it an intriguing application for FWE correction. The considerable amount of tissue loss leads to greater amounts of partial volume with CSF. The FWE model will aid in assessing the relation between atrophy and microstructural changes in the case of anomalous diffusion measures.

Chapter 3

The Free Water Elimination Model

Portions of this chapter have been published in the journal *NeuroImage* in September 2014 (Hoy AR, Koay CG, Kecskemeti SR, Alexander AL. Optimization of a Free Water Elimination Two-Compartment Model for Diffusion Tensor Imaging. Neuroimage (2014) 103:323–33).

3.1 Abstract

Diffusion tensor imaging is used to measure the diffusion of water in tissue. The diffusion properties carry information about the relative organization and structure of the underlying tissue. A single diffusion tensor is no longer appropriate in the case of a single voxel containing both tissue and a fast diffusing component such as free water. A two-tensor free water elimination model has been proposed to correct for the case of volume mixing. This model was implemented in a straightforward but novel manner. The optimal acquisition parameters were investigated through Monte Carlo simulations and human brain imaging studies. At a signal-to-noise ratio of 40 with 64 diffusion-weighted encoding images, most accurate estimates of fast diffusion signal were obtained with two diffusion-weighted shells (*b*-value in s/mm^2 x number of directions) of 500x32 and 1500x32. Using Bayesian information criteria, *in vivo* results show the free

water elimination model is superior to the traditional single component diffusion tensor model in representing the measured signal. The potential bias in fractional anisotropy induced by this two-compartment model was more than an order of magnitude less than the error of using the single diffusion tensor model in the presence of partial volume effects with free water. This strategy may be useful for characterizing the diffusion of tissues adjacent to cerebrospinal fluid (CSF) and tissues affected by edema, and removing artifacts from blurring and ghosting of the CSF signal.

3.2 Introduction

Diffusion weighted imaging (DWI) is a non-invasive magnetic resonance imaging (MRI) technique capable of measuring properties that describe the molecular displacements of water in biological tissues. Diffusion tensor imaging (DTI), an application of DWI, is used to quantify the three-dimensional movement of water with the assumption that simple Gaussian diffusion is a good descriptor of the water diffusion within a voxel [38]. The most common application of DTI is brain imaging. In this application the diffusion information is used to draw conclusions about brain architecture and microstructure. DTI has shown a great deal of utility in routine clinical use as well as in brain research [39].

The relative ease or resistance to diffusion along any single direction yields information about tissue structure and organization. Free water, which is characterized by uninhibited movement, displays isotropic diffusion and an apparent diffusion coefficient (ADC) of roughly 3 $\mathrm{x}10^{-3}\mathrm{mm}^2/\mathrm{sec}$ [40]. Meanwhile, more structured tissue such as white matter displays distinctly anisotropic diffusion. Free water in the brain exists as cerebrospinal fluid in the ventricles and bordering the parenchyma of the brain. Grey matter is characterized by a lower degree of anisotropy than white matter, as well as more hindered diffusion than CSF. GM and WM both have an ADC of approximately 0.8 $\mathrm{x}10^{-3}\mathrm{mm}^2/\mathrm{sec}$ [41].

The Free Water Elimination (FWE) model seeks to remove the deleterious effect of CSF partial volume effects on diffusion measurements. While the initial description of this two-compartment diffusion model described using multiple *b*-values [42], more recent implementations estimated the fast diffusing component using only a single *b*-value acquisition with local spatial constraints on the model [43]. However, the inclusion of these spatial constraints was seen to modify the direction of the eigenvectors. This approach is ill-posed without these constraints and assumptions. The FWE model is solvable using multiple *b*-value measurements, yet few studies have applied these schemes for DTI [44].

None of these implementations have undertaken a rigorous assessment of the accuracy of the FWE fitting. Likewise, a determination of the best acquisition parameters has not been investigated. This work sets out to determine the accuracy and reliability of the fitting as well as which acquisition is best suited to fitting the FWE model.

Recent work with more advanced diffusion models such as diffusion basis spectrum imaging (DBSI) [45], neurite orientation distribution diffusion imaging (NODDI) [16], multiple fascicle models [46], and combined hindered and restricted diffusion (CHARMED) imaging [47] has included an isotropic free water component in their models. While there is growing interest in these complex models of diffusion for characterizing brain tissue microstructure, the acquisition times are long and computational demands for these models are high relative to clinical DTI protocols. Thus, the simple DTI model with an additional fast diffusion compartment may provide a rapid and simple model for estimating and removing fast diffusion effects in many DWI studies.

This work sets out to develop a relatively simple, yet novel, method for estimating the fast diffusing component and the underlying tissue parameters. The DWI protocol for the FWE DTI model was optimized through successive simulations that took into account different experimentally realistic factors in the optimization. All the while, clinical feasibility, as defined by a maximum of 70 DWI measurements, was maintained. Thus, the number of gradient directions was fixed at 64 and 6 $b = 0$ images, which corresponded to a minimum whole-brain imaging time of 6 minutes and 30 seconds at 2.5 mm isotropic resolution on our MRI system.

3.3 Methods

In this section we introduce our two-compartment FWE DTI model and describe two independent yet complimentary methods to solve the FWE DTI model. The first method is a weighted linear least squares method using a brute force region contraction approach to solve for the free water component. Although not as robust or accurate as our second approach, this method has the advantage of being computationally efficient and serves well as either a stand-alone estimate or the initial guess for non-linear search methods. The second method is a modified Newton's method approach [48] with a dynamically adjusted dampening parameter to control step size and direction.

3.3.1 Free Water Elimination Model

Errors arise in DTI when the tissue within a single voxel is a mixture of multiple tissue types resulting in partial volume effects [40]. A two-compartment model has been used previously to estimate the diffusion characteristics of brain tissue in the presence of the partial volume effect with a fast diffusing component such as free water [42]. In the current work, the tissue compartment, which could be white or grey matter, is modeled as a tensor just as in DTI. The fast diffusing compartment is modeled as having isotropic diffusion with a fixed diffusivity equal to the theoretical expected diffusivity of unhindered water at body temperature. The relative signal contribution of the fast diffusing component is described by *f*, a scalar volume fraction. The free water elimination DTI signal model is described by

$$S_i = S_0[(1-f)\exp(-b_i g_i^T D g_i) + f exp(-bD_{iso})]\exp(-\frac{TE}{T2}) \qquad (3.1)$$

where S_i and S_0 are the signal from the i-th diffusion and non-diffusion weighted measurements, respectively, D_{iso} = 3 x10^{-3}mm^2/sec is the free water diffusivity, $\boldsymbol{D}$ is the tissue diffusion tensor, b_i and g_i are the diffusion-weighting amplitude (in mm^2/s) and unit gradient encoding vector, respectively, and *TE* is the echo time that prescribes the amount of *T2* (transverse relaxation) decay. This two-compartment model is attractive because of its similarity to DTI. The tissue signal compartment results in the same scalar metrics of DTI, even preserving the direction of the eigenvalues. The addition of the isotropic compartment is intended to compensate for confounding partial volume effects from CSF and also edema. This will improve the ability to characterize tissue parenchyma microstructure in voxels with partial volume averaging and multiple diffusion components.

3.3.2 Fitting Procedures

Initially, the tissue compartment tensor was fit using a weighted linear least squares (WLLS) region contraction approach. This was accomplished by recasting equation 3.1 as equation 3.2 and performing the estimation for a fixed f value.

$$\frac{S_i - S_0 f exp(-b_i D_{iso})}{(1-f)} = S_0 \exp(-b_i g_i^T D g_i) \tag{3.2}$$

It should be noted that the T2 weighting term was dropped as TE was held constant within a single acquisition. Thus, the signal variations were considered to be solely due to differential diffusion weighting. For each selected *f*, the WLLS estimation was then carried out [48]. For a single fixed value of *f* and keeping D_{iso} = 3 x10^{-3} mm^2/s as a constant, the only unknown remaining was *D*, the diffusion tensor. This was fit simply with a weighted linear least squares routine. The net result was a diffusion tensor that best fit the measured data for a corresponding volume fraction. This procedure could be carried out for a range of *f* between 0 and 1.

Once a (*f*, *D* tensor) pair was calculated, the weighted linear least squares objective function, equation 3.3, was used to judge which (*f*, *D* tensor) best fit the measured data. A better data fit will result in a smaller objective function. Thus, by systematically fitting diffusion tensors to many volume fractions and then evaluating which (*f*, *D* tensor) minimizes the objective function, it is possible to determine the isotropic volume fraction and the tissue compartment tensor that best represents the measured data.

$$F_{WLLS}(\gamma) = \frac{1}{2}\sum_{i=1}^{m} \omega_i^2 \left(y_i - \sum_{j=1}^{7} W_{ij}\gamma_j\right)^2 \tag{3.3}$$

$i = 1,\cdots,m$

m = the number of images obtained

s_i = the measured signal including noise

ω_i = the weights for each image = s_i

$$W = \begin{pmatrix} 1 & -b_1 g_{1x}^2 & -b_1 g_{1y}^2 & -b_1 g_{1z}^2 & -b_1 g_{1x} g_{1y} & -b_1 g_{1y} g_{1z} & -b_1 g_{1x} g_{1z} \\ \vdots & \vdots & \vdots & \vdots & \vdots & \vdots & \vdots \\ 1 & -b_m g_{mx}^2 & -b_m g_{my}^2 & -b_m g_{my}^2 & -b_m g_{mx} g_{my} & -b_m g_{my} g_{mz} & -b_m g_{mx} g_{mz} \end{pmatrix}$$

To ensure the proper volume fraction is identified would require many small steps from zero to one. This process can be cumbersome and time consuming. However, the WLLS routine was further modified so that multiple volume fractions could be fit simultaneously. Furthermore, it was seen that the total number of fittings was greatly reduced by systematically refining the size of the Δf step.

This was implemented by simultaneously solving for the diffusion tensor with multiple f-values. Initially, a coarse Δf step size of 0.1 was used over the range from zero to one. The objective function for each of these initial eleven (f, D tensor) pairs was evaluated with the lowest value being passed on as the best estimate. The next iteration used steps of 0.01 over the range of the previous best estimate ± .05. A third step reduced the step size by another order of magnitude. This method did not display any drop off in estimation accuracy compared to the use of an initial step size of 0.001. However, the series of refined steps reduced the number of WLLS estimations from 1001 to 31 per voxel. Figure 3.1 shows two steps in the region contraction approach using *in vivo* data from a single voxel.

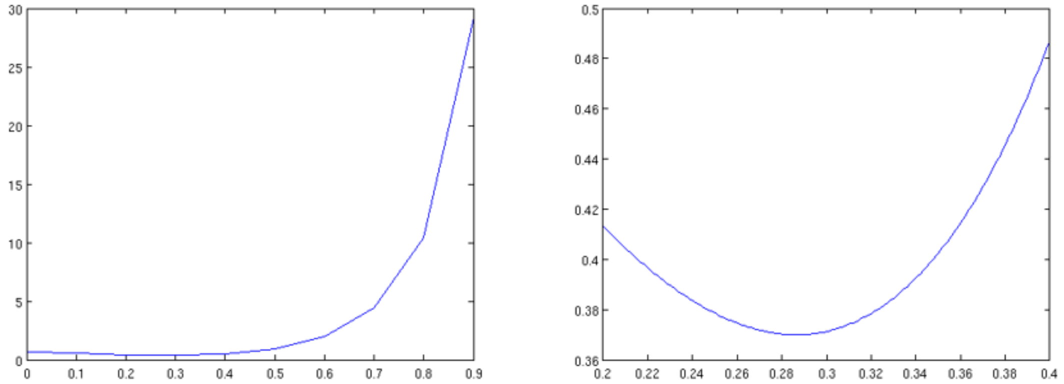

Figure 3.1: The first two steps of the region contraction approach. Both graphs have the objective function value on the vertical axis and the presumed f value on the horizontal axis. The graph on the left uses presumed values from 0 to 1 in steps of 0.1 and has a minimum value at 0.3. The right graph is from the same data with the presumed value limited from 0.2 to 0.4 but with fine steps in f.

The WLLS routines for DTI and FWE-DTI are similar as both share the same objective function with some modification.

There are two conceptual differences in the WLLS routines and both are manifest in the definition of y. As discussed earlier, the equation is recast to account for the isotropic compartment that leads to a change in the definition of y. Also, while DTI solves for a single parameter vector (γ), the FWE-DTI method solves for n-parameter vectors, each determined for a specific f-value. In DTI y is an m x 1 vector where m is the number of images. This is modified in FWE to be an m x n matrix where n is the number of f-values to be fit simultaneously.

DTI:

$$y_i = \ln(s_i)$$

$$y = [y_1, \dots, y_m]^T$$

$$\gamma = \left[\ln(s_0), D_{xx}, D_{yy}, D_{zz}, D_{xy}, D_{yz}, D_{xz}\right]^T$$

FWE-DTI:

$$y_{ik} = \ln\left\{\frac{s_i - s_0 exp(-bD_{iso})}{(1 - f_k)}\right\}$$

where k = 1, ⋯, n

n = the number of f-values fitted simultaneously

$$y = \begin{bmatrix} y_{11} & \cdots & y_{1n} \\ \vdots & \ddots & \vdots \\ y_{m1} & \cdots & y_{mn} \end{bmatrix}$$

$$\gamma = [\gamma_1, \cdots, \gamma_n]$$

To solve for ɣ:

$$\gamma = (W^T S^2 W)(SW)^T Sy$$

where S is a diagonal matrix with the measured diffusion signal as the nonzero elements:

$$S = \begin{pmatrix} s_1 & & \\ & \ddots & \\ & & s_m \end{pmatrix}$$

The volume fraction and fitted tensor pair that minimized the WLLS objective function were passed on as the initial estimate for a nonlinear fitting. The nonlinear optimization used a modified Newton's method approach [48] that explicitly calculated the Hessian at each iteration. In the context of diffusion tensor estimation, the inclusion of the full Hessian matrix has been shown to be superior [48]. The definition of the dual compartment nonlinear least squares (dcNLS) objective function for the FWE model, its gradient vector, Hessian matrix, and search step vector are shown below.

$$F_{dcNLS} = \frac{1}{2}\sum_{i=1}^{m}\left(s_i - (1-f)exp\left(\sum_{j=1}^{7} W_{ij}\gamma_j\right) - f s_0 exp(-bD_{iso})\right)^2$$

$$\nabla F_{dcNLS} = \left[\frac{\partial F}{\partial f}, \frac{\partial F}{\partial \gamma_1}, \cdots, \frac{\partial F}{\partial \gamma_7}\right]$$

$$\nabla^2 F_{dcNLS} = \begin{pmatrix} \frac{\partial^2 F}{\partial^2 f} & \frac{\partial^2 F}{\partial f \partial \gamma_1} & \cdots & \frac{\partial^2 F}{\partial f \partial \gamma_7} \\ \frac{\partial^2 F}{\partial \gamma_1 \partial f} & \frac{\partial^2 F}{\partial^2 \gamma_1^2} & \cdots & \frac{\partial^2 F}{\partial \gamma_1 \partial \gamma_7} \\ \vdots & \vdots & \ddots & \vdots \\ \frac{\partial^2 F}{\partial \gamma_7 \partial f} & \frac{\partial^2 F}{\partial \gamma_7 \partial \gamma_1} & \cdots & \frac{\partial^2 F}{\partial^2 \gamma_7^2} \end{pmatrix}$$

$$\delta = -(\nabla^2 F_{dcNLS} + \lambda I)^{-1} \nabla F_{dcNLS}$$

Here λ is the Levenberg-Marquardt parameter and I is an identity matrix of the same dimensions as the Hessian. This parameter dampens the search step with larger λ values corresponding to greater dampening and $\lambda = 0$ simply being Newton's method. The dampening allows for an increased likelihood of convergence over Newton's method when the initial parameter estimates are far from the true minima. When the initial estimate is near the minima, a smaller λ and, thus, less dampening will result in faster convergence. The exact definition of small and large λ is relative to the values in the Hessian. Further details on the values used and other implementation details can be found at the end of this section.

After each step that reduced the nonlinear objective function, λ was reduced by dividing it by some incremental factor (λ_{inc}), which was a positive number greater than one. If the step increased the objective function, then it was rejected and λ was increased by multiplying by λ_{inc}. Based on an estimate of the goodness of fit of the initial parameters determined by the WLLS fitting, a certain λ and λ_{inc} were set for the nonlinear fitting. It has been shown [48] that an unbiased estimate of the diffusion signal variance is formed by $\sigma_{DW}^2 = \frac{2F(\hat{\gamma})}{v}$, where $v = m - p$ is the number of degrees of freedom; m is the number of samples; p is the number of parameters being fit. Thus, an estimate of the signal to noise ratio, here called the pseudo signal to noise ratio (SNR_p), can be defined as $SNR_p = \frac{S_0}{\sigma_{DW}}$, where S_0 is the average signal of the $b = 0$ acquisitions. This SNR_p measure was used to determine the goodness of fit of each initial estimate.

It was also necessary to reinitialize some voxels prior to the nonlinear fitting. It was observed that high isotropic volume fractions ($f > 0.7$) occasionally were fit by WLLS with an estimated $f < 0.05$ and a nearly isotropic tensor with a mean diffusivity slightly below the fixed value of 3 $\times 10^{-3}$ mm^2/s. Therefore, any voxel with a tensor-compartment mean diffusivity greater than 1.5 $\times 10^{-3}$ mm^2/s was reset as having an f-value of 0.5 and its tensor components divided by two. Though this also represented a crude initial estimate, it was an improvement in the case of the WLLS fit procedure failing. This relative weakness in the WLLS fitting is remedied in the NLS fitting as is evident by the small estimation bias and standard deviation in the Results section.

Presented here is the algorithm employed for the nonlinear fitting. It is broken up into the steps that took place prior to the first iterations, and the body of the algorithm, which is iterated until convergence. While values are given for the Levenberg-Marquardt parameters, these may not be generally applicable. The proper values are dependent on the specific data set and will need adapting to achieve efficient and robust algorithm performance.

Before the first iteration:

```
1. If ($MD_{tensor} > .0015\ mm^2/s$) {
       f = 0.5
       tensor = tensor/2
       }
2. Calculate $F(\gamma_k)$
3. Calculate $SNR_p$
4. If ($SNR_p < 20$) {
       $\lambda = 1*10^8$
       $\lambda_{inc} = 1.1$
   } Elseif ($SNR_p < 30$) {
       $\lambda = 1*10^7$
       $\lambda_{inc} = 2$
   } Else {
       $\lambda = 1*10^7$
       $\lambda_{inc} = 5$
```

At the kth iteration

```
1. If ($k > k_{max}$ or flag==false) exit
2. Solve $(H(\gamma_k) + \lambda I)\delta_k = -\nabla F(\gamma_k)$ for $\delta_k$
3. If ($F(\gamma_k + \delta_k) < F(\gamma_k)$){
       If ($|F(\gamma_k + \delta_k) - F(\gamma_k)| < \varepsilon_2$ and $0 \le -\delta_k^T \nabla F(\gamma_k + \delta_k) < \varepsilon_3$){
           flag == false
       } Else {
           $\lambda = \lambda/\lambda_{inc}$
           Accept $\delta_k$ by setting $\gamma_{k+1} = \gamma_k + \delta_k$
       }
    } Else {
           $\lambda = \lambda*\lambda_{inc}$
           Reject $\delta_k$ by setting $\gamma_{k+1} = \gamma_k$
           }
```

Where ε_1, ε_2, and ε_3 are small positive numbers and k_{max} is the maximum number of iterations.

3.3.3 Acquisition Optimization

Simulations were initially conducted to explore the range of *b*-values for designs with 2, 3, 4, 6, 8, and 16 different shells that produced the best (*f*, *D* tensor) pair. The total number of nonzero directions were fixed at 64 and the number of directions in each shell was kept as even as possible. Any additional directions were assigned to the highest *b*-value. Thus, the two-shell design featured 32 directions per shell, while the 3-shell design had a shell structure of 21/21/22 directions. The *b*-values were linearly spaced between the minimum and maximum value for each scenario. The distribution of directions for each shell was determined using the sparse and optimal acquisition method [49].

The minimum *b*-values investigated varied from 200 to 800 sec/mm^2 in increments of 100 sec/mm^2. Two-hundred was established as the minimum *b*-value to ensure that perfusion effects were avoided [50]. The maximum *b*-value varied from 300 to 1500 sec/mm^2, once again in steps of 100 sec/mm^2. The maximum *b*-value was always at least 100 sec/mm^2 greater than the minimum value. Also, the outer shell was limited to no higher than 1500 s/mm^2 to minimize non-Gaussian diffusion effects in the signal [15].

Data was simulated utilizing the two-compartment model with *f* fixed at 0.5. The choice of this *f*-value was to create a scenario that balances the effect of parenchymal tensor and CSF isotropic compartments. At any extended interface between CSF and tissue, the distribution of *f* values will have a mean of 0.5. Thus, the intention was to avoid bias of the optimization towards high or low *f*-values.

Two separate tensor shapes were considered independently. First, a prolate tissue compartment tensor shape was considered. The eigenvalues were $\lambda_1 = 1.6 \times 10^{-3}$, $\lambda_2 = 0.5 \times 10^{-3}$, and $\lambda_3 = 0.3 \times 10^{-3}$ mm^2/sec. The tensor had a trace of 2.4×10^{-3} mm^2/sec and a fractional anisotropy (FA) value of 0.712. These values were chosen as representative of voxels in a major white matter pathway such as the corpus callosum.

Additionally, an isotropic tensor was examined. Like the prolate tensor, this tensor had a trace of 2.4×10^{-3} mm^2/sec, however, its eigenvalues were $\lambda_1 = \lambda_2 = \lambda_3 = 0.8 \times 10^{-3}$ mm^2/sec. While these two tensors were used for determination of the optimal acquisition, additional tensors were simulated to characterize the performance of the reconstruction. These tensors maintained a trace of 2.4 x10^{-3} mm^2/sec with FA increments of approximately 0.1 from 0 to 0.8.

The metrics used to judge estimation accuracy were the mean squared errors (MSE) of FA, trace, and *f*. Mean squared error was a convenient metric because of its incorporation of both the bias and variance of the estimator, $MSE = \frac{1}{n}\sum_{i=1}^{n}\left(Y_i - \hat{Y}_i\right)^2$, where n is the number of measurements, Y_i is the true parameter value, and $\hat{Y}_i$ is the estimated parameter. For an estimator, MSE is equivalent to the sum of the variance and squared bias of the estimator [51].

Monte Carlo simulations were conducted where the ideal signal was corrupted with Rician noise across a plausible range of signal to noise ratios (SNR) as established by Pierpaoli and Basser [52]. The SNR was set relative to the *b* = 0 image. To ensure rotational invariance, each synthetic tensor was simulated in 120 unique orientations evenly spaced about a hemisphere. At each tensor orientation, 100 iterations were performed.

Once the optimal *b*-values were determined for each design, a more thorough characterization of estimation performance was carried out. This was accomplished by investigating a range of *f*-values from 0 to 1 in increments of 0.1 and SNRs from 20 to 60 in increments of 10. Once again, 100 iterations for each of the 120 orientations were performed for each SNR and *f*-value.

The largest b-value determines the minimum echo time (TE), which induces T2 signal attenuation. In a single acquisition or simulation, the TE remained constant to mitigate any confounding signal variations. However, when comparing two separate acquisitions, it is imperative to consider the drop in overall SNR associated with higher b-values. Though a rough estimate may be achieved with reasonable assumptions, the exact change in signal depends on the T2 of the tissue and a number of factors that determine the TE. Here, a single T2 is assumed. Using TE values recorded from our 3T scanner (MR750, GE Healthcare, Waukesha, WI) and an approximate white matter T2 of ≈ 70 ms at 3T [29], a relative SNR scaling factor was established to correspond to the largest b-value. While the nominal SNR was 40, the simulated SNR for max-b = 500 was larger than that of the simulation with max-b = 1500. The nominal SNR was set such that max-b = 1000 had a scaling factor of unity.

To arrive at a “best” acquisition, the MSE for each *f*-value was weighted by the frequency of occurrence of that *f*-value *in vivo*. An *in vivo* data set was used to determine the frequency of each *f*-value in bins of 0.1 to match the simulated *f*-values. This frequency was normalized such that the sum of all bins was one. Table 3.1 contains the weights obtained from a single healthy volunteer. These values were averaged from the two-shell and eight-shell acquisitions. The relative frequency was then used as a weighting for each MSE to allow for a single weighted mean squared error (wMSE) for each acquisition that reflects the expected global performance of the acquisition.

To investigate the effect of directional organization (i.e. how many independent directions are in each shell) the "best" design (i.e. optimal number of b-values) was simulated, letting the distribution of directions in each shell vary along with the minimum b-value while keeping the total number of directions 64.

Once an 'optimal' acquisition was established, the effects of tensor selection were investigated. This was done by using the same simulation set up as in the second step above with different underlying tensors. The first experiment held the FA constant while scaling MD in increments of 0.5 $\times10^{-4}$ mm^2/s from 5 $\times10^{-4}$ mm^2/s to 8 $\times10^{-4}$ mm^2/s. The second experiment held the MD constant at 8 $\times10^{-4}$ mm^2/s while varying FA in increments of ≈ 0.1 from 0.4 to 0.8.

Table 3.1: *In vivo* distribution of *f*-values. The relative frequency of *f*-values within the brain of a healthy volunteer. These values were used to weight the MSE values to calculate a single wMSE for each acquisition.

f-value bins	Relative frequency
<0.5	0.14
0.05 - 0.15	0.26
0.15 - 0.25	0.27
0.25 - 0.35	0.1
0.35 - 0.45	0.05
0.45 - 0.55	0.04
0.55 - 0.65	0.03
0.65 - 0.75	0.03
0.75 - 0.85	0.02
0.85 - 0.95	0.01
>0.95	0.04

3.3.4 Model Insufficiencies / Acquisition Effects

The effects of using an incorrect underlying model and a non-standard acquisition were investigated. This included the case where a standard DTI acquisition and estimation was used when the underlying data was actually the two-compartment model. The effect of using the free water elimination method and the optimized acquisition when the underlying signal was generated with a DTI model was also investigated.

For the standard DTI acquisition, a single non-zero *b*-value of 1000 s/mm^2 was used for all 64 unique gradient directions along with six $b = 0$ images. The FWE acquisition was the optimized acquisition as determined by the simulation steps. The simulations were carried out in the manner discussed above. The gradient directions for the DTI and FWE scans were the same.

3.3.5 Example Human Brain

A single healthy volunteer was scanned with the optimized protocol. This design was repeated twice in each of two sessions conducted a day apart. All scanning was performed using informed consent and in compliance with an approved protocol from the Institutional Review Board. Diffusion scans were performed with a 3-T MR750 Discovery scanner (General Electric Medical Systems, Milwaukee, WI) and an 8-channel head coil. MR parameters for the optimized scan were TE = 68.9 ms, TR = 5600 ms, acquisition matrix = 96 x 96, number of slices = 50, voxel size = 2.5 x 2.5 x 2.5 mm^3, and scan time = 6:30 min. Diffusion parameters were Δ = 24.0ms and δ = 18.0ms. The image was then interpolated in the axial view to a matrix of 256 x 256 and a display resolution of 0.94 x 0.94 x 2.5 mm^3.

3.3.6 Model Comparison

To statistically assess the FWE model in comparison to the standard DTI model, the Bayesian information criterion (BIC) was used to judge the two models against one another in-vivo. BIC determines the effectiveness of a model by its ability to minimize some objective function while simultaneously penalizing a model for an increasing number of parameters. Equation 3.4 shows the selection criteria:

$$BIC = -2\log(L) + Klog(N) \tag{3.4}$$

where L is the sum of the squared error, K is the number of free model parameters, and N is the total number of measurements. The implementation of the FWE model is such that L will always be smaller than or equal (when $f = 0$) with DTI, however, it also has one additional free parameter.

3.4 Results

The first step of optimization was to establish the *b*-values for each acquisition scheme with different numbers of shells that minimized the mean square error (MSE). Table 3.2 contains a summary of each design including number of shells, *b*-values for each shell, and the number of directions in each shell. A general trend is seen where the optimal minimum *b*-value decreases with increasing number of shells. For each design, the optimal outer shell was the highest one simulated (1500 s/mm^2).

Number of Shells	*b*-values (s/mm^2)	Directions per Shell
2	500/1500	32 per shell
3	500/1000/1500	21/21/22
4	400/767/1133/1500	16 per shell
6	400/620/840/1060/1280/1500	10/10/10/10/10/14
8	300/471/643/814/986/1157/1329/1500	8 per shell
16	300/380/460/540/620/700/780/860/940/1020/1100/1180/1260/1340/1420/1500	4 per shell

Table 3.2: "Optimal" acquisition designs. The different designs that minimized MSE in the first step of optimization and were subsequently used for the second step of optimization.

Figure 3.2 illustrates the effects of varying the minimum and maximum *b*-values on the model MSE. The two-shell design is shown here, however, each acquisition results in a similar pattern. This step determined the best set of *b*-values for a given number of shells. At this point no conclusion can be drawn about the "best" acquisition. The metric most sensitive to *b*-value was *f*-value, while FA and trace were less sensitive to *b*-value. However, within a single acquisition the same set of *b*-values produced the best performance for each of the three metrics.

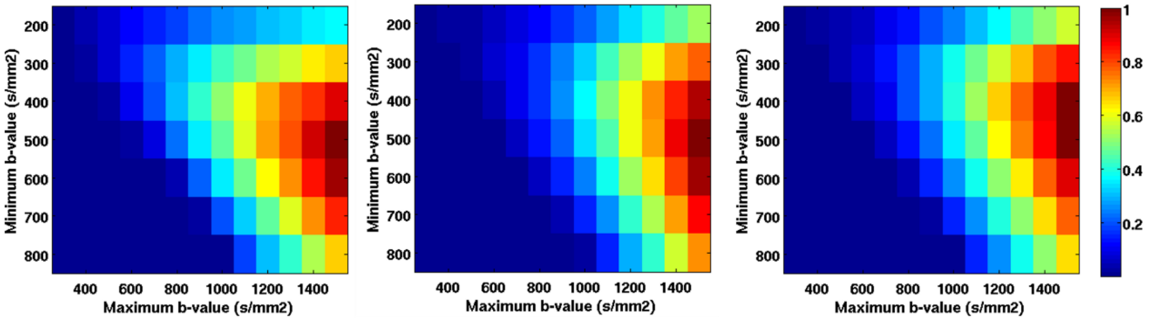

Figure 3.2: Determination of the optimal b-values for different number of shells. The scaled reciprocal of MSE corresponding to a certain minimum and maximum *b*-value (the value of 1 denotes the smallest MSE). MSE was evaluated for *f*-value (left), FA (middle), and trace (right). This set of images corresponds to the two *b*-value simulations. Though not shown, the other acquisitions produced similar patterns.

Figure 3.3 shows the effect of letting both the *b*-value and number of directions vary for the lower shell of the two-shell design. The lowest MSE was associated with a two-shell design with b-values of 500 and 1500 s/mm^2 and 32 directions each. The results shown here correspond to the case of the prolate tensor. Though not shown, the same acquisition design yielded the lowest MSE for the isotropic tensor as well.

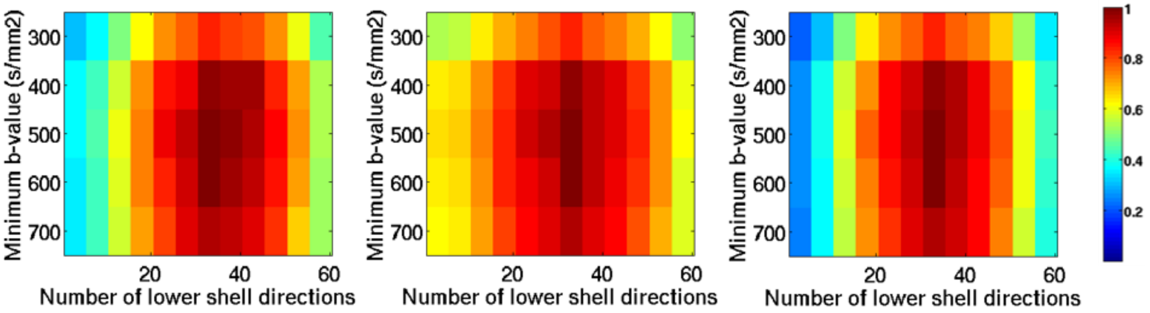

Figure 3.3: The scaled reciprocal of MSE, as in Figure 3.2, corresponding to a certain lower shell b-value and number of directions for the prolate tensor. MSE is shown for the *f*-value (left), FA (middle), and trace (right). The simulated acquisition had two-shells with the higher shell fixed at b = 1500 s/mm^2. The combined number of diffusion directions was held constant at sixty-four.

The next optimization step examined the effect of varying SNR and *f*-value on the MSE of each metric. Here the two-shell acquisition is seen to be superior for estimation in every situation investigated (see Figure 3.4). This design resulted in the lowest MSE regardless of *f*-value or SNR simulated.

Figure 3.5 shows the mean and standard deviation of the estimated FA and *f*-values for the simulation with SNR = 40. Here it is seen that despite accurate estimation of the *f*-value that the FA was biased to larger values as the simulated *f*-value increased. The bias was greatest for the isotropic tensor. The bias was larger for lower FA values. Table 3.3 shows the results of linear regression on the fit of the estimated *f*-value with increasing simulated *f*-value.

FA	**Slope**	**Intercept**	**R^2**
0.00	0.9927	0.0073	0.9986
0.11	0.9932	0.0069	0.9986
0.21	0.9927	0.0071	0.9986
0.30	0.9933	0.0067	0.9986
0.71	0.9966	0.0042	0.9998

Table 3.3: Linear regression on the fit of *f*-value for the tensors with varying FA.

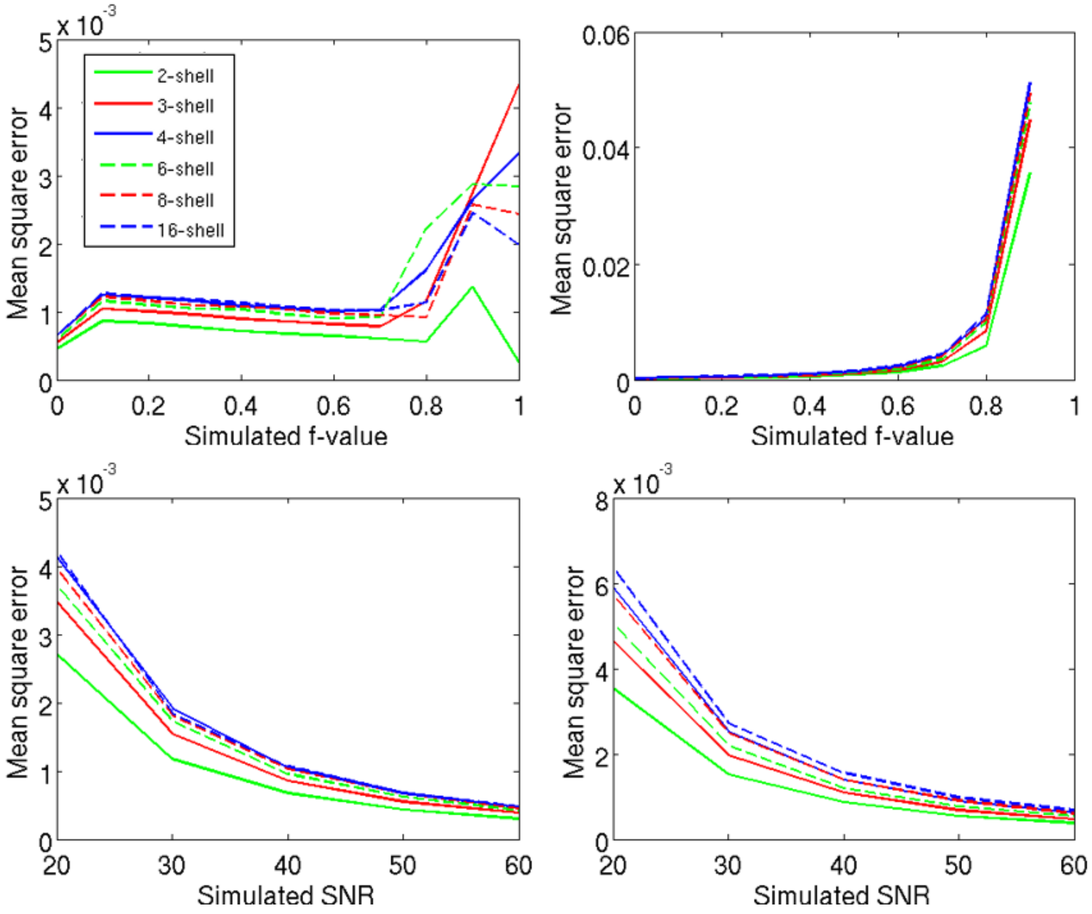

Figure 3.4: Characterization of performance for estimation of FA, left column, and *f*-value, right column, for the prolate tensor. The first row depicts MSE with increasing *f*-value while SNR = 40 for the various acquisitions tested. The second row shows MSE with increasing SNR for *f* = 0.5, the same acquisitions as above are displayed.

A clear effect of diffusion tensor MD and FA was seen in simulations (Figure 3.6). Here it was noted that for a fixed FA estimation MSE was reduced with decreasing MD. Meanwhile, when MD was held constant, MSE decreased with increasing FA.

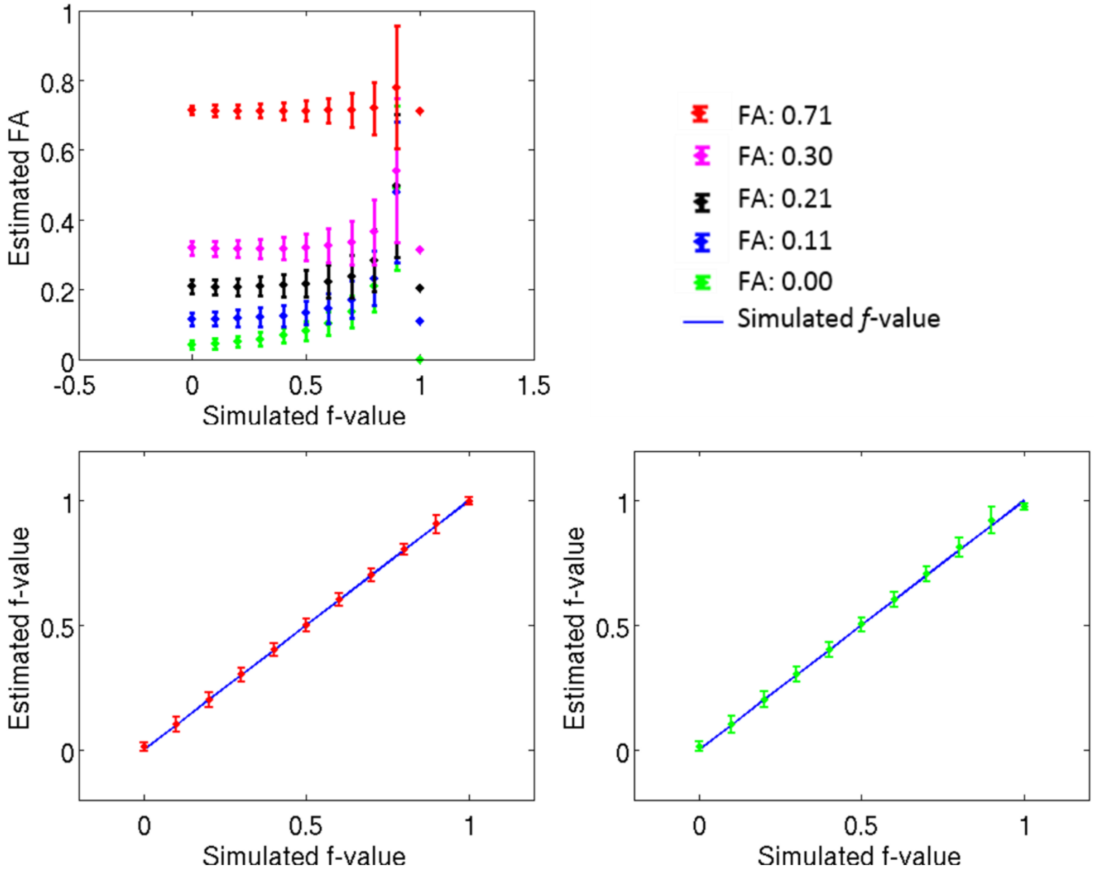

Figure 3.5: Estimation performance shown as mean ± standard deviation from simulations using the two-shell acquisition shown vs. increasing simulated *f*-value. The top image shows estimated FA for various tensor shapes. The points on the right indicate the true simulated FA values. The bottom row shows estimated *f*-value vs. increasing simulated *f*-value for the two cases used for optimization (red: FA= 0.71 and green: FA = 0.00).

Figure 3.7 shows several images from the same axial slice in a healthy volunteer. A T1-weighted anatomical image is provided for reference along with FA and MD maps from standard DTI and FWE. Additionally, a free water fraction map and FA and MD difference map are included.

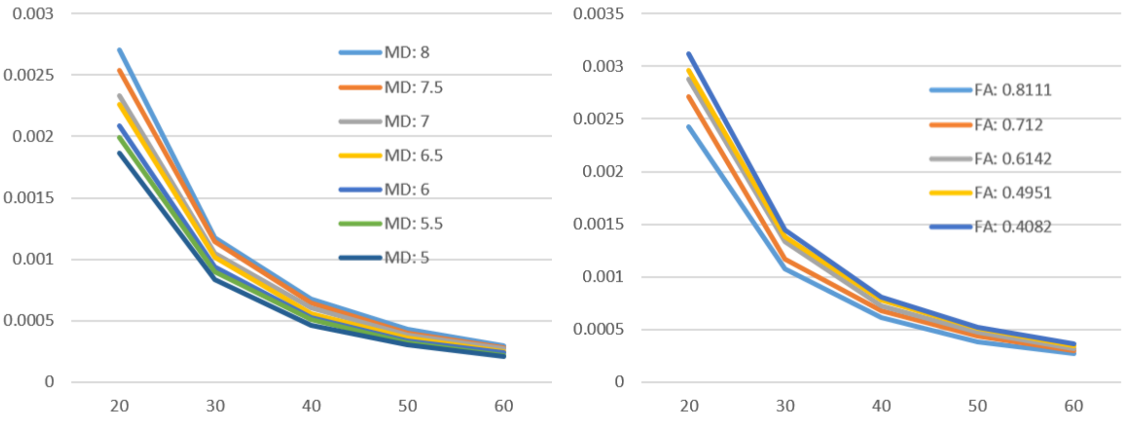

Figure 3.6: The effect of estimating tensors with different MD (left image) and FA (right image) on MSE with increasing SNR and f fixed at 0.5.

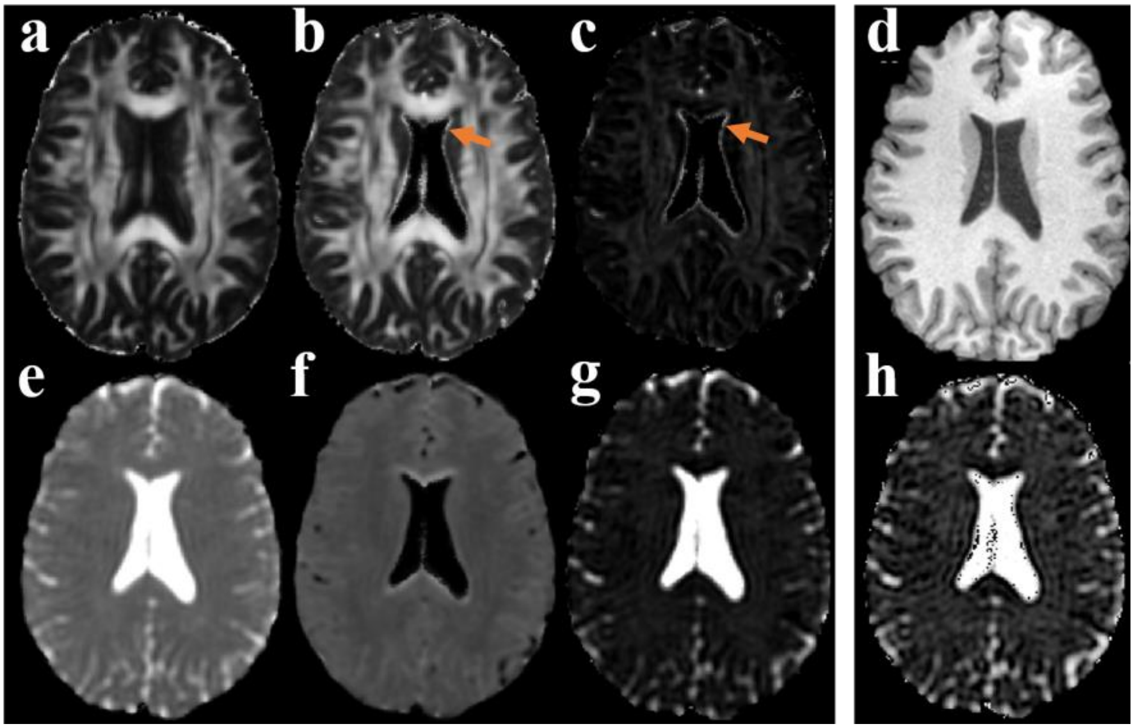

Figure 3.7: DTI and FWE metrics from an example human brain. The same axial slice with many contrasts. The first three images consist of FA from DTI (a) and FWE (b) along with the FWE FA minus the DTI FA (c) showing the pattern of increasing FA with FWE. Below these are the MD from DTI (e) and the FWE tensor (f) along with the DTI MD minus the FWE MD (g), which shows the reduced MD in the FWE tensor compartment. A T1w image is included for anatomical reference (d). The isotropic volume fraction (h) is shown as well. The arrows highlight artificially high FA in periventricular GM.

A joint histogram of FA and MD across the whole brain, as well as WM and GM segmented regions, illustrates the removal of CSF partial volume effects (Figure 3.8). The MD is not only reduced, but the distribution becomes narrower, losing its tail of high diffusivity, low FA voxels as evidenced by the reduction in standard deviation in MD for both WM and GM, Table 3.4. The reduction of voxels with CSF partial volume averaging is shown in a sagittal image in Figure 3.9. Here voxels with MD intermediate to parenchyma and CSF are considered as partial volume voxels.

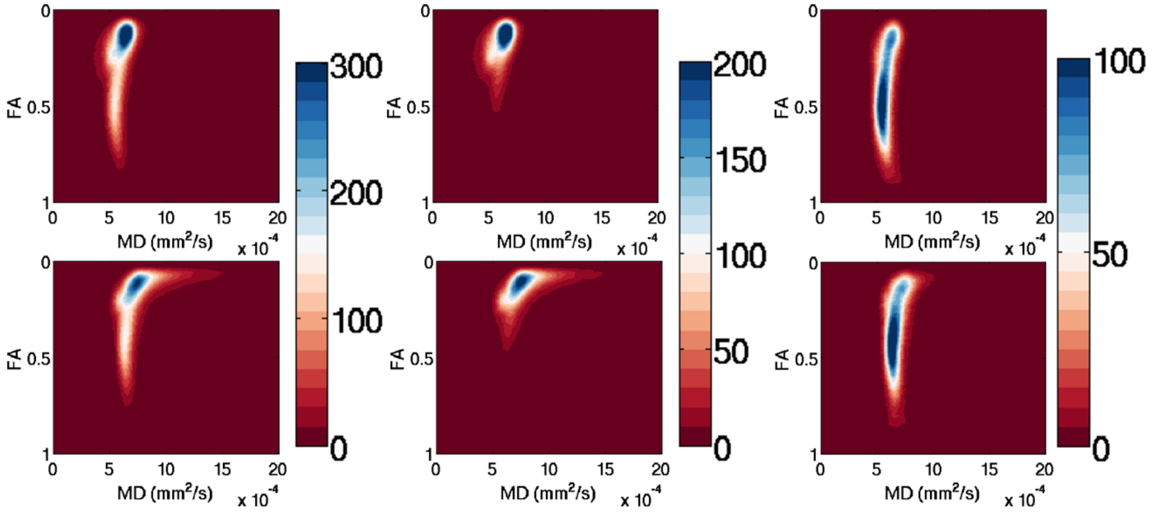

Figure 3.8: Joint FA and MD histograms for FWE (top row) and DTI (bottom row). Maps are shown for the whole brain (left column), GM (middle column), and WM (right column). Partial volumed voxels can be seen as high MD (>0.9 x10^{-3} mm^2/s), low FA (< 0.2) "tail" in the DTI histograms which is not present in the FWE histograms.

		DTI	FWE
WM			
	FA	0.35 ± 0.19	0.41 ± 0.21
	MD (x10^{-4})	6.84 ± 2.47	5.63 ± 1.77
	f	~	0.17 ± 0.14
GM			
	FA	0.15 ± 0.13	0.19 ± 0.16
	MD (x10^{-4})	7.35 ± 4.18	5.28 ± 2.82
	f	~	0.24 ± 0.23

Table 3.4: Global metrics in WM and GM from a single healthy volunteer.

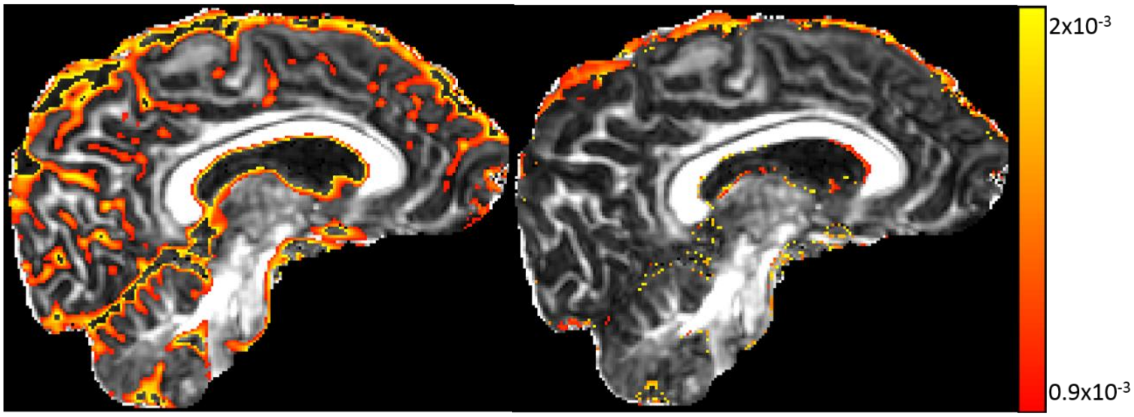

Figure 3.9: Spatial distribution of partial volumed voxels with DTI and FWE. The background is an FA map from a healthy volunteer approximately 7 mm from the mid-sagittal plain. The red/yellow voxels are those with a mean diffusivity between 0.9 $\times10^{-3}$ and 2 $\times10^{-3}$ mm^2/s. The left overlay is from the DTI MD map, while the right overlay is from the FWE tissue MD. These values are intermediate between WM (0.8 $\times10^{-3}$ mm^2/s) and CSF (3$\times10^{-3}$ mm2/s) and clearly outline the interface between the CSF filled ventricles and the corpus callosum and fornix.

The results of the BIC model comparison are displayed in Figure 3.10. This is the same axial slice that was used in Figure 3.7. Greater than 97% of all voxels were better fit by the FWE model for the entire brain volume. There was no obvious spatial distribution of the voxels that were best fit by DTI. However, those fit best by DTI were limited almost exclusively to those voxels that fit a zero value free water fraction. Nearly all voxels that fit some free water component were better fit using the FWE model.

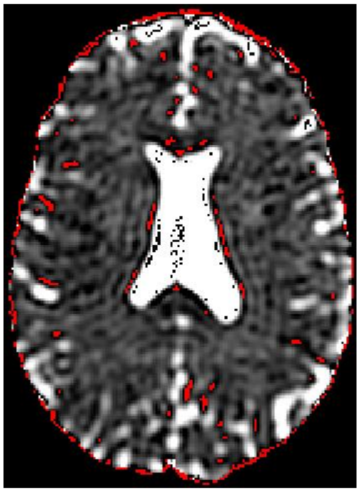

Figure 3.10: Model comparison with BIC. The same axial slice as in Figure 3.7 showing the free water fraction map with an overlay of the DTI preferred voxels from BIC. The voxels in red are those for which the signal is better represented by traditional DTI.

The use of the wrong model, either the standard DTI model when partial voluming is present or the proposed FWE model with no partial voluming, introduces some bias in the FA estimates. Taking a prolate tensor (FA = 0.712) as an example, if a voxel contains a free water fraction of 0.2, then the FA would be underestimated by ≈ .1 (see Table 3.5). As the free water component increases, so would the amount of underestimation. If there is no fast diffusion component (e.g. $f = 0$), then the FWE model should yield the same results as DTI. However, in the presence of noise, the model appears to fit a small fast diffusing component to the noise, thus introducing some small bias. For the prolate tensor with $f = 0$, the FWE model overestimates FA by < 0.009 (see Table 3.6). While induced bias is suboptimal, it is to a much smaller degree than DTI's partial volume errors.

Tables 3.5 and 3.6 display the results of the mismatch between the assumed model and the underlying simulated model. Table 3.5 presents the underestimation that occurs when using a single tensor DTI fit when there is actually a fast diffusing component of 20% (e.g. $f = 0.2$). The resulting FA is biased to a lower than true value even in the case of infinite SNR.

Table 3.5 shows the bias induced by using the FWE model when the underlying signal conforms to the single tensor DTI model ($f = 0$). The model wrongly fits a small fast diffusing component resulting in an overestimate of FA. This is due to a fitting of the noise. As would be expected, the bias decreases as SNR increases.

FA Bias for a Single Tensor Fit

SNR	20	30	40	50	60
Bias	-0.106	-0.102	-0.100	-0.100	-0.099

Table 3.5: FA bias due to using DTI in the presence of partial volume effects. Using a standard DTI model in the case of a volume fraction of 0.2 results in a bias in fitting FA. In this case the standard DTI fit underestimates the true tissue FA which was 0.712.

FA Bias for an FWE Fit

SNR	20	30	40	50	60
Bias	$8.7\text{x}10^{-3}$	$6.3\text{x}10^{-3}$	$4.8\text{x}10^{-3}$	$3.6\text{x}10^{-3}$	$2.3\text{x}10^{-3}$

Table 3.6: FA bias due to using the FWE model when the signal is truly from a single tensor. Using a FWE model in the case of a volume fraction of 0 results in a bias in fitting FA. In this case, the FWE fit overestimates the true tissue FA.

3.5 Discussion

In this study, we introduced a simple technique using a two-compartment diffusion model and two-shell DTI acquisition, which resolves partial volume effects due to CSF contamination. We optimized the acquisition parameters to minimize the estimation errors in FWE DTI. Simulations showed that a two-shell design was superior to designs with a greater number of shells.

Fitting diffusion data to a biexponential function is a notoriously difficult and ill-conditioned problem [53]. It is essential to stress the importance of the “ancillary” points regarding the ways that reinitialization in the search was carried out, as well as the modified Newton’s method and the setting of the dampening parameter. These finer points resulted in a reduction in MSE of more than an order of magnitude over the case without reinitialization and using a basic Levenberg-Marquardt implementation (not shown). Without the modifications presented here, the model is somewhat prone to poor performance especially with a large f-value.

The estimation of tensors with a substantially high f-value leads to overestimated FA values. The lower the anisotropy, the more pronounced the effect was. This matches the observation from DTI in the presence of low SNR [52]. The low anisotropy scenario means that the proposed method contains extra parameters that are unnecessary, hence the estimation of these parameters may vary wildly. For this situation the Hessian matrix may not be well conditioned. Without some modification, periventricular grey matter will be most plagued by this error and, thus, the FA in this region cannot by reliably determined. However, for high FA regions such as coherent white matter it is expected that a higher f-value (≈ 0.8) may be tolerated with reliable performance. This stands as a clear limitation of the presented method. Though spatial regularization was intentionally avoided, it may be that some spatial constraints would reduce this limitation. Nothing regarding the current implementation would preclude the inclusion of spatial constraints. It is also possible to mitigate most errors by dismissing all diffusion metrics from voxels with an f-value set above a reasonable threshold such as 0.75.

Any voxel that contains some free water portion must necessarily have a lower signal arising from the tissue compartment. As such, the FWE tensor SNR will be lower than when fitting a single diffusion tensor to the recorded signal. This effect, in turn, emphasizes the known directional dependence of variance in diffusion imaging [48,54]. We believe it is this reduced tissue compartment SNR which causes the uncertainty and bias when the isotropic component is large. It is expected that any method that attempts to resolve CSF PVE in a voxel will similarly be plagued by low apparent SNR. This would be expected even in experiments that fit a single diffusion tensor but alter the acquisition to minimize the CSF signal such as fluid attenuation inversion recovery [55] and the recent method suggested by Baron and Beaulieu [56].

The difference in estimation accuracy for two-shell acquisition design, as compared to any of the other designs, was statistically significant with $p < 0.05$ via t-test. Even so, thanks to the algorithm optimization, any of the acquisitions with the "optimal" *b*-values would likely perform sufficiently well *in vivo*. Due to its performance and relative simplicity, the two-shell acquisition is recommended for future work.

The FWE DTI model is based on the assumption that the fast diffusion compartment behaves as free water in both magnitude ($D = 3 \times 10^{-3}$mm^2/sec) and mode (isotropic) of diffusion. This is a reasonable approximation in regions with CSF and is the basis for the previous studies that apply FWE DTI [43,44,57,58]. Note that, if the fast diffusion component deviates significantly from the predicted value, the acquisition parameters may be suboptimal and the estimated measures from the model may be biased. However, our early *in vivo* results when allowing the isotropic D to vary from 2 x10^{-3}mm^2/sec to 4 x10^{-3}mm^2/sec in increments of 2 x10^{-4}mm^2/sec show that D = 3 x10^{-3}mm^2/sec fits best for more than 93% of voxels. This suggests that, for the FWE model, 3 x10^{-3}mm^2/sec is appropriate for isotropic compartment diffusivity.

The *in vivo* results with the optimized scan parameters in this study yielded a mean FWE volume fraction of 0.17 ± 0.14 in white matter and 0.24 ± 0.23 in grey matter, which are consistent with previously reported values using FWE DTI [44]. These volume fractions are similar to the mean extracellular volume of ≈ .2 in brain parenchyma from non-MRI diffusion measurements of tetra-methylammonium (TMA) [59]. Though these results are similar, the physical interpretation of the isotropic component within the parenchyma away from CSF interfaces may be debated as being inconsistent with the expected properties of the extracellular space (Beaulieu, 2002 and references therein).

Consequently, the FWE isotropic volume fraction is unlikely to be an exact measure of the extracellular volume. For diffusion times associated with clinical DTI pulse sequences, much of the water in the extracellular space will encounter barriers and display anisotropic diffusion. Note that in previously reported bi-exponential diffusion experiments with two unconstrained tensors [61-65] there was no obvious correlation to intra- and extracellular compartmentalization with the $D_{fast} \approx 1.2 \times 10^{-3}$ mm^2/s for the human brain. Using a compartment specific tracer, Duong et al. suggest that the difference in diffusivity between intra- and extracellular compartments may be indistinguishable [66].

Further complicating the interpretation of the isotropic component as being indicative of the extracellular compartment is the presence of Gibbs ringing in the f map, Figure 3.7h. This artifact is also present in the $b = 0$ image due to the high contrast transition from CSF to parenchyma. The high spatial frequency of the edge at CSF and brain borders causes the ringing. This artifact is then propagated in the tensor calculation and is visible in the standard MD image, Figure 3.7e. By using the FWE model, this ringing appears substantially reduced from the tissue compartment MD maps, Figure 3.7f. This artifact reduction should allow the tensor to more faithfully reflect diffusion properties of the tissue, however, it also displays that the f-value may be affected by factors beyond the extracellular volume.

Even with the many complications in interpreting the free water component in the parenchyma, it is our belief that it is a surrogate measure of extracellular space. Only within the extracellular space could a water molecule have the requisite room to diffuse as free water. Certainly not all water within this space would behave as free water, but some might. Furthermore, any pathology which may affect the dimensions of the extracellular space ought to have an effect on the free water fraction.

Cursory investigations were performed into whether simple, crossing white matter fibers could lead to a fast diffusion component in the FWE model with the conclusion that relatively simple two tensor patterns do not induce fitting a larger f than the bias amount of < 0.01. The requirement that diffusion be both fast and isotropic prevents spurious fitting in the case of two crossing tensors composed of a simple combination of the tensors simulated.

The FWE model estimates for reported bi-exponential diffusion [64,65] were also investigated and yielded a small free water fraction (≈ 0.11) that was consistent with the values observed in some of the white matter. So, this is also a potential mechanism for parenchymal apparent fast diffusion. We note that these estimates are consequently misleading, though no less so than standard DTI, which also does not adequately treat the bi-exponential diffusion. For this simulation the full tensors reported for diffusion in the rat brain by Inglis et al. [64] were modified to match the volume fractions and mean apparent diffusivities reported by Maier et al. [65] in the human brain.

Even with the limitations noted, the free water elimination model may be implemented in a simple way with a scan that is less than six and a half minutes. With a manageable scan time and additional information relative to DTI, we believe that the FWE scheme has significant potential for immediate, impactful clinical use. While more sophisticated models such as

CHARMED, DBSI, and NODDI provide attractive models, they are not currently configured for routine clinical use [16,17,47].

The joint histograms of WM and GM, Figure 3.6, show a great reduction in partial-volume averaged voxels with MD > 0.9×10^{-3} mm^2/s and FA < 0.2. Instead, these voxels are corrected to be more in line with the majority of voxels in the parenchyma. It appears that partial volume effects with CSF have been corrected successfully, resulting in tissue specific diffusion measures.

As a means of correcting for partial volume effects, the free water elimination model has the potential for a wide variety of applications. Any investigation into diffusion properties of tissue bordering CSF could benefit from adopting the FWE model. For example, this method may provide a means to differentiate widespread edema from infiltrating tumor by revealing tissue characteristics masked by the presence of edema. Additionally, due to its proximity to CSF, cortical grey matter diffusion imaging would greatly benefit from this model as well. Further validation is required to truly interpret the isotropic volume fraction.

3.6 Conclusions

In this paper, a bi-tensor free water elimination model that is useful for the removal of the confounding effects of free water and other sources of fast diffusion in the brain was described. These effects appear at CSF interfaces due to partial volume effects and more distally due to Gibbs ringing artifacts. The result is DTI measures that are better representations of underlying tissue microstructure and the additional contrast mechanism of the free water map. This work offers a straightforward implementation of the FWE model along with recommended acquisition parameters. The FWE model allows for a clinically acceptable acquisition time and reconstruction. For the conditions investigated, the best acquisition featured two *b*-value shells with an equal distribution of directions per shell. The recommended *b*-values are 500 and 1500 s/mm^2 for each shell. Future work will include applications to investigate performance in cortical gray matter, white matter adjacent to the ventricles, and the differentiation of infiltrating tumor from bland edema.

Chapter 4

Model Validation in White Matter with Deterministic Tractography

Portions of this chapter have been submitted to the *Journal of Magnetic Resonance Imaging* as a manuscript titled, Free Water Elimination Diffusion Tractography: A Comparison with Conventional and FLAIR DTI Acquisitions.

4.1 Abstract

Diffusion tensor imaging (DTI) coupled with tractography is an excellent technique to reconstruct white matter pathways and extract diffusion metrics. In the case of partial volume effects with cerebrospinal fluid, standard DTI fails and an alternative acquisition such as fluid attenuation inversion recovery (FLAIR) DTI is required. Here we show that the free water elimination (FWE) diffusion model can also overcome CSF PVE without the time, signal to noise ratio, and volumetric coverage penalties inherent to a FLAIR acquisition. Reconstruction of the fornix shows that the FWE scan provides larger ($p < 0.0005$), anatomically appropriate tracts than either DTI or DTI FLAIR acquisitions.

4.2 Introduction

Diffusion Tensor Imaging (DTI) is currently the most widely used neuroimaging MRI technique for characterizing tissue microstructure [67]. DTI coupled with tractography algorithms are also used to reconstruct specific white matter (WM) tracts, which may be used to define volumes of interest (VOIs) for comparison of region-specific diffusion metrics across subjects [68]. The use of tractography to define VOIs reduces the user dependence, required time, and difficulty inherent to manual segmentation of successive two-dimensional image slices [55].

Diffusion weighted imaging has inherently low signal to noise ratio (SNR) due to both diffusion effects and increased echo times (TE) from the large diffusion-encoding gradient pulses required for diffusion weighting. Although the use of multi-channel array head coils may help to improve SNR, DTI is commonly acquired with spatial resolution between 2mm and 3mm in each dimension in order to maintain adequate SNR levels. Increased spatial resolution requires longer scan times that may adversely affect clinical feasibility and increase the likelihood of head motion. Large voxel sizes also lead to greater partial volume effects, especially in white matter tracts such as the fornix and the corpus callosum, which share borders with cerebrospinal fluid. Diffusion properties of both of these tracts have been extensively studied in a wide variety of applications including normal aging, mild cognitive impairment, Alzheimer's disease, traumatic brain injury, and autism [36,58,69–72].

When two tissues with differing diffusion characteristics share a voxel, the classical DTI model no longer applies. For example, the classical DTI model underestimates the fractional anisotropy and overestimates the mean diffusivity in voxels with mixtures of CSF and either WM or gray matter (GM). White matter tractography algorithms often utilize an FA threshold (e.g., FA > 0.1 to 0.3) to terminate the tract reconstruction. Consequently, tractography of WM proximal to CSF can prematurely terminate, which may lead to misinterpretation of that tract.

One approach to reduce PVE in DTI is the use of a fluid attenuation inversion recovery preparation pulse before the acquisition of each slice. When properly timed, the FLAIR preparation reduces the signal from CSF to nearly zero, effectively eliminating PVE [55,73]. However, this approach carries with it several limitations. First, the WM signal, and hence, SNR is reduced approximately 25% when the inversion time (TI) is chosen to null CSF. Secondly, the relatively long inversion time for CSF suppression (2000 ms) drastically increases the repetition time (TR), and hence, overall scan time. Lastly, multi-slice interleaving strategies become increasingly difficult when incorporated with preparation pulses, and multi-slice acquisitions are often limited by the maximum number of slices achievable for a given inversion time.

Alternatively, a multi-component model may be used to account for PVE of CSF and brain tissue [43,44,57,74,75]. In the last chapter, the FWE DTI model was introduced and optimized. This method requires only a minor change to acquisition protocol and does not require spatial constraints or assumptions it was previously proposed and optimized [76]. This work compares the robustness of deterministic tractography in regions with CSF contamination for traditional DTI, FLAIR DTI, and the FWE DTI method outlined in Chapter 3.

4.3 Methods

In the FWE model, CSF is assumed to be isotropic and have a known ADC. The use of two non-zero b-values greatly simplifies the parameter space allowing accurate and stable DTI measures even without spatial constraints and assumptions. The FWE DTI signal model [42] is described by

$$S_i = S_0[(1-f)\exp(-b_i g_i^T D g_i) + f exp(-bD_{iso})] \tag{4.1}$$

where S_i and S_0 are the signal from the i-th diffusion and non-diffusion weighted measurements, respectively, D_{iso} = 3 x10^{-3}mm^2/sec is the free water diffusivity, $\boldsymbol{D}$ is the tissue diffusion tensor, b_i and g_i are the diffusion-weighting amplitude (in mm^2/s) and unit gradient encoding vector, respectively.

Ten healthy young (mean age: 25.6 yrs., range: 22-29 yrs.) volunteers underwent four separate DTI acquisitions constituting three distinct comparisons. All scanning was performed using informed consent and was in compliance with an approved protocol from the Institutional Review Board. Brain imaging studies were performed using a 3-Tesla MR750 Discovery scanner (General Electric Healthcare, Waukesha, WI) and a 32-channel, receive-only brain coil (Nova Medical). Diffusion tensor imaging measurements were obtained using four DTI scans: (1) standard DTI, (2) FLAIR DTI, (3) short FWE DTI and (4) long FWE DTI. Unique protocol parameters for each case are listed in Table 4.1.

	FLAIR DTI	Standard DTI	FWE (long)	FWE (short)
Acquisition time	9:00	9:00	9:00	5:24
TR (ms)	10000	6000	6000	6000
TE (ms)	63.1	63.1	68.9	68.9
Number of images x b-value	6 x 0 48 x 1000	10 x 0 80 x 1000	10 x 0 40 x 500 40 x 1500	6 x 0 24 x 500 24 x 1500

Number of slices	34	64	60	60

Table 4.1: Relevant scan parameters for the four acquisitions to be compared.

In all cases, DTI was performed using a diffusion-weighted spin-echo EPI pulse sequence with a single refocusing pulse, parallel imaging with ASSET (R=2) and custom modifications to enable FLAIR and arbitrary encoding directions. Images were acquired using contiguous sagittal slices with 2.5 mm isotropic resolution (96x96 matrix over a 240 mm FOV). A higher order shim preceded the first DTI scan. In all cases, the TR was set to the minimum value to optimize the acquisition efficiency. All DTI cases except FLAIR had a matching slice prescription. The inversion time for the FLAIR scan was set to 2000 ms. The maximum number of slices for FLAIR DTI was limited to 34, so coverage was limited to the mid-brain region, which included all of the tracts of interest. For both standard DTI and FLAIR DTI, diffusion-weighted images were collected at a single b-value (1,000 s/mm^2). The number of encoding directions was increased for standard DTI to match the scan time of FLAIR DTI. For both FWE DTI scans, diffusion-weighted data were collected at two b-values (500 and 1,500 s/mm^2), which is necessary for fitting the two-pool FWE model [46]. For all DTI scans, the ratio of diffusion weighted images to b_0 images was maintained at the reported optimal value of 8:1 [5]. The short FWE DTI protocol matched the number of diffusion encoding directions used in the FLAIR DTI studies. The long FWE DTI protocol increased the number of diffusion encoding directions to match the overall acquisition time for standard DTI and FLAIR DTI and the number of encoding directions for standard DTI. The diffusion encoding directions were matched for the pair of standard DTI and long FWE DTI scans, and the pair of FLAIR DTI and short FWE DTI scans.

The first experiment compared standard DTI, FLAIR DTI, and long FWE DTI acquisitions with the same scan time and resolution. The second comparison was between FLAIR DTI and short FWE DTI scans with the same number of encoding directions. Lastly, the long and short FWE scans were compared to judge the effect of acquiring a different number of diffusion-weighted images.

The traditional and FLAIR DTI scans were single shell acquisitions that were reconstructed per our standard laboratory pipeline that included a combination of FSL, Camino and custom Matlab tools. The preprocessing steps included movement and eddy current correction, gradient direction correction, brain extraction, and a single tensor fit with Camino [77,78]. Eddy current correction and brain extraction were carried out using the FSL toolkit [79]. For the FWE scans, the process was the same except that the FWE DTI model in Equation 4.1 was fit in Matlab [76] and the resulting free water component removed prior to performing tractography with Camino. As the FWE model treats the signal from each voxel as a combination of a single tensor and a free water signal, the removal of the free water signal provides a better probe of the underlying tissue diffusion tensor. Up to this point, all processing had been performed in the individual space for each scan.

In order to define the VOIs to be used for tractography, a template image was constructed for each individual subject using DTI-TK, which performs DTI spatial normalization using the full tensor for alignment [80]. For each individual subject, the number of slices from each scan was reduced to match that of the FLAIR scan and create the subject-specific template. The FA map from the template was used to define the tractography VOIs, which were inverse warped into the native space for each scan [81].

Whole-brain tractography was performed using the fiber assignment by continuous tracking (FACT) algorithm [19] as implemented in the Camino software package. Tracts were seeded at the center of every voxel with an FA greater than or equal to 0.3. Specific tracts were then reconstructed by constraining viable fibers through the use of targeted inclusion and exclusion VOIs. An FA threshold of 0.3 and a curvature threshold of 60 degrees over 5 mm were used as stopping criteria. Visualization was carried out using TrackVis [82].

The primary metric for comparison was tract volume. Within the confines of being consistent with known anatomy, a larger reconstruction volume is likely indicative of fewer prematurely terminated tracts [55,83,84]. Tract volume was determined by multiplying the voxel volume (15.625 mm^3) by the number of voxels that contain any portion of a tract. The FA and MD along the tracts were also compared, however, these metrics cannot be used to determine reconstruction quality. Statistical significance was determined using a paired student's t-test with $\alpha = 0.05$ and Bonferonni correction for multiple comparisons.

Native-space tractography reconstructions were performed for the corpus callosum (CC), fornix, and cingulum. The first two tracts were chosen because of their proximity to CSF filled spaces such as the ventricles and interhemispheric fissure. The cingulum bundles are not adjacent to CSF spaces and, thus, were control tracts. A single VOI defined on the midsagittal FA image was used to define the corpus callosum, Figure 4.1. This was further subdivided into five regions using the scheme proposed by Hofer and Frahm, based on fiber projection regions [85]. These regions were prefrontal (CC-I), premotor and supplementary motor

(CC-II), primary motor (CC-III), primary sensory (CC-IV), and parietal, temporal, and visual (CC-V). The fornix was delineated based on intersection with two primary VOIs in the columns and body of the fornix and one of two secondary VOIs in the left and right crux [86], Figure 4.2. The right and left cingulum bundles were defined by tracts that pass through a pair of VOIs – anterior above the corpus callosum genu and posterior above the corpus callosum splenium – placed on the thin green white matter tracts immediately superior to the corpus callosum [18,87], Figure 4.2.

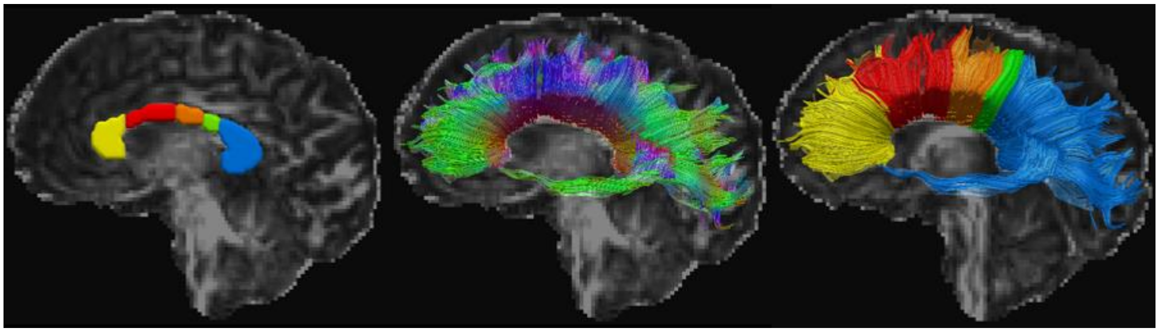

Figure 4.1: Seed VOI and example segmentation of the corpus callosum overlaid on an FA map. The CC was segmented into the following five regions: CC-I (yellow), CC-II (red), CC-III (orange), CC-IV (green), and CC-V (blue). The middle image shows a streamline reconstruction of the CC with DEC encoding based on the primary eigenvector. The rightmost image shows the same reconstruction with color determined by the seed VOI from which the tract originated.

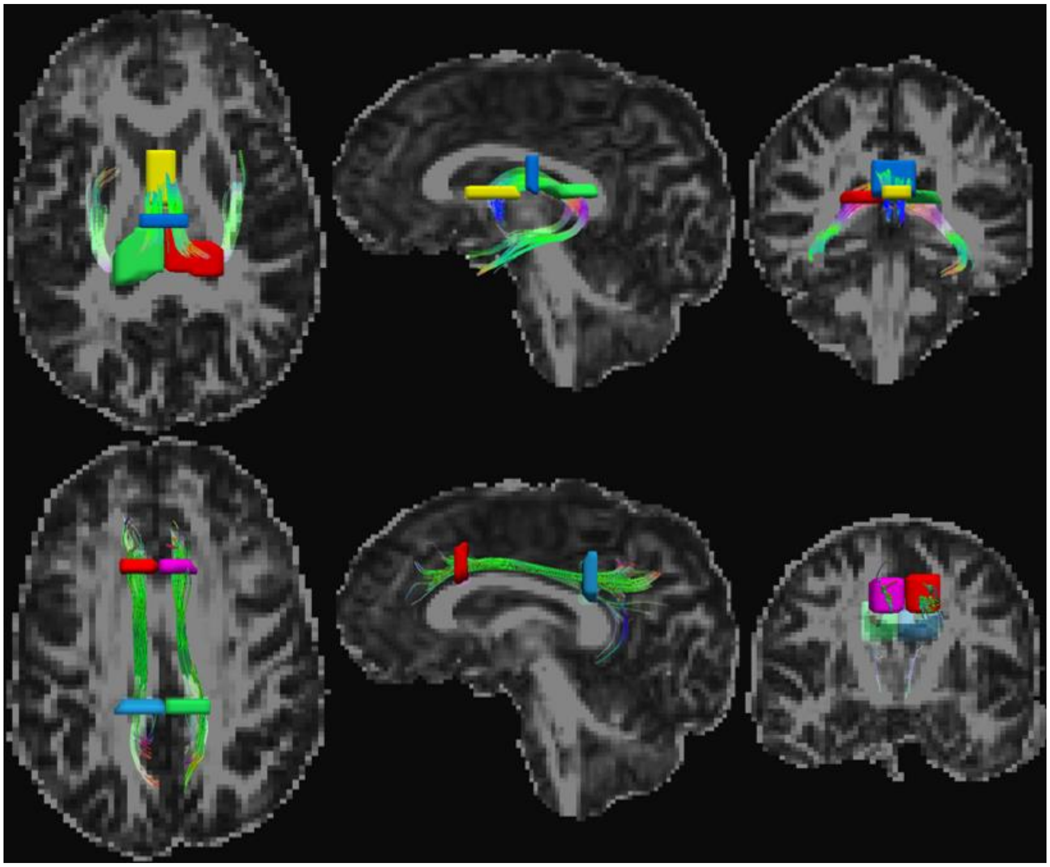

Figure 4.2: Example of the VOIs used to define the fornix (top row) and cingulum (bottom row). Fornix tracts were reconstructed if they passed through the columns (yellow), body (blue) and either the right crux (red) or left crux (green). Cingulum tracts were reconstructed if they passed through an anterior VOI (left: red, right: pink) and a posterior VOI (left: blue, right: green).

4.4 Results

The SNR of the b = 0 images for the standard DTI scan in white matter was 47 ± 1.2. Both the FLAIR DTI and FWE DTI scans displayed a reduction in SNR with measured values of 32 ± 0.8 and 42 ± 2.2, respectively, corresponding to an SNR reduction of 33% and 11%, respectively, when compared to the standard DTI. As is expected, there is no discernable difference in SNR between the long and short FWE scans.

Figure 4.3 shows the reconstructed volume for each of the four acquisitions and seven tracts relative to the standard DTI. The FLAIR DTI sequence yields a significantly larger reconstruction than standard DTI in CC-I, CC-III, CC-V, and the fornix. Likewise, the long FWE DTI sequence was statistically larger for all reconstructed tracts. Meanwhile, the tract reconstructions from the short FWE DTI scan was larger for all CC tracts and the fornix, but not the cingulum.

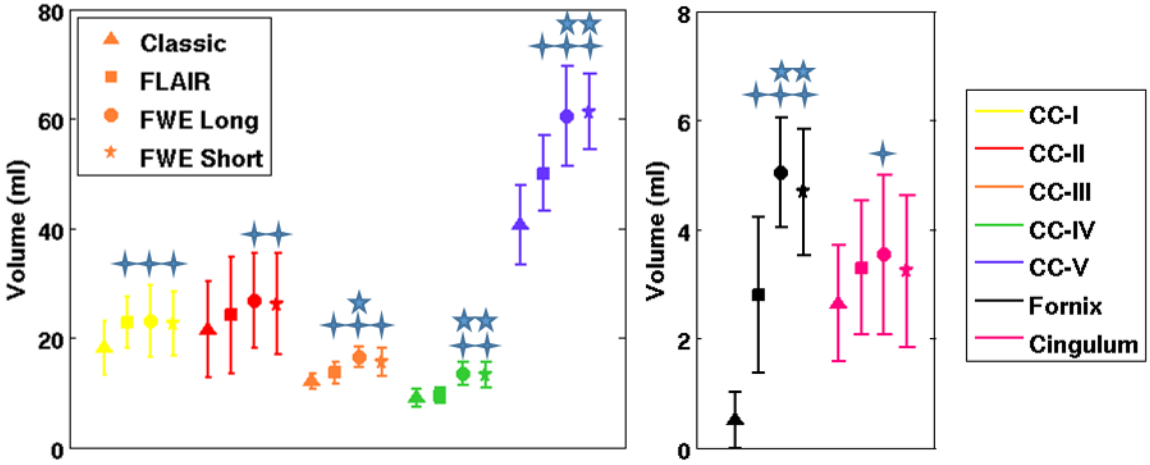

Figure 4.3: Reconstructed volume for seven tracts and four acquisitions. The marker shape denotes acquisition type and the color gives the reconstructed tract. A four sided star (✦) represents a significant difference from ‘traditional’ DTI and a five sided star (★) is a significant difference from FLAIR.

For some tracts the differences between the FLAIR DTI reconstruction and the FWE DTI reconstructions were also significantly different. The long FWE DTI scan produced a larger reconstruction for CC-III, CC-IV, CC-V, and the fornix. For the short FWE DTI scan, CC-IV, CC-V, and the fornix resulted in statistically larger tract reconstructions. The two FWE DTI scans showed no significant differences for any of the tracts reconstructed.

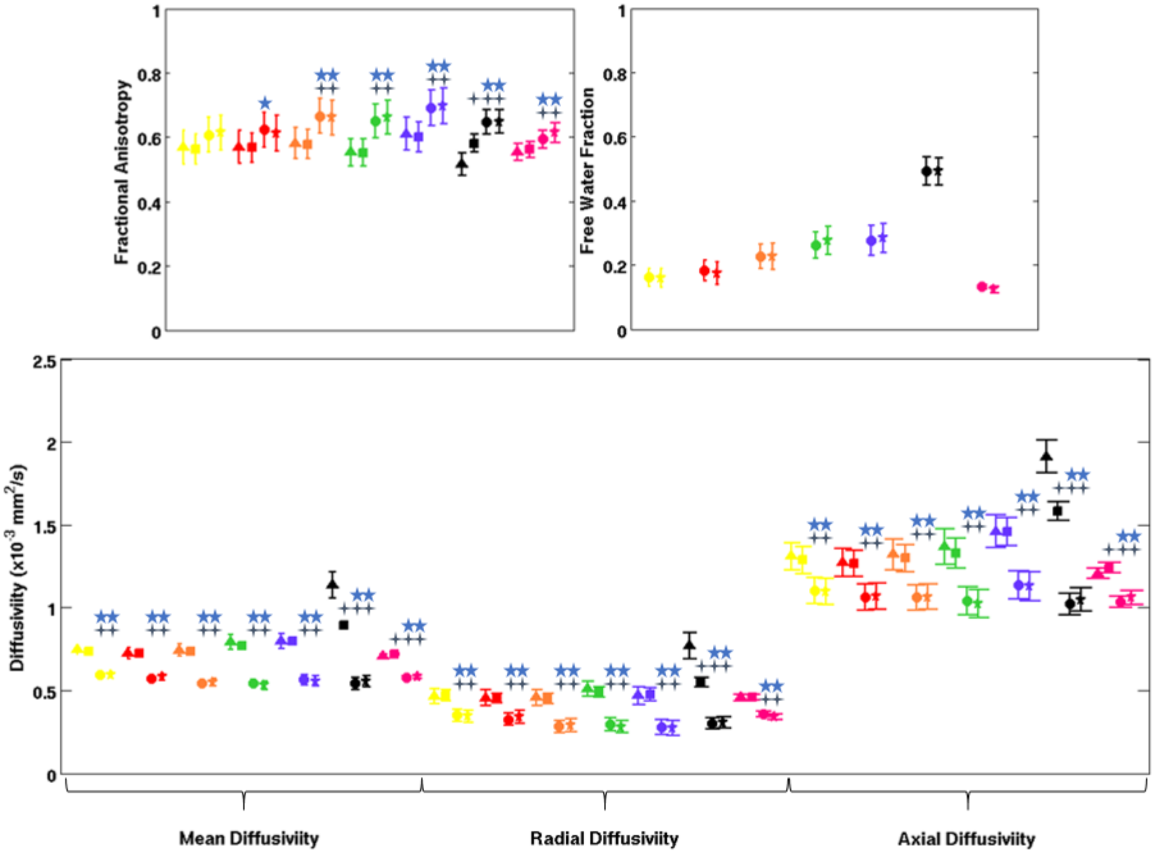

Figure 4.4: Diffusion metrics for each of the tracts and acquisitions. The marker and color definitions are the same as in Figure 4.3.

The study also investigated DTI method differences in the diffusion metrics, Figure 4.4. FLAIR DTI and standard DTI resulted in substantially similar diffusion metrics in the entirety of the corpus callosum. However, differences were noted in the fornix and cingulum bundles. In the fornix, FLAIR DTI yielded significantly smaller mean, radial, and axial diffusivities along with a higher FA. In the cingulum, FLAIR DTI yielded larger mean and axial diffusivities as compared to standard DTI. Meanwhile, the FWE DTI methods were very similar to each other, but significantly different from both standard DTI and FLAIR DTI scans in terms of mean, radial, and axial diffusivities for every reconstructed tract. Significant differences in FA were seen between both FWE DTI scans and standard DTI for all tracts except for CC-I and CC-II. As the fornix displayed the most dramatic metric changes and the highest degree of PVE, as measured by mean *f*-value, Figures 4.5 and 4.6 show these reconstructions from one subject in more detail. These Figures show the reconstructed tracts from each method along with the spatial distribution of FA and MD along the tracts.

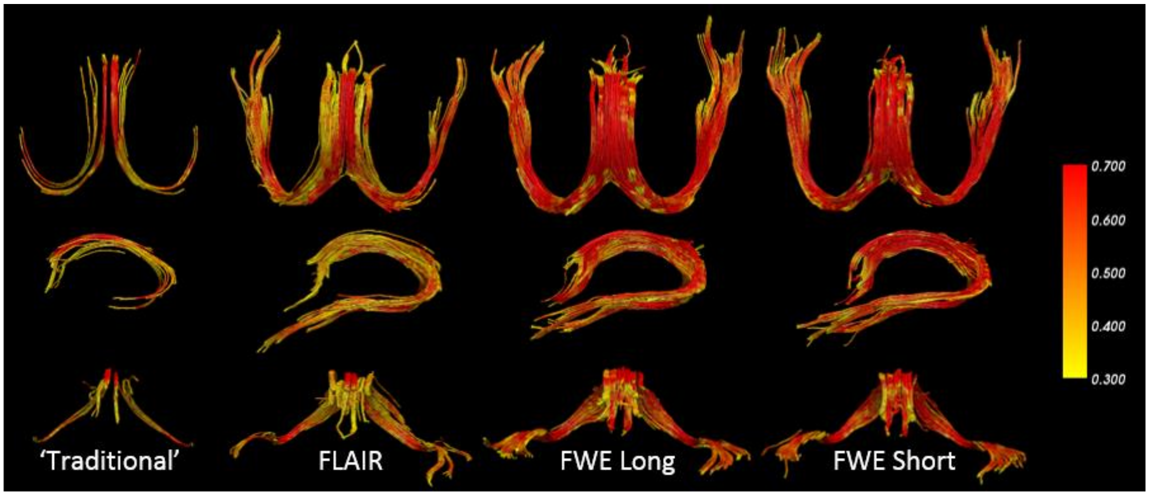

Figure 4.5: Streamline reconstruction of the fornix from one subject. The color coding is based on the FA of the tract. The reconstruction is presented in axial (top row), sagittal (middle), and coronal (bottom) views.

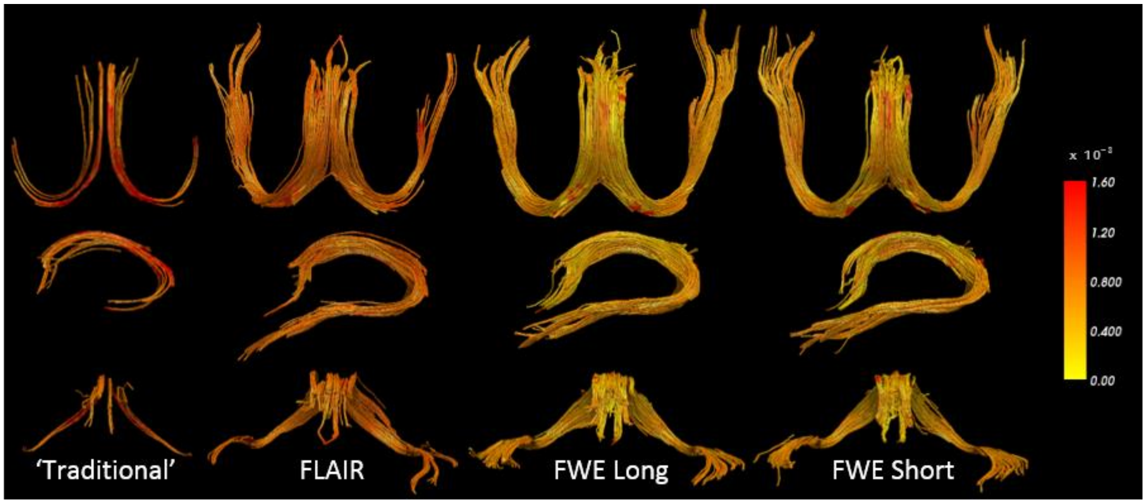

Figure 4.6: Streamline reconstruction of the fornix from the same subject as in Figure 4.5. The color coding is based on the MD of the tract. The reconstruction is presented in axial (top row), sagittal (middle), and coronal (bottom) views.

The spatial distribution of f-value can be visualized along each tract in Figure 4.7. For both the fornix and CC, the *f*-value shows a pattern consistent with PVE from the ventricles. The superior portion of the fornix and the inferior portion of the CC that border the ventricles do indeed have the largest *f*-value. In the CC the *f*-value was seen to increase from anterior to posterior for the corpus callosum, Figures 4.4 and 4.7. Clearly this is skewed by the relative amount of PVE for each tract with the ventricles and for CC tracts which penetrate into the cortex, which is more highly partial volumed with CSF. When removing the highly partial volumed voxels ($f > 0.5$), the resulting mean *f*-value is found in Table 4.2. With the exception of CC-V to CC-IV, each tract has a significantly larger *f*-value than the one immediately anterior to it. The cingulum bundles show the lowest mean *f*-value and little spatial variation along the tracts, Figures 4.4 and 4.7.

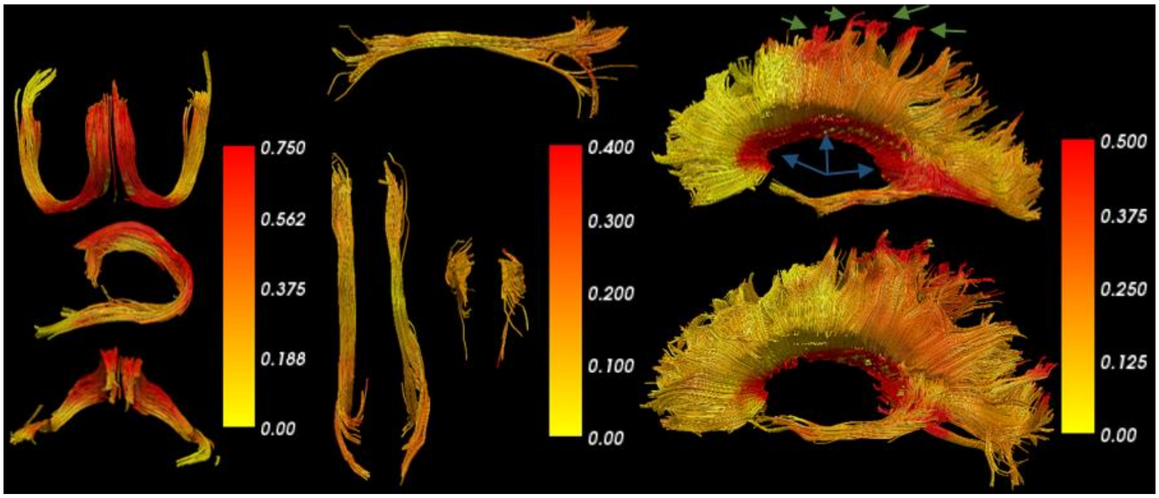

Figure 4.7: *f*-value projected onto the reconstruction of the fornix (left), cingulum (center), and corpus callosum (right). The fornix displayed the greatest degree of PVE as it is located inferior and proximal to the CSF filled ventricles. Corpus callosum reconstructions from two separate subjects are shown. The blue arrows show the area of PVE with the ventricles. Green arrows show tracts that propagate through the cortex where PVE are common due to the folded nature of the cortex.

Tract:	CC-I	CC-II	CC-III	CC-IV	CC-V
Without Correction	0.164 ± 0.025	0.197 ± 0.030	0.226 ± 0.034	0.266 ± 0.027	0.278 ± 0.021
With Correction	0.156 ± 0.021	0.183 ± 0.022	0.222 ± 0.036	0.260 ± 0.029	0.264 ± 0.020

Table 4.2: Mean isotropic signal component for CC regions with and without correction for highly partial volumed voxels.

In terms of qualitative appearance, the cingulum bundles showed no noticeable difference between any of the techniques, while the fornix showed distinctly larger, more complete reconstructions with the FLAIR DTI and FWE DTI protocols, Figures 4.5 and 4.6. For the fornix, the standard DTI acquisition yielded smaller, incomplete appearing tracts in all subjects. Differences in the appearance of the CC, though existent, were subtle and not visually obvious for most subjects.

The effect of acquisition and reconstruction on the homogeneity of diffusion measures within a single coherent structure was assessed by analyzing the standard deviation of a given metric along a single tract. The means of the standard deviations along the fornix and cingulum are shown in Table 4.3. Values are provided for FA, MD, RD, and AD. The standard deviations for the diffusivity metrics (MD, RD, AD) in the fornix are reduced with FLAIR DTI and the FWE DTI acquisitions compared to standard DTI. This is not seen in the cingulum, where variability in diffusivity measures for the PVE resolving techniques is comparable or greater than standard

DTI. For both tracts, variability of FA increases from standard DTI to FLAIR DTI and then to the FWE DTI techniques. Though not shown, all of the corpus callosum tracts displayed the same pattern as the fornix, though to a lesser extent.

	Fornix				Cingulum			
	DTI	FLAIR	FWE long	FWE short	DTI	FLAIR	FWE long	FWE short
FA	0.12	0.13	0.17	0.16	0.09	0.11	0.12	0.14
MD	0.26	0.10	0.15	0.15	0.04	0.03	0.04	0.05
RD	0.26	0.13	0.16	0.15	0.07	0.08	0.07	0.08
AD	0.33	0.26	0.29	0.31	0.11	0.15	0.15	0.18

Table 4.3: Mean of the standard deviations of the diffusion metrics along the fornix and cingulum.

4.5 Discussion and Conclusion

This work demonstrates the utility of a simple diffusion model to alleviate deleterious effects of unwanted mixing of CSF and brain tissues, thereby improving tractography. The tracts produced with the proposed FWE DTI were more complete than those produced using traditional DTI. Compared to FLAIR DTI, which also shows tractography advantages compared to DTI, the FWE DTI scan can be performed in almost half the time and with more volumetric coverage. The benefits of FWE DTI were greatest in the fornix due to its close proximity to CSF.

For the tracts with high CSF PVE (fornix and corpus callosum), the FLAIR DTI and FWE DTI scans led to a reduction in standard deviation for the diffusivity measures along a tract with the reduction greatest for FLAIR DTI. In contrast, the cingulum, which is not adjacent to CSF, had increased variability using either FLAIR DTI or FWE DTI methods, which have decreased SNR. The SNR penalty from FLAIR DTI may increase the standard deviation along the tracts. Also, the added complexity of the FWE DTI model in the cingulum may introduce uncertainty by fitting more parameters than are necessary since the expected free water fraction f is zero.

When considering the diffusion metrics associated with each technique, it becomes apparent that the FWE techniques do not simply remove the effects of CSF. If this were the case, the FWE metrics would be more in line with the measures from FLAIR DTI. However, FWE DTI results in a greater FA and reduced diffusivity measures even in tissues without CSF PVE. For example, the cingulum bundles, though not being in direct contact with CSF, have a mean f-value of 0.13 ± 0.03 and 0.12 ± 0.05 for the long and short FWE DTI protocols, respectively. It has been hypothesized that this signal arises from the extracellular space (ECS) [44,57]. The results here suggest that, for this theory to be true, water in the ECS must diffuse freely yet have a T1 that is distinct from CSF and, thus, not nulled by FLAIR.

In addition to removing CSF PVE, the *f*-value may also reflect properties of tissue microstructure and organization. Much like diffusion kurtosis imaging (DKI) [10] quantifies the deviation from monoexponential signal decay, a non-zero *f*-value may be an alternative means of modeling this deviation. Thus, even when analyzing tracts distal from CSF, the presence of a non-zero *f*-value reflects the inadequacy of the DTI model to represent the measured diffusion decay. If indeed the *f*-value in parenchyma reflects kurtosis effects, then the prior constraint [76] on the maximum acquisition b-value of 1500 s/mm^2 is unnecessary.

The CC shows both a quantitative (Table 4.2) and qualitative (Figure 4.7) pattern of increasing *f*-value from anterior to posterior. Studies with light and electron microscopy have noted that the fiber size and density of the CC is regionally dependent [88,89]. These studies note that the highest fiber density and smallest mean axon diameter are in the anterior CC with decreasing density and increasing diameter moving posterior. The lowest density and largest average diameter occur in the posterior mid-body with the fiber density increasing in the most posterior portion. While certainly not conclusive evidence, this observation qualitatively aligns with the postulation that *f*-value corresponds to the ECS.

In conclusion, this work confirms that the FWE DTI method is capable of alleviating the partial volume effects of CSF at the borders of white matter tracts. This is especially evident in the fornix, which has high partial volume averaging with CSF. In this tract FWE DTI produces a larger, fuller reconstruction than using FLAIR DTI. The FWE DTI method provides greater anatomical coverage, time efficiency, and SNR when compared with FLAIR. However, both FWE DTI and FLAIR DTI methods will improve the microstructural characterization of tracts with CSF PVE. It was also confirmed that the *f*-value reflects more than just CSF PVE and, thus, diffusion metrics with FWE DTI are distinct from those with FLAIR and DTI, even in regions distal from CSF interfaces.

Chapter 5

Diffusion Measures in Preclinical Alzheimer's Disease

Portions of this chapter have been included in a manuscript intended for future publication. Portions detailing pathological and clinical background and interpretation have been provided by collaborators.

5.1 Abstract

Background: Brain changes associated with Alzheimer's disease (AD) begin decades before disease diagnosis. While β-amyloid plaques and neurofibrillary tangles are defining features of AD, neuronal loss and synaptic pathology are closely related to the cognitive dysfunction observed in AD. Brain imaging methods that are tuned to assess degeneration of myelinated nerve fibers in the brain (collectively called white matter) include diffusion tensor imaging (DTI) and related techniques, and are expected to shed light on disease-related loss of structural connectivity.

Methods: Participants (N=70, ages 47-76 years) from the Wisconsin Registry for Alzheimer's Prevention study underwent diffusion tensor imaging (DTI) and hybrid diffusion imaging (HYDI) to determine a free-water elimination (FWE) model. The study assessed the extent to which preclinical AD pathology affects brain white matter. Preclinical AD pathology was determined using cerebrospinal fluid (CSF) biomarkers. The sample was enriched for AD risk (*APOE* ε4 and parental history of AD).

Results: Elevated AD pathology as shown on CSF was significantly associated with altered microstructure on DTI and FWE-DTI. Affected regions included frontal, parietal, and especially temporal white matter. The f-value derived from the FWE model appeared to be the most sensitive to the relationship between AD biomarkers measured in CSF and microstructural alterations in white matter.

Conclusions: The findings demonstrate that preclinical AD involves white matter degeneration. These results shed light on the early pathological features of AD, in addition to suggesting that white matter imaging measures may have utility as both tools of early disease detection and outcome measures for clinical trials. More complex models of microstructural diffusion may provide increased sensitivity over standard DTI.

5.2 Introduction

Of the characteristics that define AD, neuronal loss and synaptic pathology—not β-amyloid plaques or neurofibrillary tangles—show the strongest relationship to dementia severity and cognitive deficits in AD Beyond standard volumetric MRI, there are few options for gauging cell loss, and sensitive approaches are needed, especially to measure early changes. Diffusion-weighted magnetic resonance imaging (MRI) is an increasingly used technique that is sensitive to the random self-diffusion of water molecules. In an unstructured medium, diffusion characteristics reflect properties of the fluid such as temperature and viscosity. However, in structured media such as brain tissues, the measured signals are instead modulated by the geometry of the tissue microstructure [60]. Thus, water molecules are used as a noninvasive endogenous tracer to probe tissue microstructure.

Diffusion tensor imaging (DTI) describes the distribution of diffusion displacements using a Gaussian model and has been used extensively to assess tissue microstructure changes in aging, AD and preclinical AD[37,90–115]. Despite the promising sensitivity of DTI, it has known limitations that can impair utility and specific interpretation. To date, very few studies have applied advanced diffusion-weighted imaging methods for characterizing complex microstructural changes in the early stages of AD.

In this study, a free water elimination (FWE) diffusion model was utilized to estimate and remove the signal contributions from cerebrospinal fluid (CSF) and apparent free water components from the estimated diffusion tensor of the tissue. The FWE-DTI model contains an isotropic diffusion (free water) component with a diffusion coefficient that is constrained to be approximately three times larger than is typically encountered in tissue [57] in addition to the standard diffusion tensor. The free water diffusivity ($3x10^{-3}$ mm^2/s) matches the theoretical value of CSF at body temperature [40]. The free water signal fraction, denoted as the *f*-value, corresponds to the water that has minimal interaction with tissue barriers over the diffusion time of the experiment. This model minimizes the CSF contamination of DTI measurements in tissues adjacent to CSF filled spaces such as the ventricles and cerebral cortex [74]. Non-zero *f*-values present in tissues distal from CSF may reflect the relative volume of extracellular spaces in the tissue [44,57,75].

We expected that FWE-DTI would provide improved sensitivity to microstructural alterations that occur early in the development of AD. In addition to shedding light on the early features of AD pathogenesis, focusing on microstructural alterations is important given that plaques and tangles—while central features of AD—may be accompanied by additional features that predict progression to dementia[116-118]. Greater sensitivity in detecting microstructural pathology may help identify individuals at greatest risk for cognitive decline, as well as providing a novel outcome measure for clinical trials.

Thus, this study focused on individuals who may harbor preclinical pathology. Asymptomatic participants were recruited from the Wisconsin Registry for Alzheimer's Prevention (WRAP) study, a cohort that is enriched for AD risk based on parental history of AD and a greater percentage of adults who carry a risk gene for AD, ε4 allele of apolipoprotein E (*APOE* ε4). Participants underwent both HYDI MRI and lumbar puncture for CSF. Biomarkers in CSF were used as a proxy for elevated preclinical AD pathology. We hypothesized that individuals with higher burden of preclinical AD pathology as shown on CSF would show microstructural alterations as measured by FWE-DTI.

5.3 Methods

5.3.1 Participants

Participants were 70 asymptomatic late-middle-aged adults (19 males and 51 females, age: 61.2 ± 6.2 yrs.) from the WRAP study. The WRAP cohort comprises well-characterized and longitudinally followed participants who are either positive or negative for parental history of AD. Positive parental history of AD classification was defined as having one or both parents with autopsy-confirmed or probable AD as outlined by research criteria [119,120], and reviewed by a multidisciplinary diagnostic consensus panel. Detailed medical history and phone interviews were conducted to confirm

AD negative participants. Absence of family history of AD required that the participant's father survive to at least age 70 years and the mother to age 75 years without diagnosis of dementia or cognitive deterioration. *APOE* ε4 genetic testing was performed at the University of Wisconsin-Madison, Waisman Center. *APOE* ε4 extraction and isoform classification have been described previously [121,122]. Of those recruited 52 were identified as having a positive family history (FH+). Additionally, 27 subjects were carriers of *APOE* ε4 (APOE4+).

5.3.2 Cerebrospinal Fluid Collection

CSF was collected with a Sprotte 25-or 24-gauge spinal needle at the L3/4 or L4/5 using gentle extraction into polypropylene syringes. Samples were collected in the morning after a 12h fast. Approximately 22mL of CSF were combined, gently mixed and centrifuged at 2000g for 10 minutes. Supernatants were frozen in 0.5mL aliquots in polypropylene tubes and stored at -80°C. Samples were analyzed for total Tau (tTau), phosphorylated Tau ($pTau_{181}$), soluble amyloid precursor protein alpha and beta (sAPPα and sAPPβ) and β-amyloid-42 (Aβ42) using commercially available enzyme-linked immunosorbent assay (ELISA) methods (INNOTEST assays, Fujiurebio, Ghent Belgium) as described previously in detail [123]. Neurofilament light chain protein (NFL), YKL-40 and monocyte chemoattractant protein-1 (MCP-1) and Chitinase-3-like protein (YKL-40), were analyzed using the sandwich ELISA method with a limit quantification of 125 ng/L. Assays were performed by Board-certified laboratory technicians who were blinded to clinical information and who performed all analyses on one occasion. All samples were analyzed according to protocols approved by the Swedish Board of Accreditation and Conformity Assessment (SWEDAC) using one batch of reagents (intra-assay coefficients of variation <10%). Individual biomarkers as well as biomarker ratios were entered into the statistical analyses as predictor variables.

5.3.3 Magnetic Resonance Imaging

Diffusion-weighted imaging was completed on a 3-Tesla MR750 Discovery scanner (General Electric Healthcare, Waukesha, WI) using an 8-channel receive-only head coil. Separate diffusion scans were acquired for the DTI and FWE-DTI model fits. For the FWE scan, multiple nonzero b-values were acquired [76]: (number of images x b-value s/mm^2): 7 x 0, 6 x 300, 21 x 1200, and 24 x 2700 s/mm^2. For the DTI scan, a single nonzero b-value of 1000 s/mm^2 was acquired. Other pertinent parameters were: TR = 6500 ms, TE = 102 ms, slice orientation: sagittal, slice thickness = 3 mm, and in-plane resolution = 2.5 mm x 2.5 mm.

5.3.4 MRI Processing and Analysis

The FWE DTI signal model [42] is described by

$$S_i = S_0[(1-f)\exp(-b_i g_i^T D g_i) + f exp(-bD_{iso})] \tag{1}$$

where S_i and S_0 are the signal from the i-th diffusion and non-diffusion weighted measurements, respectively, D_{iso} = 3 x10^{-3}mm^2/sec is the isotropic free water diffusivity, D is the tissue diffusion tensor, b_i and g_i are the diffusion-weighting amplitude (in mm^2/s) and unit gradient encoding vector, respectively. In this implementation, the use of two non-zero b-values greatly simplifies the parameter space allowing accurate and stable diffusion measures even without spatial constraints and assumptions.

As separate scans were used for each of the diffusion models, all processing procedures through template construction were carried out in parallel, independent processing streams. The FWE DTI and DTI models were fit in each subject's native space. Subject specific templates were then created using DTI-TK http://www.nitrc.org/projects/dtitk/, as a means to leverage the full tensor information for optimal normalization[80,124,125]. Regions of interest (ROI) were drawn in the template space and subsequently warped back to the native spaces to use as a seed point for deterministic tractography. Native-space tractography reconstructions were performed in brain regions known to be affected by AD, including the corpus callosum (CC), fornix, and cingulum. A single ROI defined on the midsagittal fractional anisotropy (FA) image was used to define the corpus callosum, **Figure 5.1**. This was further subdivided into five regions using the scheme proposed by Hofer and Frahm, based on fiber projection regions [85]. These regions were prefrontal (CC-I), premotor and supplementary motor (CC-II), primary motor (CC-III), primary sensory (CC-IV), and parietal, temporal, and visual (CC-V). The fornix was delineated based on intersection with two primary ROIs in the columns and body of the fornix and one of two secondary ROIs in the left and right crux [86], **Figure 5.2**. The right and left cingulum bundles were defined by tracts that pass through a pair of ROIs – anterior above the corpus callosum genu and posterior above the corpus callosum splenium [18,87], see **Figure 5.2**.

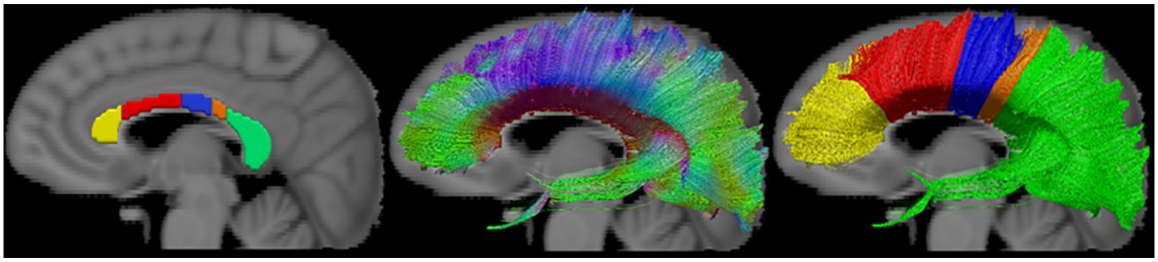

Figure 5.1: Seed ROIs and example segmentation of the corpus callosum overlaid on an MNI T1-weighted template. The CC was segmented into the following five regions: CC-I (yellow), CC-II (red), CC-III (blue), CC-IV (orange), and CC-V (green). The middle image shows a streamline reconstruction of the CC with DEC encoding based on the primary

eigenvector direction. The rightmost image shows the same reconstruction with color determined by the seed ROI from which the tract originated.

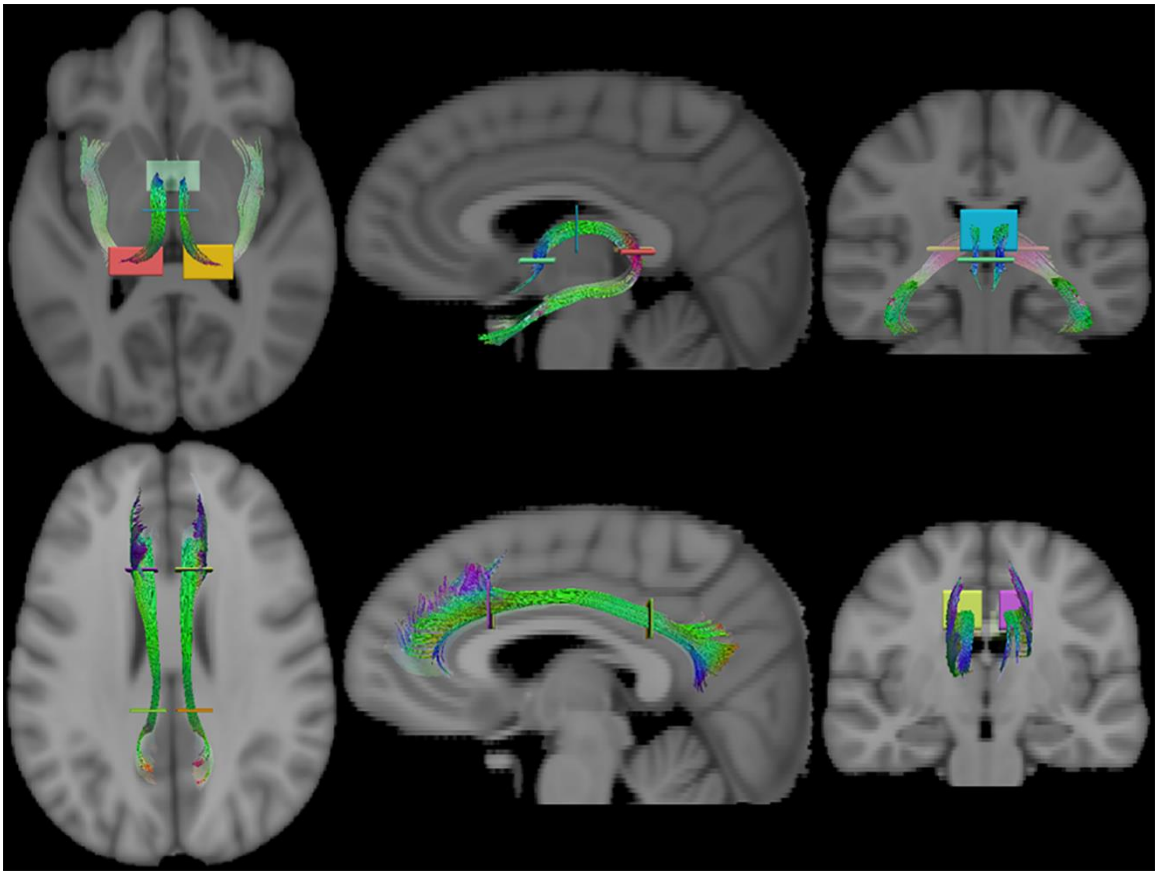

Figure 5.2: The ROIs used to define the fornix (top row) and cingulum (bottom row) in template space. Fornix tracts were reconstructed if they passed through the columns (green), body (blue) and either the right crux (red) or left crux (yellow). Cingulum tracts were reconstructed if they passed through an anterior ROI (left: yellow, right: purple) and a posterior ROI (left: orange, right: green).

The mean value of fractional anisotropy, mean diffusivity, and *f*-value were extracted for each ROI for statistical analysis. Analysis was carried out by fitting a generalized linear model in SPSS 22 (IBM Corp., Armonk, NY), treating the diffusion metrics as dependent variables and the CSF biomarkers and biomarker ratios as predictors, along with age and sex as covariates. In this way, the effect of each biomarker or ratio of markers was analyzed separately on each of the seven tracts and metrics of interest. As a means of controlling for multiple comparisons, a false discovery rate threshold of $p \leq 0.05$ was utilized [126].

Whole-brain tractography was performed using the fiber assignment by continuous tracking (FACT) algorithm [19] as implemented in the Camino software package (http://cmic.cs.ucl.ac.uk/camino/). Tracts were seeded at the center of every voxel with an FA greater than or equal to 0.3. Specific tracts were then reconstructed by constraining viable fibers through the use of targeted inclusion and exclusion ROIs. An FA threshold of 0.3 and a curvature threshold of 60 degrees over 5 mm were used as stopping criteria. Visualization was carried out using TrackVis [82].

The tractography was carried out utilizing the tensor fitting from the FWE scheme. For each individual subject, their DTI scan was aligned to their native FWE scan. In this way, the DTI diffusion metrics could be projected onto the tracts reconstructed using FWE tensors. Using the FWE tensors instead of DTI tensors ensured a more full reconstruction of the fornix. The metrics of interest for FWE were the FA, MD, and *f*-value. All DTI analyses were carried out for FA and MD.

In addition to the tractography analysis, a voxel based analysis (VBA) was performed across white matter constrained by white matter mask. This mask was defined as all voxels for which FA ≥ 0.2. Given its importance in AD and susceptibility to early pathology, a separate VBA analysis was also conducted on the hippocampus using a mask of based on the Desikan probabilistic structural atlas [127-130]. This atlas, which is in Montreal neurological institute (MNI) standard space, was warped to the population atlas space through a 12 degree of freedom affine registration of an accompanying MNI space FA map to the population space FA map.

The VBA analysis utilized nonparametric permutation testing using the randomize function in FSL [131] along with threshold free cluster enhancement [132]. Prior to the VBA, all metric maps were smoothed with a 4mm full width half max Gaussian smoothing kernel. As with the tractography analysis, the effect of age and sex was controlled and the main effect of each biomarker on the diffusion metrics of interest was tested. For each permutation test, 25,000 permutations were carried out. Multiple comparisons were accounted for through the use of a family wise error threshold of $p \leq 0 .05$. Once again, this analysis was carried out for the FWE FA, MD, *f*-value, and the DTI FA and MD. While all analysis took place in the population template space, these maps were warped to MNI via the inverse warp used for the hippocampus map for standardized reporting and visualization.

5.4 Results

5.4.1 Demographics and CSF

Table 5.1 contains the Pearson's correlation coefficients between age and the CSF markers. One subject (male, APOE4+, FH-) was censured based on poor image quality along with an especially high value on the NFL assay that was more than 5.5 standard deviations above the group mean. This left 69 participants in the remainder of the analyses. Age was positively correlated with MCP, YKL-40, and $pTau_{181}$ ($P < 0.05$) and most strongly correlated with NFL ($P< 0.001$). Several CSF markers were correlated with one another with the strongest correlations being between sAPPα and sAPPβ ($\rho = 0.954$, $P < 0.001$) as well as $pTau_{181}$and tTau ($\rho = 0.876$, $P < 0.001$). The APOE4+ group displayed a lower ($P < 0.005$) mean Aβ42 value (655 ± 168) compared to the APOE4- group (797 ± 192). None of the markers were significantly associated with sex or parental family history of AD. These value were computed after censure of the subject noted above.

5.4.2 Tractography

Tables 5.2 and 5.3 contain the results from tractography for relationships found significant at the uncorrected p = 0.05 threshold. This table also shows the corrected significance level once multiple comparisons are considered. No correlations were significant after false discovery rate correction.

	sAPPα	sAPPβ	MCP	YKL	NFL	Aβ42	tTau	pTau$_{181}$
Age	0.057	0.028	0.321*	0.300*	0.546†	-0.190	0.202	0.237*
sAPPα		0.954†	-0.399†	0.385†	0.053	0.229	0.516†	0.631†
sAPPβ			-0.385†	0.436†	0.040	0.328*	0.571†	0.663†
MCP				0.009	0.117	-0.241	-0.145	-0.318
YKL-40					0.193	0.299*	0.517†	0.559†
NFL						0.095	0.319*	0.314*
Aβ42							0.188	0.230
tTau								0.876*

Table 5.1: Linear Pearson Correlation. Significant correlations at $P < 0.05$ (*) and $P < 0.001$ (†) are noted.

Method	Tract	Metric	Predictor	Uncorrected P	FDR
DTI	CC-IV	MD	pTau$_{181}$ / Aβ42	0.0005	0.0002
DTI	CC-IV	MD	YKL-40/ Aβ42	0.0009	0.0005
DTI	CC-IV	MD	tTau / Aβ42	0.0010	0.0007
DTI	CC-III	MD	tTau / Aβ42	0.0011	0.0010
DTI	CC-III	MD	pTau$_{181}$ / Aβ42	0.0017	0.0012
DTI	CC-IV	MD	pTau$_{181}$	0.0022	0.0014
DTI	CC-III	MD	pTau$_{181}$	0.0029	0.0017
DTI	CC-IV	MD	tTau	0.0036	0.0019
DTI	CC-III	MD	tTau	0.0038	0.0021
DTI	CC-III	MD	YKL-40 / Aβ42	0.0041	0.0024
DTI	CC-IV	MD	YKL-40	0.0058	0.0026
DTI	CC-V	MD	YKL-40 / Aβ42	0.0244	0.0029

Table 5.2: DTI tractography results with an uncorrected P ≤ 0.05 along with the false discovery rate α value.

All DTI results showed a positive correlation between the MD and CSF biomarkers. Of the seven ROIs investigated, the ROIs situated in the posterior portions of the corpus callosum (CC-III, CC-IV, and CC-V) were the only ones which showed an association with CSF biomarkers, including $pTau_{181}$, tTau, and YKL-40 as well as the ratio of each to Aβ42. The most robust results were for the ratios of markers as opposed to individual markers.

Method	Tract	Metric	Predictor	Uncorrected P	FDR
FWE	CC-I	f	$pTau_{181}$ / Aβ42	0.0005	0.0002
FWE	Cingulum	f	$pTau_{181}$ / Aβ42	0.0007	0.0003
FWE	CC-I	f	YKL-40 / Aβ42	0.0010	0.0005
FWE	CC-I	f	sAPPβ / Aβ42	0.0022	0.0006
FWE	Cingulum	f	sAPPβ / Aβ42	0.0024	0.0008
FWE	Cingulum	f	sAPPα / Aβ42	0.0035	0.0010
FWE	CC-I	f	tTau / Aβ42	0.0035	0.0011
FWE	Cingulum	f	$pTau_{181}$	0.0051	0.0013
FWE	CC-I	f	sAPPα / Aβ42	0.0065	0.0014
FWE	Cingulum	f	YKL-40 / Aβ42	0.0101	0.0016
FWE	CC-IV	f	$pTau_{181}$	0.0114	0.0017
FWE	Cingulum	f	tTau / Aβ42	0.0202	0.0019
FWE	CC-III	f	$pTau_{181}$ / Aβ42	0.0359	0.0021

Table 5.3: FWE tractography results with an uncorrected P ≤ 0.05 along with the false discovery rate α value.

For the FWE metrics, only the *f*-value showed a correlation with the CSF biomarkers. As with DTI MD, the *f*-value was positively correlated with the CSF biomarkers. However, in this case the tracts that were affected were primarily the cingulum bundles and CC-I. The FWE *f*-value showed a positive relationship with $pTau_{181}$, $pTau_{181}/A\beta42$, tTau/Aβ42, YKL-40/Aβ42, sAPPα/Aβ42 and sAPPβ/Aβ42.

5.4.3 Voxel Based Analysis

The voxel based analysis revealed widespread areas where diffusion metrics were related to $pTau_{181}/A\beta42$, tTau/ Aβ42, sAPPα/Aβ42 and sAPPβ/Aβ42 in both DTI and FWE analyses. For FWE but not DTI, $pTau_{181}$ was significantly correlated with diffusion measures. **Tables 5.4 and 5.5** records all significant clusters with extent ≥ 50 mm^3 found in both analyses. An explicit cluster size threshold is not needed when using TFCE as this threshold is strictly for reporting. As was seen in the tractography analysis, the only metrics which showed a significant relation were DTI MD and FWE *f*-value. Likewise, the relationship was positive for all of the clusters identified. An additional summary of the overall extent of significant findings can be found in **Table 5.6**.

Biomarker	MNI Coordinates (x,y,z)	Peak T value	k (mm3)	Region
pTau$_{181}$	(-41, -24, -8)	4.54	140	L inferior frontal-occipital fasciculus
pTau$_{181}$	(-29, -23, 23)	4.67	136	L posterior corona radiata
pTau$_{181}$	(-50, -31, -20)	4.81	128	L inferior temporal gyrus white matter
tTau / Aβ42	(-35, -48, -12)	6.69	3223	L fusiform gyrus white matter
tTau / Aβ42	(-20, 45, 5)	4.73	355	L anterior corona radiata
tTau / Aβ42	(-36, -76, -5)	5.15	69	L inferior occipital gyrus white matter
pTau$_{181}$ / Aβ42	(-35, -48, -12)	7.94	31689	L fusiform gyrus white matter
pTau$_{181}$ / Aβ42	(38, -40, -17)	5.64	1338	R fusiform gyrus white matter
pTau$_{181}$ / Aβ42	(-36, -3, -31)	5.47	1178	L inferior temporal gyrus white matter
pTau$_{181}$ / Aβ42	(36, -3, 24)	5.42	522	R inferior temporal gyrus white matter
pTau$_{181}$ / Aβ42	(-35, -8, -7)	4.64	379	L insular gyrus
pTau$_{181}$ / Aβ42	(17, 56, 10)	5.99	135	R superior frontal gyrus white matter
pTau$_{181}$ / Aβ42	(40, 12, 21)	4.38	122	R inferior frontal gyrus white matter
pTau$_{181}$ / Aβ42	(-8, -12, 40)	3.13	68	L cingulate gyrus
sAPPα / Aβ42	(-46, -18, -12)	5.47	5935	L middle temporal gyrus white matter
sAPPα / Aβ42	(-15, 49, 10)	5.19	2957	L superior frontal gyrus white matter
sAPPα / Aβ42	(-27, 21, 29)	4.52	1061	L middle frontal gyrus white matter
sAPPα / Aβ42	(-35, -2, -31)	5.46	691	L inferior temporal gyrus white matter
sAPPα / Aβ42	(-42, -6, 27)	4.77	523	L superior longitudinal fasciculus
sAPPα / Aβ42	(-28, 16, -1)	5.61	509	L external capsule/inferior fronto-
sAPPα / Aβ42	(-36, -7, -6)	4.83	307	L insular gyrus
sAPPα / Aβ42	(-18, -7, 48)	3.71	172	L superior frontal gyrus white matter
sAPPα / Aβ42	(-28, -21, 21)	3.72	160	L superior corona radiata
sAPPα / Aβ42	(-14, 39, 37)	3.82	96	L superior frontal gyrus white matter
sAPPα / Aβ42	(-32, -11, 36)	4.42	96	L superior longitudinal fasciculus
sAPPα / Aβ42	(-12, 25, 42)	3.73	57	L superior frontal gyrus white matter
sAPPβ / Aβ42	(-36, -49, -12)	6.21	11941	L fusiform gyrus white matter
sAPPβ / Aβ42	(-15, 49, 10)	5.71	4845	L superior frontal gyrus white matter
sAPPβ / Aβ42	(38, -40, -17)	5.72	1572	R fusiform gyrus white matter
sAPPβ / Aβ42	(-27, 22, 28)	4.8	1562	L middle frontal gyrus white matter
sAPPβ / Aβ42	(-36, -3, -32)	6.05	1306	L inferior temporal gyrus white matter
sAPPβ / Aβ42	(-32, -11, 36)	5.16	1044	L precentral gyrus white matter
sAPPβ / Aβ42	(22, 52, 5)	5.11	547	R superior frontal gyrus white matter
sAPPβ / Aβ42	(37, 1, 27)	4.92	506	R precentral gyrus white matter
sAPPβ / Aβ42	(-17, -6, 48)	3.77	450	L superior frontal gyrus white matter
sAPPβ / Aβ42	(30, 19, 27)	4.26	395	R middle frontal gyrus white matter
sAPPβ / Aβ42	(27, 43, 5)	4.17	378	R middle frontal gyrus white matter
sAPPβ / Aβ42	(-13, -25, 54)	4.91	234	L precentral gyrus white matter
sAPPβ / Aβ42	(47, -38, 30)	4.55	137	R supramarginal gyrus white matter
sAPPβ / Aβ42	(-15, 0, 58)	3.7	81	L superior frontal gyrus white matter
sAPPβ / Aβ42	(-51, -8, 20)	4.82	78	L postcentral gyrus white matter

Table 5.4: Listing of all significant clusters for which the FWE f-value was correlated to one of the predictors. Information presented for each cluster includes diffusion metric and the related biomarker, relevant white matter region, MNI coordinates (in mm) of the peak t-value, and the cluster size (k).

Biomarker	MNI Coordinates (x,y,z)	Peak T value	k (mm3)	Region
tTau / Aβ42	(-50, -21, -19)	5.39	3913	L parietal operculum
tTau / Aβ42	(24, 25, -13)	5.2	497	R posterior orbital gyrus white matter
tTau / Aβ42	(36, 2, -33)	5.26	381	R inferior temporal gyrus white
tTau / Aβ42	(54, -24, -16)	4.75	353	R middle temporal gyrus white matter
tTau / Aβ42	(37, -7, -5)	5.45	130	R insular gyrus
tTau / Aβ42	(35, 1, 19)	4.7	100	R precentral gyrus white matter
pTau$_{181}$ / Aβ42	(-53, -33, -15)	6.36	5640	L inferior temporal gyrus white
pTau$_{181}$ / Aβ42	(36, 1, -33)	5.8	491	R inferior temporal gyrus white
pTau$_{181}$ / Aβ42	(28, 14, -8)	5.24	467	R inferior fronto-occipital fasciculus
pTau$_{181}$ / Aβ42	(36, 3, 18)	5.5	351	R precentral gyrus white matter
pTau$_{181}$ / Aβ42	(35, -6, 23)	5.13	255	R precentral gyrus white matter
pTau$_{181}$ / Aβ42	(52, -21, -23)	5.04	194	R inferior temporal gyrus white
sAPPα / Aβ42	(-53, -33, -15)	5.68	4179	L inferior temporal gyrus white
sAPPα / Aβ42	(-35, 39, -1)	5.08	1589	L inferior frontal gyrus white matter
sAPPα / Aβ42	(-43, -5, 31)	4.41	552	L precentral gyrus white matter
sAPPα / Aβ42	(35, 4, 16)	4.65	460	R inferior frontal gyrus white matter
sAPPα / Aβ42	(20, -4, -9)	6.24	445	R posterior limb of the internal
sAPPα / Aβ42	(30, 14, -9)	5.33	335	R external capsule
sAPPα / Aβ42	(-45, -6, 39)	4.22	143	L precentral gyrus white matter
sAPPα / Aβ42	(37, -8, -4)	5.45	134	R insular gyrus
sAPPα / Aβ42	(-49, -17, 25)	5.25	101	L postcentral gyrus
sAPPα / Aβ42	(17, -1, 3)	4.08	100	R globus pallidus
sAPPα / Aβ42	(35, -7, 22)	4.12	90	R superior longitudinal fasciculus
sAPPα / Aβ42	(-22, -64, 35)	4.69	64	L superior parietal lobule white
sAPPα / Aβ42	(50, -2, 28)	5.43	63	R precentral gyrus white matter
sAPPα / Aβ42	(-32, 9, -11)	3.86	62	L insular gyrus
sAPPα / Aβ42	(51, -21,-23)	4.39	54	R inferior temporal gyrus white
sAPPβ / Aβ42	(-53, -33, -15)	6.15	5342	L middle temporal gyrus white matter
sAPPβ / Aβ42	(51, -21, -23)	5.22	96	R inferior temporal gyrus white

Table 5.5: Listing of all significant clusters for which the DTI MD was correlated to one of the predictors. Information presented for each cluster includes diffusion metric and the related biomarker, relevant white matter region, MNI coordinates (in mm) of the peak t-value, and the cluster size (k).

	pTau$_{181}$	pTau$_{181}$/ Aβ42	tTau$_{181}$/ Aβ42	sAPPα/ Aβ42	sAPPβ/ Aβ42
FWE: f-value	404	35509	3701	12784	25263
DTI: MD	~	7558	5398	8453	5572

Table 5.6: The total extent of significant voxels (mm^3).

The spatial distribution of clusters for which FWE *f*-value or DTI MD were correlated with $pTau_{181}/A\beta 42$ is displayed in **Figures 5.3 and 5.4**, respectively. Scatter plots corresponding to the single largest clusters from **Figures 5.3- 5.4** are shown in **Figures 5.5-5.6**. **Tables 5.7 and 5.8** show the relationship between the areas related to each biomarker or biomarker ratio. With the exception of the clusters due to $pTau_{181}$ alone, there is substantial overlap between all FWE clusters with one another and all DTI clusters with one another. There were no significant clusters for either diffusion method in the hippocampus.

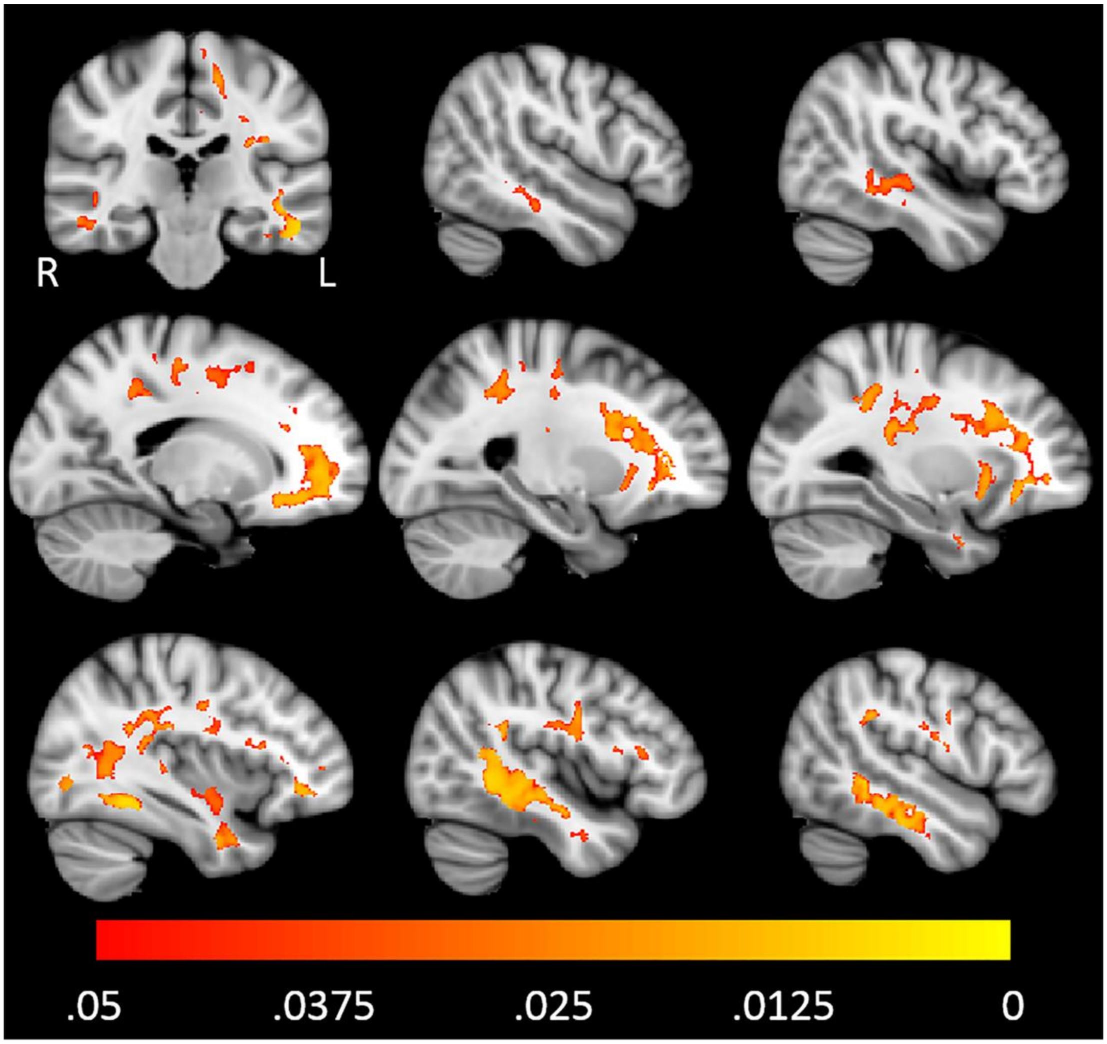

Figure 5.3: Higher levels of pTau$_{181}$/Aβ42 were associated with increased FWE *f*-value throughout white matter. The red-yellow color scale above shows the familywise error corrected P-value. The underlay image is a T1w MNI template with 1 mm isotropic resolution.

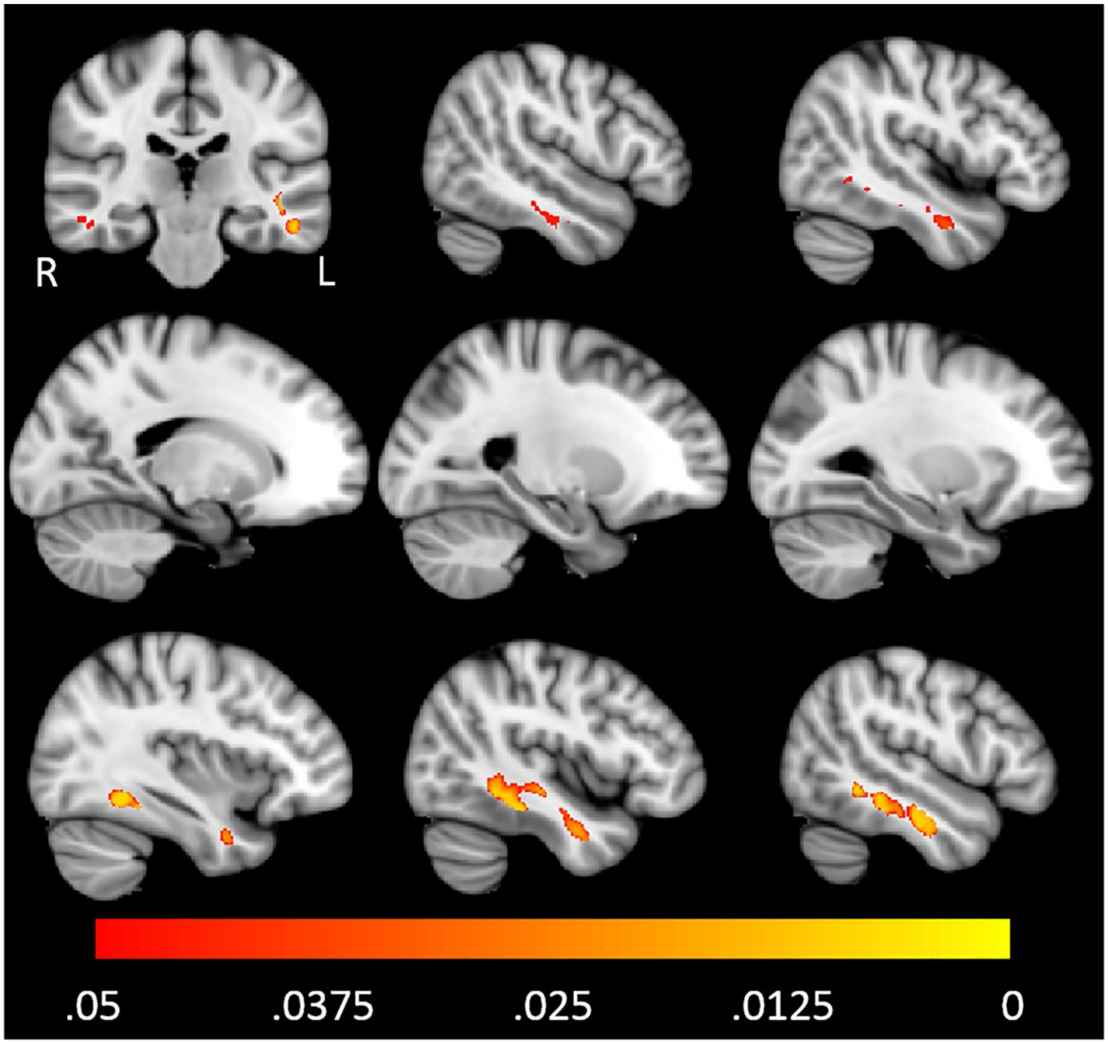

Figure 5.4: Higher levels of pTau181/Aβ42 were associated with increased DTI MD primarily in the left and right temporal lobes. The color scale, underlay, and presented slices are the same as those in Figure 5.3.

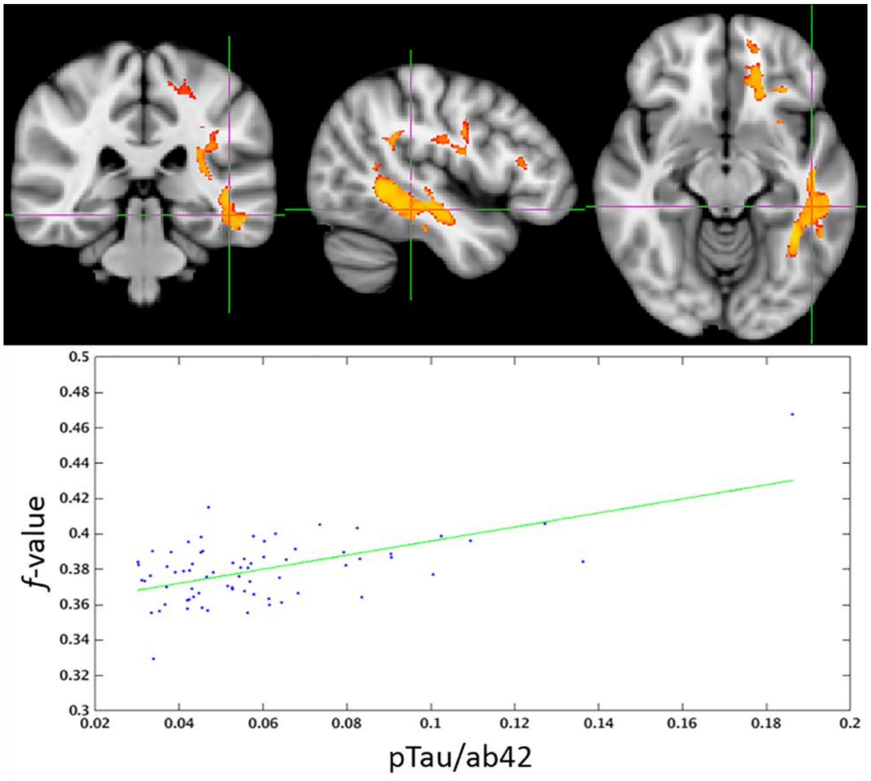

Figure 5.5: The largest contiguous cluster for which FWE *f*-value correlated with $pTau_{181}/A\beta42$. All other clusters were masked out of the image. The color scale is the same as that of Figure 5.3.

	f ~ $pTau_{181}/A\beta42$	f ~ tTau/Aβ42	f ~ sAPPα/Aβ42	f ~ sAPPβ/Aβ42
f ~ $pTau_{181}$	94 %	36 %	67 %	80 %
f ~ $pTau_{181}/A\beta42$		100 %	93 %	80 %
f ~ tTau/Aβ42			74 %	93 %
f ~ sAPPα/Aβ42				98 %

Table 5.7: The percent overlap between the significant finding maps using the FWE *f*-value. These are computed as the percent of the smaller map which overlaps with the larger map.

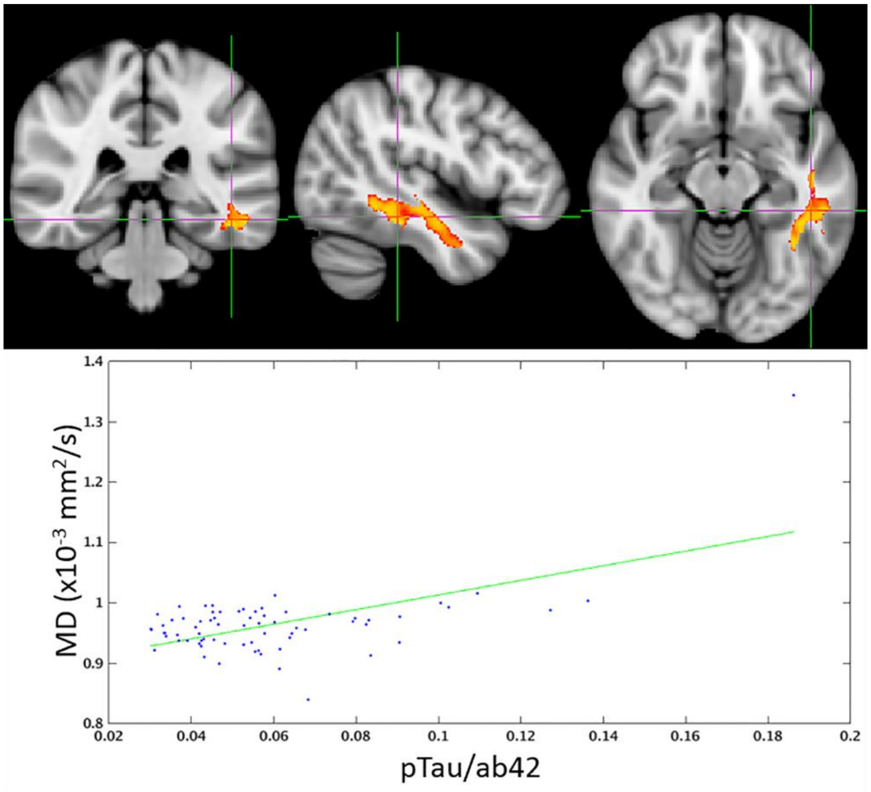

Figure 5.6: The largest contiguous cluster for which DTI MD correlated with $pTau_{181}/A\beta42$. All other clusters were masked out of the image. The color scale is the same as that of Figure 5.3.

	MD ~ tTau/Aβ42	MD ~ sAPPα/Aβ42	MD ~ sAPPβ/Aβ42
MD ~ $pTau_{181}$/Aβ42	92 %	60 %	85 %
MD ~ tTau/Aβ42		64 %	66 %
MD ~ sAPPα/Aβ42			76 %

Table 5.8: The percent overlap between the significant finding maps using the DTI MD. These are computed as the percent of the smaller map which overlaps with the larger map.

5.5 Discussion and Conclusion

An estimated 5.2 million Americans have AD. In the absence of effective treatments for the disease, there has been an increased focus on understanding the pathological features that occur in the earliest stages of the disease. Early identification is important for detecting pathological features that may be modified at an early stage in the disease prior to significant cell loss, in addition to identifying candidates for clinical trials. In this study, we tested the extent to which preclinical AD pathology involves alteration to white matter microstructure. White matter alteration may be an early feature of the disease, and new methods for modeling complex diffusion are expected to be sensitive to this early pathology. We found significant associations between markers of AD pathology measured in CSF, and white matter microstructure, especially as indicated by FWE f-value. In particular, elevated ratios of pTau/Aβ_{42} and tTau/Aβ_{42} were robustly associated with higher free water or f-value in frontal and temporal lobe white matter. A novel marker of the amyloid pathway (sAPPβ) also showed a robust association with altered microstructure as shown on FWE-DTI, especially when combined as a ratio with Aβ_{42}. It was previously shown in a smaller group of participants (n=42) that tau and Aβ_{42} ratios are associated with MD[101]. Interestingly, the results of the current study also showed that MD derived from standard DTI was associated with higher pTau/Aβ_{42} in CSF, with peaks of association in temporal lobe white matter. Of note, the current study extends these findings by showing that FWE-DTI appears to demonstrate greater sensitivity to associations between AD pathology and white matter microstructure compared to standard DTI.

Non-zero *f*-values that are measured in tissue distal from CSF may reflect the relative volume of extracellular space in the tissue. In the context of aging and AD, this signal could be due to loss of axons, or loss of myelin in brain white matter. The pathology of AD includes hyperphosphorylation of tau protein, resulting in axonal abnormalities and displacement of tau to neuronal cell bodies[133]. Markers in this study that were related to tau (tTau and pTau), in addition to NFL, were strongly associated with white matter microstructural features as shown on FWE-DTI. Given that tau and NFL are components of the axonal cytoskeleton, these results may suggest that the *f*-value is sensitive to early axonal degeneration.

Amyloid pathology has also been linked with axonal degeneration. Hippocampal neurons cultured in vitro show axonal degeneration due to $A\beta_{42}$ toxicity, an event that occurs prior to cell body death [134] . Other studies suggest that pathological changes in AD include leakage of amyloid from the extracellular space into the neuron, for example, at the axon hillock [135], causing subsequent axonal pathology. Krstic et al. review evidence that inflammation is involved in increasing neuronal cell vulnerability [136], and indeed, the results of the tractography analysis showed a positive association between MD and YKL-40, a marker of microglial activation—suggesting inflammation—as well as the ratio of YKL-40 to $A\beta_{42}$. The results did not survive correction for multiple corrections, but are suggestive. Additional studies are needed to determine the importance of inflammation in AD pathogenesis.

It is also of interest that higher $sAPP\beta/A\beta_{42}$ showed a widespread association with higher *f*-value across bilateral temporal and frontal white matter. sAPPβ is a product of amyloid precursor protein (APP) cleavage by β-secretase. Cleavage of APP via this pathway ultimately leads to formation of deposited amyloid plaques. Prior to deposition, however, products of the β-secretase pathway include increases in amyloid-β oligomers, which may be more toxic to neuronal cells than deposited plaques [137]. While direct measures of oligomeric Aβ in CSF are unavailable, higher sAPPβ in CSF is likely proportional to oligomer levels. Additionally, a higher $sAPP\beta/A\beta_{42}$ ratio may indicate a proportionally higher level of toxic oligomeric amyloid prior to extensive deposition as measured by reductions of $A\beta_{42}$ in CSF. To the author's knowledge, this is the first study showing a link between elevated β-secretase cleavage of APP and *in vivo* evidence of axonal damage as shown on diffusion-weighted imaging in humans.

The study of preclinical AD has been significantly enhanced by focusing on carriers of autosomal dominant mutations for AD prior to development of symptomatic AD [138]. In sporadic AD, the field has centered on studying individuals at increased risk due to *APOE* ε4 genotype and parental history of AD. Several studies from our group and others have suggested that family history of AD is associated with preclinical brain changes [139–142], including significant alterations to white matter as shown on DTI [37,143]. While risk factors such as parental history of AD and *APOE* ε4 are useful for identifying individuals at greater risk for progression to AD, the capability of obtaining CSF biomarkers that are direct measures of existing pathological features provides an enhanced opportunity for studying preclinical AD. This is the first study demonstrating an association between CSF biomarkers and white matter microstructure using the FWE model in an asymptomatic population at increased risk for AD.

Chapter 6

Concluding Remarks

> *What is a model? A model is like an Austrian timetable. Since Austrian trains are always late, a Prussian visitor asks an Austrian conductor why they bother to print timetables. The conductor replies, "If we did not, how would we know how late the trains are?" – Victor F. Weisskopf*

6.1 Contributions and Lessons Learned

This work presents a straightforward implementation of the FWE model first proposed by Pierpaoli and Jones [42]. Eschewing the heavy regularization required to solve the ill posed problem suggested by Pasternak [43] this project instead approached the problem with the goal of catering an acquisition and reconstruction.

An optimal acquisition was identified and the first ever characterization of the FWE model's performance was carried out through Monte Carlo simulations. The ability to resolve PVE was then confirmed through deterministic tractography. Indeed, the FWE model is more capable of this task than FLAIR DTI while maintaining higher SNR, greater anatomical coverage, and superior time efficiency. This study also provided the first supporting evidence for the theory that the isotropic signal arises from the extracellular space. What was certain was that the f-value corresponded to something beyond simple CSF PVE.

The FWE technique was then applied to a cohort of older individuals who had undergone a lumbar puncture to quantify CSF biomarkers of AD. This study provided a direct comparison with DTI as the individuals had a separate “standard” DTI scan. This comparison showed that the FWE *f*-value was more sensitive to widespread changes than any DTI metrics were. While it is unclear what the exact origin of the *f*-value is, it has been seen to be useful in discriminating subtle white matter changes.

Diffusion tensor imaging remains the most popular form of diffusion imaging despite the well-chronicled shortcoming of this method. The plethora of higher order diffusion models require longer scan times and arduous reconstruction methods. Nevertheless, the question remains, what exactly does the signal mean? That it arises from tissue microstructure is unquestioned, but deeper meaning is uncertain as many physiological factors are intermingled in the process of self-diffusion in the brain. For this reason DTI will likely persist due to its relative simplicity and proven sensitivity. What is presented in this work is an improvement to DTI that allows use in anatomical regions which were otherwise prohibited and provides additional information without significantly degrading the favorable characteristics of DTI.

6.2 Future Works

While generally pleased with and proud of my time at the University of Wisconsin exciting work remains undone.

This includes the use of the FWE model in brain tumor imaging. It is believed that the proposed model would be helpful in differentiating infiltrating tumor from inflammation and edema. This task has proven futile for typical diffusion imaging. Diffusion properties of edema would likely not match that of CSF, thus, the model may need modification of the idealized ADC. If successful, this project would represent a major contribution to brain imaging.

While this work has been limited to applications in the brain, there is no reason that this is necessary. It would be interesting to further investigate body imaging.

Ideally, the FWE framework could be extended by incorporating a kurtosis term for the diffusion tensor. In the intermediate b-value regime (≈ 2500 s/mm^2), the estimated isotropic volume fraction becomes larger. Non-Gaussian diffusion is accentuated as b-value increases which likely explains the increase in f-value. Another such method which describes this phenomenon is diffusion kurtosis imaging. It would be interesting to evaluate the kurtosis of the tensor with and without FWE. It is possible that the FWE term would mitigate all kurtosis.

Lastly, more work is needed to ascertain the origin of the isotopic compartment signal beyond partial volume effects. It is clear from the tractography study, chapter 4, that the signal arises from more than simple CSF partial voluming. As mentioned, DTI and indeed FWE are mathematical simplifications of a complex phenomenon. Even so, hope remains that histological studies may better be able to determine the validity of the extracellular space hypothesis. It would be interesting to determine if observations about the corpus callosum are repeatable in non-human primates. If indeed there is a consistent anterior to posterior variation in f then follow up histology could be useful.

References

1. Einstein A. On the movement of small particles suspended in staitionary liquids required by the molecular-kinetic theory of heat. Annelan der Phys. 1905;17(16):549–60.

2. Chenevert TL, Brunberg JA, Pipe JG. Anisotropic diffusion in human white matter: demonstration with MR techniques in vivo. Radiology. 1990;177:401–5.

3. Moseley ME, Cohen Y, Kucharczyk J, Mintorovitch J, Asgari HS, Wendland MF, Tsuruda J, Norman D. Diffusion-weighted MR imaging of anisotropic water diffusion in cat central nervous system. Radiology. 1990;176:439–45.

4. Stejskal EO, Tanner JE. Spin Diffusion Measurements: Spin Echoes in the Presence of a Time-Dependent Field Gradient. J Chem Phys [Internet]. 1965;42:288. Available from: http://link.aip.org/link/JCPSA6/v42/i1/p288/s1&Agg=doi

5. Jones DK, Horsfield M a, Simmons a. Optimal strategies for measuring diffusion in anisotropic systems by magnetic resonance imaging. Magn Reson Med [Internet]. 1999 Sep;42(3):515–25. Available from: http://www.ncbi.nlm.nih.gov/pubmed/10467296

6. Basser PJ, Mattiello J, LeBihan D. MR diffusion tensor spectroscopy and imaging. Biophys J. 1994;66:259–67.

7. Basser P, Mattiello J, LeBihan D. Estimation of the Effective Self-Diffusion Tensor from the NMR Spin Echo. J Magn Reson Ser …. 1994;(103):247–54.

8. Tuch DS, Reese TG, Wiegell MR, Makris N, Belliveau JW, Wedeen VJ. High angular resolution diffusion imaging reveals intravoxel white matter fiber heterogeneity. Magn Reson Med [Internet]. 2002 Oct [cited 2014 May 29];48(4):577–82. Available from: http://www.ncbi.nlm.nih.gov/pubmed/12353272

9. Jensen JH, Helpern JA. Quantifying Non-Gaussian Water Diffusion by Means of Pulsed-Field-Gradient MRI. 2003;859(2000):2154.

10. Jensen JH, Helpern J a, Ramani A, Lu H, Kaczynski K. Diffusional kurtosis imaging: the quantification of non-gaussian water diffusion by means of magnetic resonance imaging. Magn Reson Med [Internet]. 2005 Jun [cited 2013 Sep 19];53(6):1432–40. Available from: http://www.ncbi.nlm.nih.gov/pubmed/15906300

11. Hui ES, Cheung MM, Qi L, Wu EX. Towards better MR characterization of neural tissues using directional diffusion kurtosis analysis. Neuroimage [Internet]. 2008 Aug 1 [cited 2013 Sep 20];42(1):122–34. Available from: http://www.ncbi.nlm.nih.gov/pubmed/18524628

12. Callaghan PT. Principles of Nuclear Magnetic Resonance Microscopy [Internet]. Medical Physics. 1991. Available from: http://link.aip.org/link/?MPH/19/1121/1&Agg=doi

13. Wedeen V, Reese T, Tuch D, Weigel M, Dou J, Weiskoff R, Chessler D. Mapping fiber orientation spectra in cerebral white matter with Fourier-transform diffusion MRI. Proc Intl Sot Mag Reson Med 8. 2000. p. 5627–5627.

14. Wu YC, Alexander AL. Hybrid diffusion imaging. Neuroimage. 2007;36:617–29.

15. Assaf Y, Freidlin RZ, Rohde GK, Basser PJ. New modeling and experimental framework to characterize hindered and restricted water diffusion in brain white matter. Magn Reson Med. 2004;52:965–78.

16. Zhang H, Schneider T, Wheeler-Kingshott CA, Alexander DC. NODDI: practical in vivo neurite orientation dispersion and density imaging of the human brain. Neuroimage [Internet]. Elsevier Inc.; 2012 Jul 16 [cited 2013 Sep 16];61(4):1000–16. Available from: http://www.ncbi.nlm.nih.gov/pubmed/22484410

17. Wang Y, Wang Q, Haldar JP, Yeh F-C, Xie M, Sun P, Tu T-W, Trinkaus K, Klein RS, Cross AH, Song S-K. Quantification of increased cellularity during inflammatory demyelination. Brain. 2011;134:3590–601.

18. Pajevic S, Pierpaoli C. Color schemes to represent the orientation of anisotropic tissues from diffusion tensor data: application to white matter fiber tract mapping in the human brain. Magn Reson Med [Internet]. 2000 Jun;43(6):921. Available from: http://www.ncbi.nlm.nih.gov/pubmed/10861892

19. Mori S, Crain B, Chacko V, Van Ziji P. Three-dimensional tracking of axonal projections in the brain by magnetic resonance imaging. Ann Neurol. 1999;45(2):265–9.

20. Conturo TE, Lori NF, Cull TS, Akbudak E, Snyder AZ, Shimony JS, Mckinstry RC, Burton H, Raichle ME. Tracking neuronal fiber pathways in the living human brain. Proc Natl Acad Sci U S A. 1999;96(August):10422–7.

21. Basser PJ, Pajevic S, Pierpaoli C, Duda J, Aldroubi a. In vivo fiber tractography using DT-MRI data. Magn Reson Med [Internet]. 2000 Oct;44(4):625–32. Available from: http://www.ncbi.nlm.nih.gov/pubmed/11025519

22. Chenevert TL, Pipe JG, Williams DM, Brunberg JA. Quantitative measurement of tissue perfusion and diffusion in vivo. Magn Reson Med. 1991;17:197–212.

23. Beaulieu CF, Zhou X, Cofer GP, Johnson GA. Diffusion-weighted MR microscopy with fast spin-echo. Magn Reson Med. 1993;30:201–6.

24. Liu C, Bammer R, Kim D-H, Moseley ME. Self-navigated interleaved spiral (SNAILS): application to high-resolution diffusion tensor imaging. Magn Reson Med [Internet]. 2004 Dec [cited 2013 Oct 14];52(6):1388–96. Available from: http://www.ncbi.nlm.nih.gov/pubmed/15562493

25. Gmitro AF, Alexander AL. Use of a projection reconstruction method to decrease motion sensitivity in diffusion-weighted MRI. Magn Reson Med. 1993;29:835–8.

26. Pipe JG, Farthing VG, Forbes KP. Multishot diffusion-weighted FSE using PROPELLER MRI. Magn Reson Med. 2002;47:42–52.

27. Reese TG, Heid O, Weisskoff RM, Wedeen VJ. Reduction of eddy-current-induced distortion in diffusion MRI using a twice-refocused spin echo. Magn Reson Med [Internet]. 2003 Jan [cited 2014 Jun 2];49(1):177–82. Available from: http://www.ncbi.nlm.nih.gov/pubmed/12509835

28. Lin C, Bernstein M, Huston J, Fain S, Sw FS. Measurements of T1 Relaxation times at 3 . 0T : Implications for clinical MRA. International Society for Magnetic Resonance in Medicine Meeting. 2001. p. 1391.

29. Stanisz GJ, Odrobina EE, Pun J, Escaravage M, Graham SJ, Bronskill MJ, Henkelman RM. T1, T2 relaxation and magnetization transfer in tissue at 3T. Magn Reson Med [Internet]. 2005 Sep [cited 2013 Sep 23];54(3):507–12. Available from: http://www.ncbi.nlm.nih.gov/pubmed/16086319

30. Duyckaerts C. Neuropathologic classification of dementias: introduction. In: Vinken P, Bruyn G, editors. Handbook of Clinical Neurology. 2008. p. 147–59.

31. Larson E, Shadlen M, Wang L, McCormick W, Bowen J, Teri L, Kukull W. Survival after initial diagnosis of Alzheimer disease. Ann Intern Med. 2004;140:501–11.

32. Cummings J. Cognitive and behavioral heterogeneity in Alzheimer's disease: seeking the neurobiological basis. Neurobiol Aging. 2000 Dec;21(6):845–61.

33. Farrer LA, Cupples LA, Haines JL, Hyman B, Kukull WA, Mayeux R, Myers RH, Pericak-Vance MA, Risch N, van Duijn CM. Effects of Age, Sex, and Ethnicity on the Association Between Apolipoprotein E Genotype and Alzheimer Disease: A Meta-analysis. JAMA: The Journal of the American Medical Association. 1997. p. 1349–56.

34. Cupples LA, Farrer L a, Sadovnick a D, Relkin N, Whitehouse P, Green RC. Estimating risk curves for first-degree relatives of patients with Alzheimer's disease: The REVEAL study. Genet Med. 2004 Aug;6(4):192–6.

35. Desai M, Sudol K, Janelsins M, Mastrangelo M, Frazer M, Bowers W. Triple-transgenic Alzheimer's disease mice exhibit region-specific abnormalities in brain myelination patterns prior to appearance of amyloid and tau pathology. Glia. 2009;57(1):54–65.

36. Berlot R, Metzler-Baddeley C, Jones DK, O'Sullivan MJ. CSF contamination contributes to apparent microstructural alterations in mild cognitive impairment. Neuroimage [Internet]. The Authors; 2014 Feb 3 [cited 2014 Feb 11];1–9. Available from: http://www.ncbi.nlm.nih.gov/pubmed/24503415

37. Bendlin B, Ries M, Canu E, Sodhi A. White matter is altered with parental family history of Alzheimer's disease. Alzheimer's … [Internet]. 2010 [cited 2014 Mar 1];6(5):394–403. Available from: http://www.sciencedirect.com/science/article/pii/S1552526009023334

38. Basser PJ, Mattiello J, LeBihan D. MR diffusion tensor spectroscopy and imaging. Biophys J [Internet]. 1994 Jan;66(1):259–67. Available from: http://www.pubmedcentral.nih.gov/articlerender.fcgi?artid=1275686&tool=pmcentrez&rendertype=abstract

39. Alexander AL, Lee JE, Lazar M, Field AS. Diffusion Tensor Imaging of the Brain. 2007;4(July):316–29.

40. Alexander AL, Hasan KM, Lazar M, Tsuruda JS, Parker DL. Analysis of Partial Volume Effects in Diffusion-Tensor MRI. 2001;780:770–80.

41. Sener RN. Diffusion MRI : apparent diffusion coefcient (ADC) values in the normal brain and a classication of brain disorders based on ADC values. Comput Med Imaging Graph. 2001;25:299–326.

42. Pierpaoli C, Jones DK. Removing CSF Contamination in Brain DT-MRIs by Using a Two-Compartment Tensor Model. International Society for Magnetic Resonance in Medicine Meeting. 2004. p. 1215.

43. Pasternak O, Sochen N, Gur Y, Intrator N, Assaf Y. Free water elimination and mapping from diffusion MRI. Magn Reson Med

[Internet]. 2009 Sep [cited 2013 Sep 23];62(3):717–30. Available from: http://www.ncbi.nlm.nih.gov/pubmed/19623619

44. Pasternak O, Shenton ME, Westin C-F. Estimation of extracellular volume from regularized multi-shell diffusion MRI. Med Image Comput Comput Assist Interv [Internet]. 2012 Jan;15(Pt 2):305–12. Available from: http://www.ncbi.nlm.nih.gov/pubmed/23286062

45. Wang Y, Wang Q, Haldar JP, Yeh F-C, Xie M, Sun P, Tu T-W, Trinkaus K, Klein RS, Cross AH, Song S-K. Quantification of increased cellularity during inflammatory demyelination. Brain [Internet]. 2011;134:3590–601. Available from: http://www.pubmedcentral.nih.gov/articlerender.fcgi?artid=3235568&tool=pmcentrez&rendertype=abstract

46. Scherrer B, Warfield SK. Parametric representation of multiple white matter fascicles from cube and sphere diffusion MRI. PLoS One [Internet]. 2012 Jan [cited 2013 Oct 1];7(11):e48232. Available from: http://www.pubmedcentral.nih.gov/articlerender.fcgi?artid=3506641&tool=pmcentrez&rendertype=abstract

47. Assaf Y, Freidlin RZ, Rohde GK, Basser PJ. New modeling and experimental framework to characterize hindered and restricted water diffusion in brain white matter. Magn Reson Med. 2004;52:965–78.

48. Koay CG, Chang L-C, Carew JD, Pierpaoli C, Basser PJ. A unifying theoretical and algorithmic framework for least squares methods of estimation in diffusion tensor imaging. J Magn Reson [Internet]. 2006 Sep [cited 2013 Oct 14];182(1):115–25. Available from: http://www.ncbi.nlm.nih.gov/pubmed/16828568

49. Koay CG, Ozarslan E, Johnson KM, Meyerand ME. Sparse and optimal acquisition design for diffusion MRI and beyond. Med Phys [Internet]. 2012 May;39(5):2499–511. Available from: http://www.pubmedcentral.nih.gov/articlerender.fcgi?artid=3344880&tool=pmcentrez&rendertype=abstract

50. Turner R, Le Bihan D, Maier J, Vavrek R, Hedges LK, Pekar J. Echo-planar imaging of intravoxel incoherent motion. Radiology. 1990;177(2):407–14.

51. Montgomery DC, Runger GC, Hubele NF. Engineering Statistics [Internet]. Statistics. 1987. Available from: http://books.google.com/books?hl=en&lr=&id=O-XmUTtpgSUC&oi=fnd&pg=PA488&dq=Engineering+Statistics&ots=BXJawF5wW0&sig=whBpTrDRLRDbtLs7usRxcWi3F6U

52. Pierpaoli C, Basser P. Toward a quantitative assessment of diffusion anisotropy. Magn Reson Med [Internet]. 1996 [cited 2014 Jun 23]; Available from: http://onlinelibrary.wiley.com/doi/10.1002/mrm.1910360612/full

53. Mulkern R, Haker S, Maier S. On high b diffusion imaging in the human brain: ruminations and experimental insights. Magn Reson Imaging [Internet]. 2009 [cited 2014 Jun 11];27(8):1151–62. Available from: http://www.sciencedirect.com/science/article/pii/S0730725X09000873

54. Koay CG, Basser PJ. Analytically exact correction scheme for signal extraction from noisy magnitude MR signals. J Magn Reson [Internet]. 2006 Apr [cited 2014 Mar 19];179(2):317–22. Available from: http://www.ncbi.nlm.nih.gov/pubmed/16488635

55. Concha L, Gross DW, Beaulieu C. Diffusion tensor tractography of the limbic system. AJNR Am J Neuroradiol [Internet]. 2005 Oct;26(9):2267–74. Available from: http://www.ncbi.nlm.nih.gov/pubmed/16219832

56. Baron C a, Beaulieu C. Acquisition strategy to reduce cerebrospinal fluid partial volume effects for improved DTI tractography. Magn Reson Med [Internet]. 2014 Apr 10 [cited 2014 Jun 28];00:1–10. Available from: http://www.ncbi.nlm.nih.gov/pubmed/24723303

57. Pasternak O, Westin C-F, Bouix S, Seidman LJ, Goldstein JM, Woo T-UW, Petryshen TL, Mesholam-Gately RI, McCarley RW, Kikinis R, Shenton ME, Kubicki M. Excessive extracellular volume reveals a neurodegenerative pattern in schizophrenia onset. J Neurosci [Internet]. 2012 Nov 28 [cited 2013 Oct 3];32(48):17365–72. Available from:

http://www.pubmedcentral.nih.gov/articlerender.fcgi?artid=3549332&tool=pmcentrez&rendertype=abstract

58. Metzler-Baddeley C, O'Sullivan MJ, Bells S, Pasternak O, Jones DK. How and how not to correct for CSF-contamination in diffusion MRI. Neuroimage. Elsevier Inc.; 2012 Jan;59(2):1394–403.

59. Nicholson C, Syková E. Extracellular space structure revealed by diffusion analysis. Trends Neurosci [Internet]. 1998 May;21(5):207–15. Available from: http://www.ncbi.nlm.nih.gov/pubmed/9610885

60. Beaulieu C. The basis of anisotropic water diffusion in the nervous system - a technical review. NMR Biomed [Internet]. 2002 [cited 2013 Sep 20];15(7-8):435–55. Available from: http://www.ncbi.nlm.nih.gov/pubmed/12489094

61. Niendorf T, Dijkhuizen RM, Norris DG, van Lookeren Campagne M, Nicolay K. Biexponential diffusion attenuation in various states of brain tissue: implications for diffusion-weighted imaging. Magn Reson Med [Internet]. 1996 Dec;36(6):847–57. Available from: http://www.ncbi.nlm.nih.gov/pubmed/8946350

62. Assaf Y, Cohen Y. Non-mono-exponential attenuation of water and N-acetyl aspartate signals due to diffusion in brain tissue. J Magn Reson [Internet]. 1998 Mar;131(1):69–85. Available from: http://www.ncbi.nlm.nih.gov/pubmed/9533908

63. Mulkern R V, Gudbjartsson H, Westin CF, Zengingonul HP, Gartner W, Guttmann CR, Robertson RL, Kyriakos W, Schwartz R, Holtzman D, Jolesz F a, Maier SE. Multi-component apparent diffusion coefficients in human brain. NMR Biomed [Internet]. 1999 Feb;12(1):51–62. Available from: http://www.ncbi.nlm.nih.gov/pubmed/10195330

64. Inglis B a, Bossart EL, Buckley DL, Wirth ED, Mareci TH. Visualization of neural tissue water compartments using biexponential diffusion tensor MRI. Magn Reson Med [Internet]. 2001 Apr;45(4):580–7. Available from: http://www.ncbi.nlm.nih.gov/pubmed/11283985

65. Maier SE, Vajapeyam S, Mamata H, Westin C-F, Jolesz F a, Mulkern R V. Biexponential diffusion tensor analysis of human brain diffusion

data. Magn Reson Med [Internet]. 2004 Feb [cited 2013 Oct 14];51(2):321–30. Available from: http://www.ncbi.nlm.nih.gov/pubmed/14755658

66. Duong T, Ackerman J, Ying H, Neil J. Evaluation of Extra- and Intracellular Apparent Diffusion in Normal and Globally Ischemic Rat Brain via 19F NMR. Magn Reson Med. 1998;40(1):1–13.

67. Alexander AL, Hurley S a, Samsonov A a, Adluru N, Hosseinbor AP, Mossahebi P, Tromp DPM, Zakszewski E, Field AS. Characterization of cerebral white matter properties using quantitative magnetic resonance imaging stains. Brain Connect [Internet]. 2011 Jan [cited 2014 Aug 12];1(6):423–46. Available from: http://www.pubmedcentral.nih.gov/articlerender.fcgi?artid=3360545&tool=pmcentrez&rendertype=abstract

68. Metzler-Baddeley C, Jones DK, Belaroussi B, Aggleton JP, O'Sullivan MJ. Frontotemporal connections in episodic memory and aging: a diffusion MRI tractography study. J Neurosci. 2011 Sep;31(37):13236–45.

69. Metzler-Baddeley C, Jones DK, Belaroussi B, Aggleton JP, O'Sullivan MJ. Frontotemporal connections in episodic memory and aging: a diffusion MRI tractography study. J Neurosci [Internet]. 2011 Sep 14 [cited 2014 Jul 23];31(37):13236–45. Available from: http://www.ncbi.nlm.nih.gov/pubmed/21917806

70. Kinnunen KM, Greenwood R, Powell JH, Leech R, Hawkins PC, Bonnelle V, Patel MC, Counsell SJ, Sharp DJ. White matter damage and cognitive impairment after traumatic brain injury. Brain [Internet]. 2011 Feb [cited 2013 Sep 27];134(Pt 2):449–63. Available from: http://www.pubmedcentral.nih.gov/articlerender.fcgi?artid=3030764&tool=pmcentrez&rendertype=abstract

71. Travers BG, Adluru N, Ennis C, Tromp DPM, Destiche D, Doran S, Bigler ED, Lange N, Lainhart JE, Alexander AL. Diffusion tensor imaging in autism spectrum disorder: a review. Autism Res [Internet]. 2012 Oct [cited 2013 Sep 26];5(5):289–313. Available from: http://www.ncbi.nlm.nih.gov/pubmed/22786754

72. Bendlin B, Ries M, Canu E, Sodhi A. White matter is altered with parental family history of Alzheimer's disease. Alzheimer's …. 2010;6(5):394-403.

73. Chou M-C, Lin Y-R, Huang T-Y, Wang C-Y, Chung H-W, Juan C-J, Chen C-Y. FLAIR diffusion-tensor MR tractography: comparison of fiber tracking with conventional imaging. AJNR Am J Neuroradiol. 2005 Mar;26(3):591-7.

74. Metzler-Baddeley C, O'Sullivan MJ, Bells S, Pasternak O, Jones DK. How and how not to correct for CSF-contamination in diffusion MRI. Neuroimage [Internet]. Elsevier Inc.; 2012 Jan 16 [cited 2013 Oct 19];59(2):1394-403. Available from: http://www.ncbi.nlm.nih.gov/pubmed/21924365

75. Rathi Y, Pasternak O, Savadjiev P, Michailovich O, Bouix S, Kubicki M, Westin C-F, Makris N, Shenton ME. Gray matter alterations in early aging: A diffusion magnetic resonance imaging study. Hum Brain Mapp [Internet]. 2013 Dec 31 [cited 2014 Jan 10];00. Available from: http://www.ncbi.nlm.nih.gov/pubmed/24382651

76. Hoy AR, Koay CG, Kecskemeti SR, Alexander AL. Optimization of a Free Water Elimination Two-Compartment Model for Diffusion Tensor Imaging. Neuroimage [Internet]. Elsevier B.V.; 2014 Sep [cited 2014 Sep 29];103:323-33. Available from: http://linkinghub.elsevier.com/retrieve/pii/S1053811914007952

77. Alexander DC, Barker GJ. Optimal imaging parameters for fiber-orientation estimation in diffusion MRI. Neuroimage [Internet]. 2005 Aug 15 [cited 2013 Sep 30];27(2):357-67. Available from: http://www.ncbi.nlm.nih.gov/pubmed/15921931

78. Jones DK, Basser PJ. "Squashing peanuts and smashing pumpkins": How noise distorts diffusion-weighted MR data. Magn Reson Med. 2004;52:979-93.

79. Jenkinson M, Beckmann CF, Behrens TEJ, Woolrich MW, Smith SM. Fsl. Neuroimage. 2012 Aug 15;62(2):782-90.

80. Zhang H, Yushkevich P a, Alexander DC, Gee JC. Deformable registration of diffusion tensor MR images with explicit orientation optimization. Med Image Anal. 2006 Oct;10(5):764–85.

81. Adluru N, Zhang H, Tromp DPM, Alexander AL. Effects of DTI spatial normalization on white matter tract reconstructions. SPIE Med … [Internet]. 2013 [cited 2014 Oct 9];(4):1–15. Available from: http://proceedings.spiedigitallibrary.org/proceeding.aspx?articleid=1667477

82. Wang R, Benner T. Diffusion toolkit: a software package for diffusion imaging data processing and tractography. Proc Intl Soc Mag Reson … [Internet]. 2007 [cited 2014 Jul 5];15:3720. Available from: http://cds.ismrm.org/ismrm-2007/files/03720.pdf

83. Okada T, Miki Y, Fushimi Y, Hanakawa T. Diffusion-Tensor Fiber Tractography: Intraindividual Comparison of 3.0-T and 1.5-T MR Imaging 1. Radiology. 2006;238(2):668–78.

84. Lebel C, Benner T, Beaulieu C. Six is enough? Comparison of diffusion parameters measured using six or more diffusion-encoding gradient directions with deterministic tractography. Magn Reson Med [Internet]. 2012 Aug [cited 2014 Jan 10];68(2):474–83. Available from: http://www.ncbi.nlm.nih.gov/pubmed/22162075

85. Hofer S, Frahm J. Topography of the human corpus callosum revisited--comprehensive fiber tractography using diffusion tensor magnetic resonance imaging. Neuroimage. 2006 Sep;32(3):989–94.

86. Okada T, Miki Y, Fushimi Y, Hanakawa T. Diffusion-Tensor Fiber Tractography: Intraindividual Comparison of 3.0-T and 1.5-T MR Imaging 1. Radiology. 2006;238(2):668–78.

87. Wakana S, Jiang H, Nagae-Poetscher L, van Zijl P, Mori S. Fiber Tract–based Atlas of Human White Matter Anatomy1. Radiology [Internet]. 2004 [cited 2013 Dec 19];230(1):77–87. Available from: http://radiology.rsna.org/content/230/1/77.short

88. Aboitiz F, Scheibel a B, Fisher RS, Zaidel E. Fiber composition of the human corpus callosum. Brain Res [Internet]. 1992 Dec 11;598(1-

2):143–53. Available from: http://www.ncbi.nlm.nih.gov/pubmed/1486478

89. Tomasch J. Size, distribution, and number of fibres in the human corpus callosum. Anat Rec [Internet]. 1954 [cited 2014 Jul 22];119:119–35. Available from: http://onlinelibrary.wiley.com/doi/10.1002/ar.1091190109/abstract

90. Pfefferbaum A, Sullivan E V., Hedehus M, Lim KO, Adalsteinsson E, Moseley M. Age-related decline in brain white matter anisotropy measured with spatially corrected echo-planar diffusion tensor imaging. Magn Reson Med. 2000;44:259–68.

91. Salat DH, Tuch DS, Greve DN, Van Der Kouwe AJW, Hevelone ND, Zaleta AK, Rosen BR, Fischl B, Corkin S, Diana Rosas H, Dale AM. Age-related alterations in white matter microstructure measured by diffusion tensor imaging. Neurobiol Aging. 2005;26:1215–27.

92. Abe O, Aoki S, Hayashi N, Yamada H, Kunimatsu A, Mori H, Yoshikawa T, Okubo T, Ohtomo K. Normal aging in the central nervous system: Quantitative MR diffusion-tensor analysis. Neurobiol Aging. 2002;23:433–41.

93. Engelter ST, Provenzale JM, Petrella JR, DeLong DM, MacFall JR. The effect of aging on the apparent diffusion coefficient of normal-appearing white matter. Am J Roentgenol [Internet]. 2000;175:425–30. Available from: http://www.ajronline.org/content/175/2/425.short₩nhttp://www.ncbi.nlm.nih.gov/pubmed/10915688

94. Masliah E, Mallory M, Hansen L, DeTeresa R, Terry RD. Quantitative synaptic alterations in the human neocortex during normal aging. Neurology. 1993;43:192–7.

95. Persson J, Nyberg L, Lind J, Larsson A, Nilsson LG, Ingvar M, Buckner RL. Structure-function correlates of cognitive decline in aging. Cereb Cortex. 2006;16:907–15.

96. Deary IJ, Bastin ME, Pattie A, Clayden JD, Whalley LJ, Starr JM, Wardlaw JM. White matter integrity and cognition in childhood and old age. Neurology. 2006;66:505–12.

97. Sullivan E V., Adalsteinsson E, Pfefferbaum A. Selective age-related degradation of anterior callosal fiber bundles quantified In vivo with fiber tracking. Cereb Cortex. 2006;16:1030–9.

98. Lebel C, Gee M, Camicioli R, Wieler M, Martin W, Beaulieu C. Diffusion tensor imaging of white matter tract evolution over the lifespan. Neuroimage. 2012;60:340–52.

99. Bendlin BB. White matter in aging and cognition: a cross-sectional study of microstructure in adults aged eightee to eighty-three. Dev Neuropsychol. 2010;6(5):394–403.

100. Ly M, Canu E, Xu G, Oh J, Mclaren DG, Dowling NM, Alexander AL, Sager MA, Johnson SC, Bendlin BB. Midlife measurements of white matter microstructure predict subsequent regional white matter atrophy in healthy adults. Hum Brain Mapp. 2014;35:2044–54.

101. Bendlin BB, Carlsson CM, Johnson SC, Zetterberg H, Blennow K, Willette A a, Okonkwo OC, Sodhi A, Ries ML, Birdsill AC, Alexander AL, Rowley H a, Puglielli L, Asthana S, Sager M a. CSF T-Tau/Aβ42 predicts white matter microstructure in healthy adults at risk for Alzheimer's disease. PLoS One [Internet]. 2012 Jan [cited 2014 Nov 6];7(6):e37720. Available from: http://www.pubmedcentral.nih.gov/articlerender.fcgi?artid=3368882&tool=pmcentrez&rendertype=abstract

102. Bozzali M, Falini A, Franceschi M, Cercignani M, Zuffi M, Scotti G, Comi G, Filippi M. White matter damage in Alzheimer's disease assessed in vivo using diffusion tensor magnetic resonance imaging. J Neurol Neurosurg Psychiatry. 2002;72:742–6.

103. Fellgiebel A, Schermuly I, Gerhard A, Keller I, Albrecht J, Weibrich C, Müller MJ, Stoeter P. Functional relevant loss of long association fibre tracts integrity in early Alzheimer's disease. Neuropsychologia. 2008;46:1698–706.

104. Hanyu H, Asano T, Sakurai H, Imon Y, Iwamoto T, Takasaki M, Shindo H, Abe K. Diffusion-weighted and magnetization transfer imaging of the corpus callosum in Alzheimer's disease. J Neurol Sci. 1999;167:37-44.

105. Huang J, Friedland RP, Auchus AP. Diffusion tensor imaging of normal-appearing white matter in mild cognitive impairment and early Alzheimer disease: Preliminary evidence of axonal degeneration in the temporal lobe. American Journal of Neuroradiology. 2007. p. 1943-8.

106. Rose SE, Janke AL, Chalk JB. Gray and white matter changes in Alzheimer's disease: a diffusion tensor imaging study. J Magn Reson Imaging. 2008;27:20-6.

107. Salat DH, Tuch DS, van der Kouwe AJW, Greve DN, Pappu V, Lee SY, Hevelone ND, Zaleta AK, Growdon JH, Corkin S, Fischl B, Rosas HD. White matter pathology isolates the hippocampal formation in Alzheimer's disease. Neurobiol Aging. 2010;31:244-56.

108. Stahl R, Dietrich O, Teipel SJ, Hampel H, Reiser MF, Schoenberg SO. White matter damage in Alzheimer disease and mild cognitive impairment: assessment with diffusion-tensor MR imaging and parallel imaging techniques. Radiology. 2007;243:483-92.

109. Takahashi S, Yonezawa H, Takahashi J, Kudo M, Inoue T, Tohgi H. Selective reduction of diffusion anisotropy in white matter of Alzheimer disease brains measured by 3.0 Tesla magnetic resonance imaging. Neurosci Lett [Internet]. 2002;332:45-8. Available from: http://www.sciencedirect.com/science?_ob=MImg&_imagekey=B6T0G-46XGS2H-F-H&_cdi=4862&_user=489256&_orig=search&_coverDate=10/25/2002&_sk=996679998&view=c&wchp=dGLbVzW-zSkWb&md5=dc23ebc3446eaacdb46b57d3bb5e8b44&ie=/sdarticle.pdf

110. Xie S, Xiao JX, Gong GL, Zang YF, Wang YH, Wu HK, Jiang XX. Voxel-based detection of white matter abnormalities in mild Alzheimer disease. Neurology. 2006;66:1845-9.

111. Duan J-H, Wang H-Q, Xu J, Lin X, Chen S-Q, Kang Z, Yao Z-B. White matter damage of patients with Alzheimer's disease correlated with the decreased cognitive function. Surg Radiol Anat. 2006;28:150–6.

112. Medina D, deToledo-Morrell L, Urresta F, Gabrieli JDE, Moseley M, Fleischman D, Bennett DA, Leurgans S, Turner DA, Stebbins GT. White matter changes in mild cognitive impairment and AD: A diffusion tensor imaging study. Neurobiol Aging. 2006;27:663–72.

113. Canu E, McLaren DG, Fitzgerald ME, Bendlin BB, Zoccatelli G, Alessandrini F, Pizzini FB, Ricciardi GK, Beltramello A, Johnson SC, Frisoni GB. Microstructural diffusion changes are independent of macrostructural volume loss in moderate to severe Alzheimer's disease. J Alzheimer's Dis. 2010;19:963–76.

114. Wang P-N, Chou K-H, Lirng J-F, Lin K-N, Chen W-T, Lin C-P. Multiple diffusivities define white matter degeneration in amnestic mild cognitive impairment and Alzheimer's disease. J Alzheimers Dis [Internet]. 2012;30:423–37. Available from: http://www.ncbi.nlm.nih.gov/pubmed/22430530

115. Huang H, Fan X, Weiner M, Martin-Cook K, Xiao G, Davis J, Devous M, Rosenberg R, Diaz-Arrastia R. Distinctive disruption patterns of white matter tracts in Alzheimer's disease with full diffusion tensor characterization. Neurobiol Aging. 2012;33:2029–45.

116. Perez-Nievas BG, Stein TD, Tai HC, Dols-Icardo O, Scotton TC, Barroeta-Espar I, Fernandez-Carballo L, De Munain EL, Perez J, Marquie M, Serrano-Pozo A, Frosch MP, Lowe V, Parisi JE, Petersen RC, Ikonomovic MD, López OL, Klunk W, Hyman BT, Gómez-Isla T. Dissecting phenotypic traits linked to human resilience to Alzheimer's pathology. Brain. 2013;136:2510–26.

117. Tosto G, Zimmerman ME, Carmichael OT, Brickman AM. Predicting aggressive decline in mild cognitive impairment: the importance of white matter hyperintensities. JAMA Neurol [Internet]. 2014;71:872–7. Available from: http://www.ncbi.nlm.nih.gov/pubmed/24821476

118. Brinkmalm G, Brinkmalm A, Bourgeois P, Persson R, Hansson O, Portelius E, Mercken M, Andreasson U, Parent S, Lipari F, Ohrfelt A,

Bjerke M, Minthon L, Zetterberg H, Blennow K, Nutu M. Soluble amyloid precursor protein α and β in CSF in Alzheimer’s disease. Brain Res [Internet]. 2013 Jun 4 [cited 2014 Nov 30];1513:117–26. Available from: http://www.ncbi.nlm.nih.gov/pubmed/23541617

119. McKhann G, Drachman D, Folstein M, Katzman R, Price D, Stadlan EM. Clinical diagnosis of Alzheimer’s disease: report of the NINCDS-ADRDA Work Group under the auspices of Department of Health and Human Services Task Force on Alzheimer's Disease. Neurology. 1984 Jul;34(7):939–44.

120. McKhann GM, Knopman DS, Chertkow H, Hyman BT, Jack CR, Kawas CH, Klunk WE, Koroshetz WJ, Manly JJ, Mayeux R, Mohs RC, Morris JC, Rossor MN, Scheltens P, Carrillo MC, Thies B, Weintraub S, Phelps CH. The diagnosis of dementia due to Alzheimer’s disease: Recommendations from the National Institute on Aging-Alzheimer’s Association workgroups on diagnostic guidelines for Alzheimer's disease. Alzheimer’s Dement. 2011 May;7(3):263–9.

121. Johnson SC, La Rue A, Hermann BP, Xu G, Koscik RL, Jonaitis EM, Bendlin BB, Hogan KJ, Roses AD, Saunders AM, Lutz MW, Asthana S, Green RC, Sager MA. The effect of TOMM40 poly-T length on gray matter volume and cognition in middle-aged persons with APOE ε3/ε3 genotype. Alzheimer’s Dement J Alzheimer's Assoc. 2011 Jul;7(4):456–65.

122. Sager MA, Hermann B, La Rue A. Middle-aged children of persons with Alzheimer’s disease: APOE genotypes and cognitive function in the Wisconsin Registry for Alzheimer's Prevention. J Geriatr Psychiatry Neurol. 2005;18:245–9.

123. Palmqvist S, Zetterberg H, Blennow K, Vestberg S, Andreasson U, Brooks DJ, Owenius R, Hägerström D, Wollmer P, Minthon L, Hansson O. Accuracy of brain amyloid detection in clinical practice using cerebrospinal fluid β-amyloid 42: a cross-validation study against amyloid positron emission tomography. JAMA Neurol. 2014 Oct;71(10):1282–9.

124. Wang Y, Gupta A, Liu Z, Zhang H, Escolar ML, Gilmore JH, Gouttard S, Fillard P, Maltbie E, Gerig G, Styner M. DTI registration in atlas

based fiber analysis of infantile Krabbe disease. Neuroimage. 2011;55:1577–86.

125. Zhang H, Yushkevich PA, Rueckert D, Gee JC. Unbiased white matter atlas construction using diffusion tensor images. Med Image Comput Comput Assist Interv. 2007;10:211–8.

126. Benjamini Y, Hochberg Y. Controlling the False Discovery Rate: A Practical and Powerful Approach to Multiple Testing. J R Stat Soc Ser B [Internet]. 1995;57:289 – 300. Available from: http://www.jstor.org/stable/2346101

127. Makris N, Goldstein JM, Kennedy D, Hodge SM, Caviness VS, Faraone S V., Tsuang MT, Seidman LJ. Decreased volume of left and total anterior insular lobule in schizophrenia. Schizophr Res. 2006;83:155–71.

128. Frazier J a, Chiu S, Breeze JL, Makris N, Lange N, Kennedy DN, Herbert MR, Bent EK, Koneru VK, Dieterich ME, Hodge SM, Rauch SL, Grant PE, Cohen BM, Seidman LJ, Caviness VS, Biederman J. Structural brain magnetic resonance imaging of limbic and thalamic volumes in pediatric bipolar disorder. Am J Psychiatry [Internet]. 2005 Jul;162(7):1256–65. Available from: http://www.ncbi.nlm.nih.gov/pubmed/15994707

129. Desikan RS, Ségonne F, Fischl B, Quinn BT, Dickerson BC, Blacker D, Buckner RL, Dale AM, Maguire RP, Hyman BT, Albert MS, Killiany RJ. An automated labeling system for subdividing the human cerebral cortex on MRI scans into gyral based regions of interest. Neuroimage [Internet]. 2006 Jul 1 [cited 2013 Dec 12];31(3):968–80. Available from: http://www.ncbi.nlm.nih.gov/pubmed/16530430

130. Goldstein JM, Seidman LJ, Makris N, Ahern T, O'Brien LM, Caviness VS, Kennedy DN, Faraone S V, Tsuang MT. Hypothalamic abnormalities in schizophrenia: sex effects and genetic vulnerability. Biol Psychiatry [Internet]. 2007 Apr 15 [cited 2013 Dec 16];61(8):935–45. Available from: http://www.ncbi.nlm.nih.gov/pubmed/17046727

131. Winkler AM, Ridgway GR, Webster M a, Smith SM, Nichols TE. Permutation inference for the general linear model. Neuroimage [Internet]. The Authors; 2014 May 15 [cited 2014 Jul 22];92:381–97. Available from: http://www.pubmedcentral.nih.gov/articlerender.fcgi?artid=4010955&tool=pmcentrez&rendertype=abstract

132. Smith SM, Nichols TE. Threshold-free cluster enhancement: Addressing problems of smoothing, threshold dependence and localisation in cluster inference. Neuroimage. 2009;44:83–98.

133. Larsson EM, Englund E, Sjöbeck M, Lätt J, Brockstedt S. MRI with diffusion tensor imaging post-mortem at 3.0 T in a patient with frontotemporal dementia. Dementia and Geriatric Cognitive Disorders. 2004. p. 316–9.

134. Alobuia WM, Xia W, Vohra BPS. Axon degeneration is key component of neuronal death in amyloid-β toxicity. Neurochem Int. 2013;63:782–9.

135. Christensen DZ, Huettenrauch M, Mitkovski M, Pradier L, Wirths O. Axonal degeneration in an alzheimer mouse model is PS1 gene dose dependent and linked to intraneuronal aβ accumulation. Front Aging Neurosci. 2014;6.

136. Krstic D, Knuesel I. Deciphering the mechanism underlying late-onset Alzheimer disease. Nat Rev Neurol [Internet]. 2013;9:25–34. Available from: http://www.ncbi.nlm.nih.gov/pubmed/23183882

137. Lansbury PT. Evolution of amyloid : What normal protein folding may tell us about fibrillogenesis and disease. Proc Natl Acad Sci U S A. 1999;96(March):3342–4.

138. Reiman EM, Quiroz YT, Fleisher AS, Chen K, Velez-Pardo C, Jimenez-Del-Rio M, Fagan AM, Shah AR, Alvarez S, Arbelaez A, Giraldo M, Acosta-Baena N, Sperling RA, Dickerson B, Stern CE, Tirado V, Munoz C, Reiman RA, Huentelman MJ, Alexander GE, Langbaum JBS, Kosik KS, Tariot PN, Lopera F. Brain imaging and fluid biomarker analysis in young adults at genetic risk for autosomal dominant

Alzheimer's disease in the presenilin 1 E280A kindred: A case-control study. Lancet Neurol. 2012;11:1048–56.

139. Xu G, McLaren DG, Ries ML, Fitzgerald ME, Bendlin BB, Rowley HA, Sager MA, Atwood C, Asthana S, Johnson SC. The influence of parental history of Alzheimer's disease and apolipoprotein E epsilon4 on the BOLD signal during recognition memory. Brain. 2009;132:383–91.

140. Johnson SC, Schmitz TW, Trivedi MA, Ries ML, Torgerson BM, Carlsson CM, Asthana S, Hermann BP, Sager MA. The influence of Alzheimer disease family history and apolipoprotein E epsilon4 on mesial temporal lobe activation. J Neurosci. 2006;26:6069–76.

141. Trivedi MA, Schmitz TW, Ries ML, Hess TM, Fitzgerald ME, Atwood CS, Rowley HA, Asthana S, Sager MA, Johnson SC. fMRI activation during episodic encoding and metacognitive appraisal across the lifespan: Risk factors for Alzheimer's disease. Neuropsychologia. 2008;46:1667–78.

142. Johnson SC, Ries ML, Hess TM, Carlsson CM, Gleason CE, Alexander AL, Rowley HA, Asthana S, Sager MA. Effect of Alzheimer disease risk on brain function during self-appraisal in healthy middle-aged adults. Arch Gen Psychiatry. 2007;64:1163–71.

143. Adluru N, Destiche DJ, Lu SY-F, Doran ST, Birdsill AC, Melah KE, Okonkwo OC, Alexander AL, Dowling NM, Johnson SC, Sager MA, Bendlin BB. White matter microstructure in late middle-age: Effects of apolipoprotein E4 and parental family history of Alzheimer's disease. NeuroImage Clin [Internet]. 2014;4:730–42. Available from: http://www.sciencedirect.com/science/article/pii/S2213158214000527

144. Jones DK, editor. Diffusion MRI: Theory, Methods, and Applications. Oxford University Press; 2011.